POINCARÉ SECTIONS AND RESONANT ORBITS IN THE RESTRICTED THREE-BODY PROBLEM

A Thesis

Submitted to the Faculty

of

Purdue University

by

Tatiana Mar Vaquero Escribano

In Partial Fulfillment of the

Requirements for the Degree

of

Master of Science in Aeronautics and Astronautics

May 2010

Purdue University

West Lafayette, Indiana

A papi y a mami.

To my husband, Matt.

ACKNOWLEDGMENTS

First and foremost, I would like to thank my parents, Miguel and Mercedes. Without your support, everything that I am and have done could not have been possible. *Mami, papi, este trabajo es tanto mío como vuestro. Sin vuestro cariño, paciencia, y apoyo no hubiera sido posible. Gracias por confiar en mí y por convencerme de que podía hacerlo. A papá, gracias por hacer que cada día salga el sol en esta ciudad eternamente nublada, y a mamá, gracias por todo el amor y los mejores consejos del mundo.*

To my husband, Matt: you have been my third pillar of support, and for that I am enormously grateful. Thank you for your endless love, patience, and support during all these years, and for giving up some of your goals so that I could pursue my own. I made it this far because of you.

Special thanks should also go to my advisor, Professor Kathleen C. Howell. Thank you for teaching me everything that I know in this field, and for being a role model. You have been my professor, advisor, and mentor. It is a privilege to have learned from you, both in and out of the classroom. I am proud to continue towards the next level of academics with you as my advisor.

I would also like to acknowledge very important people in my life who not only encouraged me through the process of this investigation, but made the journey enjoyable as well. Thank you to my brother, Miguel, and to my family-in-law: John, Teresa, Jamie, Matt W., and Patrick. Your support through the good and the bad has been a huge encouragement.

In addition, I would like to thank the Department of Foreign Languages and Literatures, and especially, Professor Maria L. Cooks, for their continuous support. You have provided the funding necessary to complete this investigation, and for this, I am very thankful. For similar reasons, I give thanks to the School of Aeronautics and

Astronautics. I also thank Professor DeLaurentis and Professor Longuski for serving on my committee.

I would like to express my gratitude to each member of our research group: Todd Brown, Diane Craig Davis, Daniel Grebow, Amanda Haapala, Aurelie Heritier, Jayme Howsman, Lucia Irrgang, Masaki Kakoi, Amanda Knutson, Zubin Olikara, Martin Ozimek, Chris Patterson, Tom Pavlak, Raoul Rausch, Wayne Schlei, Cody Short, Jeff Stuart, Rohan Sood, and Geoff Wawrzyniak. Thank you for answering all of my questions and for sharing your knowledge. You have been invaluable resources in the preparation of my final examination. I am proud to have learned from you and to be able to count such remarkable people among my friends. I look forward to sharing the next few years with you.

Y por último, gracias a la Cali por traer siempre la calma en medio de la tempestad.

TABLE OF CONTENTS

Page

Page

LIST OF TABLES

Table Page

LIST OF FIGURES

Figure Page

ABSTRACT

Vaquero Escribano, Tatiana Mar. M.S.A.A., Purdue University, May 2010. Poincaré Sections and Resonant Orbits in the Restricted Three-Body Problem. Major Professor: Kathleen C. Howell.

The application of dynamical systems techniques to mission design has demonstrated that the use of invariant manifolds and resonant flybys can enable previously unknown trajectory options and potentially reduce the ΔV requirements. In particular, recent investigations related to the Europa Orbiter baseline trajectory design demonstrate that the flyby segment of this trajectory appears to follow the invariant manifolds of 3:4 and 5:6 unstable resonant orbits before capture around Europa. This investigation includes a detailed analysis of planar and three-dimensional unstable resonant orbits as well as techniques for the computation and visualization of the associated invariant manifolds. Poincaré maps are used as an effective tool in the search for unstable resonant orbits and offer an insightful view of their invariant manifolds. These surface-of-sections are utilized to explore the relationship between the resonances and their invariant manifolds and to search for potential resonant transitions. For two specific energy levels and two different systems, a connection exists between the invariant manifolds associated with a number of two-dimensional unstable resonant orbits and this relationship yields transitions between resonances. In addition, a series of apparently resonant homoclinic-type connections in the Jupiter-Europa and Saturn-Titan systems are presented. The results obtained from this investigation may lead to interesting applications for trajectory and mission design.

1. INTRODUCTION

Previous analysis concerning dynamical systems techniques and resonance has demonstrated that the use of invariant manifolds and resonant flybys can enable previously unknown trajectory options and potentially reduce the ΔV requirements. Hence, this investigation focuses on the use of such techniques to explore the relationship between the invariant manifolds associated with unstable resonant orbits at a given energy level, and to determine their role in resonance transition.

1.1 Problem Definition

Much of the focus of this work involves the search, identification, and computation of planar and three-dimensional resonant orbits in the circular restricted three-body problem (CR3BP). Both the determination of the orbits and their use is facilitated by Poincaré sections. Poincaré sections are successfully employed as a tool to examine the relationship between the invariant manifolds of multiple unstable resonant orbits at a fixed value of Jacobi constant. The intersection of the invariant manifolds associated with these resonant trajectories, as viewed in the Poincaré map, is then employed to search for potential resonance transitions. The resulting transfer trajectories may benefit from a reduced maneuver cost (ΔV) by shadowing the invariant manifold trajectories. Thus, the core of this investigation is the application of Poincaré maps and resonance to the circular restricted three-body problem. As a result, the techniques can be applied in mission design.

1.2 Motivation

Interplanetary missions, such as the Jupiter Icy Moons Orbiter (JIMO) and the Jupiter Europa Orbiter (JEO), are designed to exploit multiple gravity assists as well as low-thrust propulsion. The complexity of such mission scenarios and the gravity environments suggest that dynamical systems techniques might offer important advantages. The JIMO spacecraft mission is designed to explore the icy moons of Jupiter, including Europa. Ganymede and Callisto are also flyby targets for the spacecraft. The JEO mission, a mission in NASA's Outer Planets Program, is planned to insert a spacecraft into orbit about Europa to determine the presence or absence of a liquid ocean on the moon [1]. Relevant to this investigation, the spacecraft encounters Europa in an 'endgame' phase. The first encounter is designed to insert the spacecraft into a 3:4 resonant orbit with respect to Europa, i.e., three spacecraft orbits to four Europa orbits, and the second encounter shifts the spacecraft to a 5:6 resonance orbit with Europa, leading to Europa Orbit Insertion (EOI) on the final pass [1].

This investigation is primarily motivated by the work of previous researchers [2] [3] [4] [5] involving the analysis of the invariant manifolds emanating from two specific unstable resonant orbits involved in the JEO encounters. In the previous work, it is apparent that the actual Europa Orbiter flyby trajectory appears to shadow the invariant manifolds of the 3:4 and 5:6 unstable resonant orbits just prior capture around Europa. Consequently, this effort is focused on understanding such relationships and using dynamical systems techniques to search for similar connections involving multiple resonances in different systems. One obvious extension is the application to the Saturn-Titan system.

1.3 Previous Contributions

A spacecraft that passes in close proximity to a moon in the Jovian or Saturnian system is modeled, in this analysis, within the context of the circular restricted three body problem (CR3BP). This dynamical model has been explored by many

investigators in the past, including some of the greatest researchers in the history of dynamics.

In 1687, Newton published his *PhilosophiæNaturalis Principia Mathematica*, also known as the *Principia*, and included an attempt to solve the n-body problem to explain the observed motion of the Moon around the Earth, and to predict the lunar position over time [6] [7]. In 1772, Euler first formulated a much simpler model where the motion of a small particle under the influence of two gravitational sources could be described, that is, the three-body problem [6]. He formulated the problem using a rotating coordinate system, in which the two gravitational bodies remain fixed and equilibrium point solutions exist. However, not until many years later did Poincaré give the problem the name 'circular restricted three-body problem' [7]. Both Euler and Lagrange discovered particular solutions in the three-body problem, those related to the equilibrium points. In 1772, Lagrange approximated periodic solutions to the problem, which Hill continued to examine in later years [5].

In 1843, Jacobi reduced the order in the three-body problem to six, and identified a single integral of motion, known as the Jacobian integral [7] [8]. Hill demonstrated the importance of this integral, in 1878, by defining regions of exclusion, or regions that are 'forbidden' to motion, where the massless body cannot be located for certain values of Jacobi constant [8]. Poincaré later continued Hill's research, and investigated periodic solutions. In his work, *Les Méthodes Nouvelles de la Mécanique Celeste* [9], Poincaré introduced a qualitative analysis of the CR3BP. He used this qualitative assessment to prove that, although the problem is non-integrable by the techniques that employ traditional integrals of motion [7], there are an infinite number of periodic solutions that exist in the CR3BP.

The origins of most of the dynamical systems techniques employed today appear in Poincaré's work [5]. In general terms, a dynamical systems approach attempts to describe the evolution of a future state as it follows from the current state; this description is either continuous via ordinary differential equations or discrete, using a map [5]. In 1892, Poincaré predicted the existence of particular structures, such as

periodic orbits and invariant manifolds [5]. Dynamical chaos, one of the key concepts introduced by Poincaré, can be defined as the highly sensitive dependence of dynamical systems on initial conditions [10] [11]. In other words, small differences in initial conditions yield widely diverging results for chaotic systems. As a result, long-term prediction is almost impossible [10], but it is the existence of chaos in the CR3BP that allows for transfers from an original position to different destinations at very little cost [5]. These concepts have been advanced by many researchers, including Birkhoff [12], as well as Kolmogorov, Arnold, and Moser.

In the 1960's, the application of the CR3BP moved into the space age when a mission to the Lagrange points was considered for NASA's Apollo program [13]. Since then, many of the structures that emerge in the CR3BP have been more widely used in trajectory design [14] [15] [16]. Consequently, successful missions to the vicinity of the Lagrange points have since been launched, such as the International Sun-Earth Explorer-3 (ISEE-3) [17], the Solar Heliospheric Observatory (SOHO) [18], the Advanced Composition Explorer (ACE) [19], and the Microwave Anisotropy Probe (MAP) [20]. Parallel to the development of these mission concepts, other researchers considered the possibility of applying dynamical systems techniques to these type of missions [5]. In fact, in the 1960's, Conley had investigated low energy transfer orbits to the Moon using dynamical system techniques [21]. However, the transfer orbits that Conley computed possessed a time of flight that was considered too great to be useful [5]. Nevertheless, he set the foundation for future work, and other researchers rapidly took over this design problem [22]. In the 1990's, the use of invariant manifolds as pathways between the Earth and the Sun-Earth libration points was finally applied to an actual mission [5]: the Genesis mission [23] [24] [25]. Since then, these techniques have been increasingly applied in mission design [26] [5].

The study of resonance, particularly within the context of flybys, has also advanced, and dynamical systems techniques are now applied to this problem [5]. The application of gravity flyby techniques to mission design also has a long history and was first introduced by Minovitch [27] [28] and others at the Jet Propulsion Labora-

tory (JPL) [5]. In almost all the multiple planetary flyby trajectories designed, some form of resonance is employed [5]. One reason for using resonant flybys is that the corresponding trajectories result in much lower maneuver costs. This efficient result is based in the exchange in momentum between the spacecraft and the planetary body during the flyby [5]. Another example of the use of resonance during planet or moon encounters is the Jupiter Europa Orbiter trajectory, which incorporates two different resonances with respect to Europa before capture around the Jovian moon [1].

One of the most significant examples of natural resonance in the solar system are comets in resonance with planetary orbits. The Jupiter family of comets, such as Gehrels 3, Oterma, and Helin-Roman-Crockett, are known to frequently transition between 3:2 and 2:3 resonances, sometimes including temporary captures by Jupiter for several revolutions [5]. As a result, many researchers have attempted to explain this phenomenon. In 1997, Belbruno and Marsden explained the transition between these resonances with a weak stability boundary concept [29] [5]. In 1998, Lo and Ross suggested that these comets were using the invariant manifolds associated with Sun-Jupiter libration point orbits to transition between resonances [25] [5]. In 2000, Koon, Lo, Marsden and Ross demonstrated, from a theoretical planar perspective, that the invariant manifolds of the 3:2 and 2:3 resonant orbits near Jupiter and the Lyapunov orbits in the vicinity of the Sun-Jupiter L_1 and L_2 libration points supply the mechanism for resonant transfer and capture around Europa [30] [31] [5]. Later, in 2001, Howell, Marchand, and Lo extended the analysis to three-dimensions and numerically confirmed the existence of this transition by comparing the orbits of several comets with arcs from the invariant manifolds of libration point orbits near the Sun-Jupiter L_1 and L_2 points [32] [5].

Based on the previous analyses concerning dynamical systems techniques and resonance, the focus of this investigation is the use such techniques to explore the relationship between the invariant manifolds of unstable resonant orbits at a given energy level, and to determine their role in resonance transition.

1.4 Thesis Overview

This investigation is organized as follows:

- Chapter 2: The n-body problem is described, and the necessary background regarding the formulation of the circular restricted three-body problem is developed. This chapter includes the derivation of the differential equations and the integrals of the motion, the state transition matrix, and a series of numerical techniques that are employed in the computation of periodic solutions in the CR3BP. Numerical examples of such periodic solutions are also included. Planar, periodic, Lyapunov orbits, and three-dimensional, periodic, halo orbits are discussed in detail. The required background in orbital stability is also developed.

- Chapter 3: The background regarding resonant orbits, invariant manifold theory, and Poincaré sections is developed in this chapter. The concept of resonance and the different types of resonance are first introduced. The mean motion orbital resonance, or orbit-orbit resonance, is the main focus of this investigation. Thus, this concept is primarily introduced from the perspective of the two-body problem and, subsequently, transitioned to the CR3BP. A numerical analysis of the planar and the three-dimensional resonant orbits is presented, followed by an introduction to invariant manifold theory. The invariant manifolds for fixed points as well as the invariant manifolds associated with periodic orbits are discussed. As an illustrative example, the numerical computation of the invariant manifolds that emanate from a libration point orbit is provided. The last section of this chapter illustrates the concept of Poincaré maps and the technique used in their computation. A series of Hénon maps are used to illustrate the concept of periodic, quasi-periodic, and chaotic trajectories obtained from the surfaces of section. Finally, this chapter also includes tables of physical constants, CR3BP constants, and values of the Jacobi constant at the libration points in the Jupiter-Europa and Saturn-Titan systems.

- Chapter 4: The concept of unstable resonant orbits is further discussed. A technique to compute such orbits from a Poincaré section is detailed. The process to compute the invariant manifolds of unstable resonant orbits and to display them in a Poincaré map is developed, along with numerical examples. Once the invariant manifolds associated with an unstable resonant orbit are displayed on a surface of section, the concept of resonance transition is discussed using a series of resonances in the Jupiter-Europa and Saturn-Titan systems. The two unstable resonant orbits involved in the planar Europa Orbiter flyby trajectory [5] are reproduced and the relationship between the associated invariant manifolds is demonstrated. This relationship is then expanded to multiple unstable resonant orbits at the same energy level. Two apparently homoclinic trajectories are presented, and further discussion ensues on the relationship between the invariant manifolds of the 3:4 resonance and other resonances at the given energy level. A similar analysis regarding a 2:3 unstable resonant orbits in the Saturn-Titan system is presented.

- Chapter 5: The final chapter includes a summary of the major results of this investigation, along with future recommendations to further investigate the problem and prepare a trajectory design tool.

2. BACKGROUND - DYNAMICAL MODELS AND NUMERICAL METHODS

Any study involving resonances typically defines a resonance initially within the context of the two-body problem and conics. This investigation, however, is focused on resonance conditions in a higher-fidelity environment, that is, involving multiple gravitational fields. Thus, the circular restricted three-body problem serves as the basis for the majority of this analysis. In the restricted problem, the motion of an infinitesimal third particle is modeled in the presence of two gravitationally-attracting bodies of significantly larger mass. Such a scenario can easily represent the behavior of a spacecraft in the presence of the Sun and a planet, or a planet and moon. As background that facilitates an understanding of the problem, the first section introduces the general n-body problem and then the framework, assumptions, and full formulation of the circular restricted three-body problem for this application.

2.1 The General n-Body Problem

Frequently, the ultimate goal in an investigation represented in terms of the n-body problem is a prediction of the motion of n celestial bodies given only their present position and velocity. The number of bodies with gravity is defined such that $n \geq 3$, that is, no less than three bodies, and thus, the label three-body problem. A diagram to define notation in the n-body problem appears in Fig. 2.1. The $\hat{X}, \hat{Y}, \hat{Z}$ system of coordinates denotes an inertial reference frame; point O identifies the origin, overbars indicate vectors, and carats represent unit vectors. The directional components of any vectors are identified with subscripts and the gravitational bodies in the system are labeled $P_1, P_2, ..., P_n$.

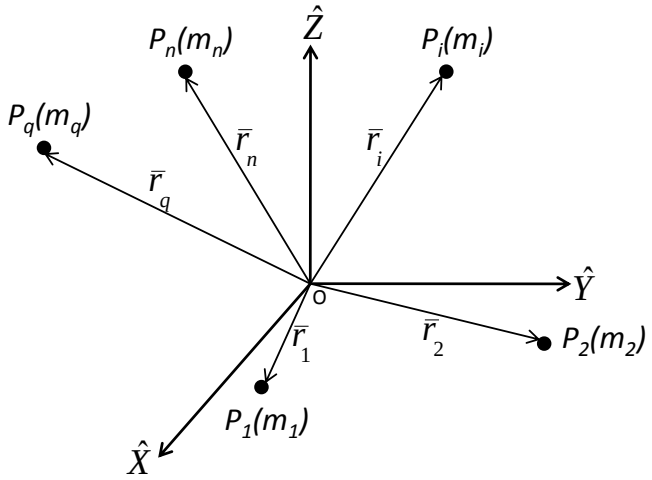

Fig. 2.1. Definitions in the n-body Problem

The mutual gravity between the n point masses is assumed to be the only force acting in the system. A force model is available from Newton's law of universal gravitation, that is,

$$\bar{F}_t = -Gm_i \sum_{\substack{j=1 \\ j\neq i}}^{n} \frac{m_j}{r_{ji}^3} \bar{r}_{ji} \tag{2.1}$$

where G is the universal gravitational constant. Using this force model, the equations of motion are derived from Newton's second law assuming that the masses in the system are constant and all derivatives are relative to an inertial observer. The resulting vector equation of motion for a particle P_i under the gravitational influence of n other particles is written,

$$m_i \frac{d^2\bar{r}_i}{dt^2} = -G \sum_{\substack{j=1 \\ j\neq i}}^{n} \frac{m_i m_j}{r_{ji}^3} \bar{r}_{ji} \tag{2.2}$$

In Eq. (2.2), however, the number of dependent variables, that is, the scalar components of position and velocity of m_i, $(\bar{r}_i, \dot{\bar{r}}_i)$, is greater than the number of equations. Ultimately, six scalar, first-order differential equations are required to model the degrees of freedom for each particle in the system, that is, a total of $6n$ differential equations for a system of n particles. These equations are non-linear and coupled.

From fundamental concepts in mechanics, only 10 integrals of motion are known to exist; even in just the two-body problem where $n = 2$, 12 equations are necessary for a closed-form analytical solution. An alternative relative formulation is more successful, i.e., expressing the position of particle $P_q(m_q)$ relative to particle $P_i(m_i)$, as defined in Fig. 2.2.

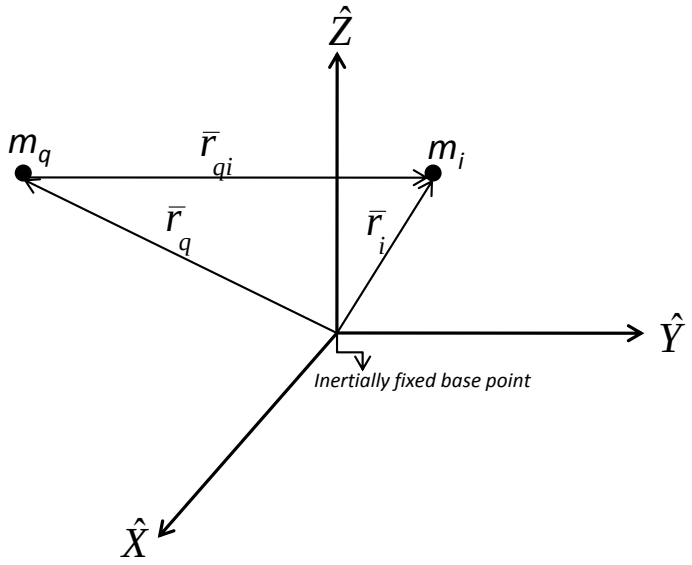

Fig. 2.2. Definition of the Relative Vector $\bar{r}_{qi}$, Representing the Location of Particle m_i Relative to Particle m_q

In the relative n-body problem, the equation for the motion of particle m_i relative to m_q is written,

$$\bar{r}''_{qi} + G\frac{(m_j + m_q)}{r^3_{qi}}\bar{r}_{qi} = G\sum_{\substack{j=1 \\ j\neq i,q}}^{n} m_j \left(\frac{\bar{r}_{ij}}{r^3_{ji}} - \frac{\bar{r}_{qj}}{r^3_{qj}}\right) \tag{2.3}$$

Note that primes identify derivatives with respect to dimensional time. The terms on the right represent the perturbation due to a third particle on the motion of both P_q and P_i. In the two-body problem, all perturbing terms are removed and a closed-form analytical solution is available. However, this analytical result no longer exists if even

one more body is added to the system. But, the dynamical system of equations in Eq. (2.3) can be solved numerically.

2.2 The Circular Restricted Three-Body Problem (CR3BP)

Limiting the number of particles reduces the complexity of the governing differential equations. For three gravitational sources, Eq. (2.3) reduces to the form,

$$m_3\bar{r}_3'' = -G\frac{m_3m_1}{r_{13}^3}\bar{r}_{13} - G\frac{m_3m_2}{r_{23}^3}\bar{r}_{23} \tag{2.4}$$

where m_3 is the infinitesimally small mass of the third particle P_3 and the masses m_1 and m_2 comprise the primary system. Solving Eq. (2.4) analytically requires the time history for the location of the primaries, that is, $\bar{r}_1(t)$ and $\bar{r}_2(t)$. Such information is not available since P_1 and P_2 are influenced by the motion of P_3 and its instantaneous position $\bar{r}_3(t)$. Recall that the simultaneous solution for all three position vectors requires 18 integrals, but only 10 are available. In the two-body problem, reformulating the problem in terms of relative motion is significant and yields an analytical solution, so the same strategy is employed for $n = 3$. Consider the motion of P_3 with respect to P_1,

$$\bar{r}_{13}'' + G\frac{(m_3+m_1)}{r_{13}^3}\bar{r}_{13} = Gm_2\left(\frac{\bar{r}_{32}}{r_{23}^3} - \frac{\bar{r}_{12}}{r_{12}^3}\right) \tag{2.5}$$

and the motion of P_3 with respect to P_2,

$$\bar{r}_{23}'' + G\frac{(m_3+m_2)}{r_{23}^3}\bar{r}_{23} = Gm_1\left(\frac{\bar{r}_{31}}{r_{13}^3} - \frac{\bar{r}_{21}}{r_{12}^3}\right) \tag{2.6}$$

This relative formulation results in two second-order vector differential equations for $\bar{r}_{13}$ and $\bar{r}_{23}$. A total of 12 constants are required and only 10 are available. Even though the relative-equation formulation reduces the number of equations that are necessary to completely model the system, an analytical solution is still not available. Further simplification is warranted to gain insight into the behavior of the system.

2.2.1 Assumptions

Three additional assumptions are critical to further decrease the complexity of the problem. All the assumptions are key in describing the motion of the primary system, i.e., P_1 and P_2. They are based on the relative mass ratios:

1. It is assumed that the mass of the third particle, P_3, is infinitesimally small relative to the masses of primary particles P_1 and P_2, that is, $m_3 \ll m_1, m_2$. This mass relationship is reasonable when m_3 represents a comet, spacecraft, or moon moving under the influence of the planets and/or the Sun. The assumption implies that m_3 does not influence the motion of m_1 and m_2.

2. If m_3 does not influence the motion of m_1 and m_2, then m_1 and m_2 represent an isolated two-body system. The solution in such a system is known to be a conic section. For many applications of interest, the solution is a closed conic. The masses m_1 and m_2 comprise the primary system; m_1 is arbitrarily selected as the larger primary. The center of mass is located at the barycenter on the line joining the primaries.

3. If the relative two-body primary motion is closed, it can be described as an ellipse. To further restrict motion, it is assumed that P_1 and P_2 move on circular orbits. This conic motion of the primaries is planar. However, the motion of P_3 is not constrained and the third particle is free to move in all three dimensions.

Given these assumptions, the problem can be reformulated as demonstrated in Fig. (2.3). From this relative formulation, the vector equation of motion for P_3 is written,

$$m_3\bar{r}_3'' = -G\frac{m_3m_1}{r_{13}^3}\bar{r}_{13} - G\frac{m_3m_2}{r_{23}^3}\bar{r}_{23} \tag{2.7}$$

The position vectors in Eq. (2.7) are defined in Fig. 2.3.

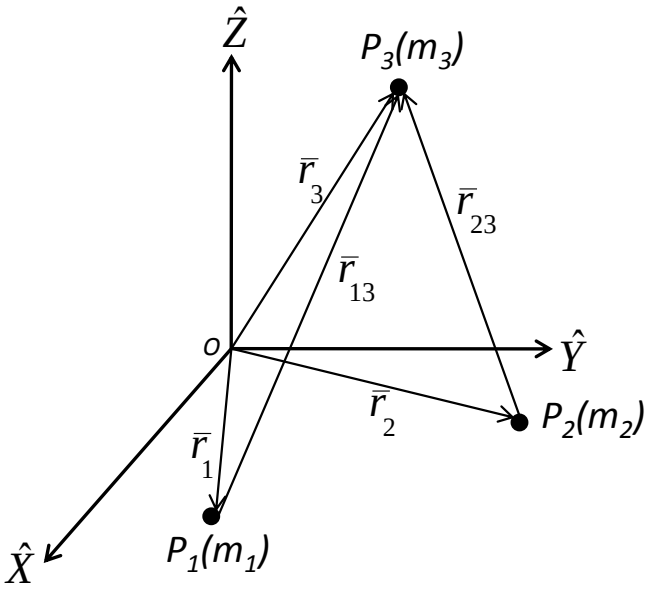

Fig. 2.3. Formulation of the Three-body Problem

2.2.2 Characteristic Quantities and Non-Dimensionalization

Further insight into this complex problem can be gained by non-dimensonalizing the parametric quantities in Eq. (2.7). Non-dimensionalization is most successfully accomplished if the characteristic quantities are selected to appropriately scale the problem. The following quantities are standard for studies in the CR3BP. The characteristic length, l^*, is defined as the distance between the primaries. The characteristic mass, m^*, represents the sum of the masses of the two primaries, and the orbital period of the system primaries in their relative motion is defined as the characteristic time, t^*. In summary,

$$l^* = \|\bar{r}_1\| + \|\bar{r}_2\| \tag{2.8}$$

$$m^* = m_1 + m_2 \tag{2.9}$$

$$t^* = \left[\frac{l^{*3}}{\widetilde{G}m^*}\right]^{\frac{1}{2}} \tag{2.10}$$

$$\tilde{G} = \frac{Gl^{*3}}{m^*t^{*2}} = 1 \tag{2.11}$$

where G is the universal gravitational constant. Several derived quantities are also very useful. The mean motion of the primary bodies in their conic orbit is non-dimensionalized to the value n, such that,

$$n = Nt^* = 1 \tag{2.12}$$

and time, the independent variable in the differential equations, is non-dimensionalized such that,

$$\tau = \frac{t}{t^*} \tag{2.13}$$

In addition to the characteristic quantities, the mass fraction μ is associated with the two system primaries P_1 and P_2 and is defined as,

$$\mu = \frac{m_2}{m_1 + m_2} = \frac{m_2}{m^*} \tag{2.14}$$

This mass ratio is often used to parameterize the ensuing motion.

2.2.3 Equations of Motion

The differential equations that govern the motion of P_3 are applicable to a wide variety of systems in a non-dimensional form. Equation (2.7) can be simplified with the aid of the characteristic quantities. In addition, a formulation relative to a rotating observer adds great insight and further applications. This rotating frame facilitates the identification of fixed equilibrium points corresponding to particular solutions in the CR3BP. These equilibrium points then serve as the starting point for the determination of periodic orbits.

To define the rotating frame, first recall the inertial frame that is defined in Fig. 2.2. The origin of the inertial frame is also fixed at B, the system barycenter. Then, the rotating frame is an additional reference frame, R, also centered at B such that the x-axis of the rotating frame is always parallel to the line connecting P_1 to P_2, and directed from the larger towards the smaller primary. Let $\hat{x}$ represent a unit vector in this direction. Since P_1 and P_2 move on conic paths, their mutual plane of

motion remains fixed. This fixed plane is defined as the common $\hat{X}\hat{Y}$- and $\hat{x}\hat{y}$-plane. Recall that the third particle P_3 can move in any of the three spatial dimensions. The z-axis of the rotating frame, i.e. $\hat{z}$, is parallel to the orbital angular momentum vector associated with the motion of the system; thus $\hat{z}$ and $\hat{Z}$ are parallel. Then, $\hat{y}$ completes the right-handed vector basis. The angle θ denotes the orientation of the rotating frame with respect to the inertial frame. The dimensional rate of change of θ, i.e. θ', is the angular velocity of the primary system, which is constant for circular orbits of the primaries and equal to the mean motion, N.

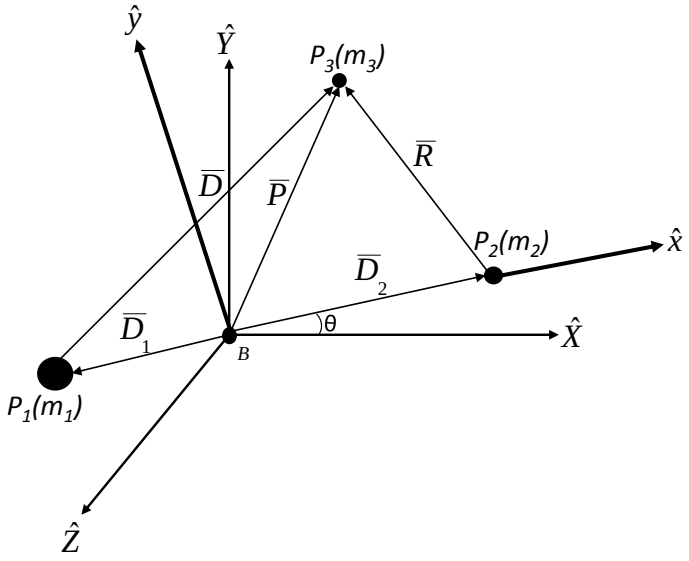

Fig. 2.4. Formulation of the CR3BP Relative to a Rotating Reference Frame

Once the rotating frame is clearly defined, the derivation of the equations of motion is straightforward. The positions of P_1, P_2, and P_3 with respect to the barycenter are defined by the vectors $\bar{D}_1$, $\bar{D}_2$, and $\bar{P}$, respectively. The position of P_3 relative to P_1 is $\bar{D}$ and that of P_3 relative to P_2 is $\bar{R}$. Let the position vector $\bar{P}$ be defined in terms of the scalar components,

$$\bar{P} = x_d\hat{x} + y_d\hat{y} + z_d\hat{z} \tag{2.15}$$

where x_d, y_d, z_d are dimensional quantities measured relative to the rotating frame. With these vector definitions, the non-dimensional distances $\bar{r}$, $\bar{d}$, and $\bar{\rho}$ are written,

$$\bar{r} = \frac{\bar{R}}{l^*} = (x - 1 + \mu)\,\hat{x} + y\hat{y} + z\hat{z} \tag{2.16}$$

$$\bar{d} = \frac{\bar{D}}{l^*} = (x + \mu)\,\hat{x} + y\hat{y} + z\hat{z} \tag{2.17}$$

$$\bar{\rho} = \frac{\bar{P}}{l^*} = x\hat{x} + y\hat{y} + z\hat{z} \tag{2.18}$$

where $l^* = \left\|\bar{D}_1\right\| + \left\|\bar{D}_2\right\|$ and x, y, z are non-dimensional quantities measured relative to the rotating frame. The specific quantities defined in Fig. 2.4 and Eqs. (2.15)-(2.18) are substituted into Eq. (2.7). The result is a vector, second-order differential equation for the motion of m_3 under the gravitational influence of larger masses m_1 and m_2,

$$\bar{\rho}'' = -(1 - \mu)\frac{\bar{d}}{d^3} - \mu\frac{\bar{r}}{r^3} \tag{2.19}$$

where the primes indicate derivatives with respect to the non-dimensional time, τ, relative to an inertial reference frame centered on the barycenter of the system. It is desirable to express Eq. (2.19) in terms of the Cartesian coordinates and the rotating reference frame. Expressions for $\bar{\rho}'$ and $\bar{\rho}''$ are derived from the Basic Kinematic Equation, BKE, that is,

$$\bar{\rho}' = \frac{{}^I d\bar{\rho}}{d\tau} = \frac{{}^R d\bar{\rho}}{d\tau} + {}^I\bar{\omega}^R \times \bar{\rho} \tag{2.20}$$

$$\bar{\rho}'' = \frac{{}^I d^2\bar{\rho}}{d\tau^2} = \frac{{}^R d^2\bar{\rho}}{d\tau^2} + 2{}^I\bar{\omega}^R \times \bar{\rho} + {}^I\bar{\omega}^R \times \left({}^I\bar{\omega}^R \times \bar{\rho}\right) \tag{2.21}$$

where ${}^I\bar{\omega}^R = n\hat{z}$ is the angular velocity of the rotating reference frame with respect to the inertial frame. The kinematic expressions for the velocity and acceleration relative to an observer in frame R are,

$$\dot{\bar{\rho}} = \frac{{}^R d\bar{\rho}}{d\tau} = \dot{x}\hat{x} + \dot{y}\hat{y} + \dot{z}\hat{z} \tag{2.22}$$

$$\ddot{\bar{\rho}} = \frac{{}^R d^2\bar{\rho}}{d\tau^2} = \ddot{x}\hat{x} + \ddot{y}\hat{y} + \ddot{z}\hat{z} \tag{2.23}$$

Recall that the dots indicate a derivative with respect to the non-dimensional time, τ, and relative to the rotating reference frame. Substituting Eq. (2.23) into Eq. (2.21) results in the following kinematic expansion,

$$\bar{\rho}'' = \left(\ddot{x} - 2n\dot{y} - n^2 x\right)\hat{x} + \left(\ddot{y} + 2n\dot{x} - n^2 y\right)\hat{y} + \ddot{z}\hat{z} \tag{2.24}$$

The kinematic expression for the acceleration in Eq. (2.24) is substituted into the left side of Eq. (2.19). The resulting vector equation of motion (EOM) reduces to the well known scalar, second-order differential equations in the CR3BP,

$$\ddot{x} - 2n\dot{y} - n^2 x = -\frac{(1-\mu)(x+\mu)}{d^3} - \frac{\mu}{r^3}(x - 1 + \mu) \tag{2.25}$$

$$\ddot{y} + 2n\dot{x} - n^2 y = -\frac{(1-\mu)}{d^3}y - \frac{\mu}{r^3}y \tag{2.26}$$

$$\ddot{z} = -\frac{(1-\mu)}{d^3}z - \frac{\mu}{r^3}z \tag{2.27}$$

where the magnitudes of $\bar{d}$ and $\bar{r}$ are evaluated as,

$$d = \sqrt{(x+\mu)^2 + y^2 + z^2} \tag{2.28}$$

$$r = \sqrt{(x-1+\mu)^2 + y^2 + z^2} \tag{2.29}$$

and the dot indicates a derivative with respect to the non-dimensional time, τ, and relative to an observer in the rotating reference frame. For future analysis, the non-linear system of differential equations in Eqs.(2.25)-(2.27) can be generally represented in first-order form as $\dot{\bar{X}} = \bar{F}(\bar{X}, \tau)$. The state vector $\bar{X}$ is the six-element state vector $\bar{X} = [x_1\ x_2\ x_3\ x_4\ x_5\ x_6]^T = [x\ y\ z\ \dot{x}\ \dot{y}\ \dot{z}]^T$, and the elements of $\bar{F}$ are expressed as,

$$\bar{X} = \begin{bmatrix} x_1 \\ x_2 \\ x_3 \\ x_4 \\ x_5 \\ x_6 \end{bmatrix}, \bar{F} = \begin{bmatrix} x_4 \\ x_5 \\ x_6 \\ 2nx_5 + n^2 x_1 - \frac{(1-\mu)(x_1+\mu)}{d^3} - \frac{\mu}{r^3}(x_1 - 1 + \mu) \\ -2nx_4 + n^2 x_2 - \frac{(1-\mu)}{d^3}x_2 - \frac{\mu}{r^3}x_2 \\ -\frac{(1-\mu)}{d^3}x_3 - \frac{\mu}{r^3}x_3 \end{bmatrix} \tag{2.30}$$

where d and r are similarly defined in terms of x_1, x_2, and x_3. These differential equations govern the motion of P_3 under the gravitational influence of the primary

bodies; the result is viewed by a rotating observer. All simulations in the CR3BP result from the numerical integration of these non-dimensional equations of motion.

2.2.4 Integrals of Motion

The differential equations of motion in Eqs. (2.25)-(2.27) can be further simplified by defining a pseudo-potential function. The scalar pseudo-potential U^* is defined as,

$$U^* = \frac{1-\mu}{d} + \frac{\mu}{r} + \frac{1}{2}n^2(x^2+y^2) \tag{2.31}$$

The differential equations of motion in Eqs. (2.25)-(2.27) can be rewritten in terms of the pseudo-potential and appear in the following form,

$$\ddot{x} - 2n\dot{y} = \frac{\partial U^*}{\partial x} \tag{2.32}$$

$$\ddot{y} + 2n\dot{x} = \frac{\partial U^*}{\partial y} \tag{2.33}$$

$$\ddot{z} = \frac{\partial U^*}{\partial z} \tag{2.34}$$

These equations and Eqs. (2.25)-(2.27) are equivalent.

The form of the equations in (2.32)-(2.34) does admit an integral of the motion. It is possible to produce the integral of the motion in the CR3BP by operating on Eqs. (2.32)-(2.34). Using a dot product between the differential equations and the rotating velocity vector, $\dot{\rho} = \dot{x}\hat{x} + \dot{y}\hat{y} + \dot{z}\hat{z}$, the resulting scalar equations are summed,

$$\dot{x}\ddot{x} + \dot{y}\ddot{y} + \dot{z}\ddot{z} = \frac{dU^*}{d\tau} \tag{2.35}$$

The scalar relationship in Eq. (2.35) can be directly integrated over non-dimensional time, τ, to produce the well known Jacobian integral, or Jacobi constant, C,

$$\frac{1}{2}\left(\dot{x}^2 + \dot{y}^2 + \dot{z}^2\right) = U^* - \frac{C}{2} \tag{2.36}$$

The constant of integration is defined as $-\frac{C}{2}$ for convenience so that the integral of motion can be more easily expressed in the form,

$$V^2 = 2U^* - C \tag{2.37}$$

where the speed relative to the rotating frame is denoted V. Thus, one integral of motion exists, but one constant of the motion is not sufficient for a closed-form solution. However, the lack of an analytical solution does not prevent a numerical analysis.

2.2.5 Equilibrium Solutions

For a coupled, non-linear set of differential equations, the behavior of the system is typically first investigated via equilibrium solutions. Equilibrium solutions are sought by examination of the system equations when the first and second derivatives are equal to zero. In Eqs. (2.32)-(2.34), if $\dot{\rho}$ and $\ddot{\rho}$ are zero, it is implied that the velocity and acceleration relative to the rotating frame are zero. Thus, if P_3 possesses no initial velocity or acceleration with respect to the rotating frame, P_3 theoretically maintains the given position indefinitely, relative to the rotating frame. Thus, from Eqs. (2.32)-(2.34) these equilibrium locations are determined by evaluating the gradient of the pseudo-potential function when the value is equal to zero,

$$\frac{\partial U^*}{\partial x} = \frac{\partial U^*}{\partial y} = \frac{\partial U^*}{\partial z} = 0 \tag{2.38}$$

where U^* is the pseudo-potential function from Eq. (2.31).

In 1772, Joseph-Louis Lagrange determined five equilibrium solutions, which were subsequently denoted the Lagrange points or libration points. The locations of these five equilibrium points, as viewed in the rotating frame, are indicated in Fig. 2.5. They are denoted by the symbol L_i, $i = 1, ..., 5$. By convention, the equilibrium point to the left of the smaller primary is labeled L_1; L_2 is located to the right of the smaller primary, and L_3 is the furthest point on the x-axis on the far side of the larger primary. The equilateral point with a positive y-component is labeled L_4; the final libration point with a negative y-component is L_5. All five equilibrium points are located in the plane of motion of the primaries, that is $z = 0$. Three of the five, the collinear points, lie along the x-axis, and the remaining two, the equilateral points, form equilateral

triangles with the primaries. The distances γ_1, γ_2, γ_3 locate the equilibrium points relative to the primaries. Effectively, at these equilibrium locations, the gravitational and centrifugal forces in the system cancel.

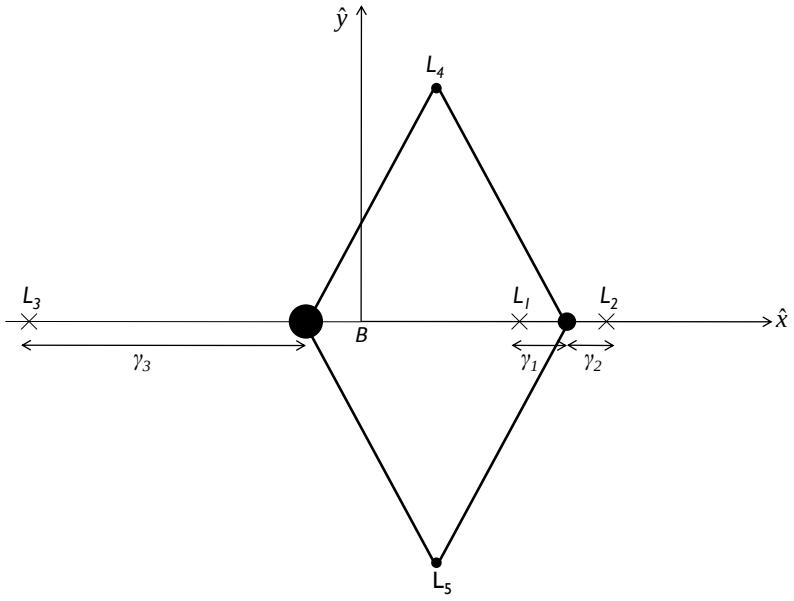

Fig. 2.5. Relative Location of the Lagrange Points, L_i, in the CR3BP

The location of the collinear points can be computed from Eq. (2.31) by expanding the partial expression $\frac{\partial U^*}{\partial x} = 0$ and solving for the three distinct x-axis crossings, which correspond to the locations of L_1, L_2, and L_3, that is,

$$x - \frac{1-\mu}{(x+\mu)^2} - \frac{\mu}{(x-1-\mu)^2} = 0 \tag{2.39}$$

where $x = (1 - \mu - \gamma_1)$ for L_1, $x = (1 - \mu + \gamma_2)$ for L_2 and $x = (-\mu - \gamma_3)$ for L_3. Recall that $y = 0$ and $z = 0$ for all three collinear points. The specific values for γ_1, γ_2, and γ_3 are determined from the following fifth-order polynomials,

$$\begin{aligned} \gamma_1^5 + \gamma_1^4(\mu - 3) + \gamma_1^3(3 - 2\mu) - \gamma_1^2(\mu) + \gamma_1(2\mu) - \mu = 0 \\ \gamma_2^5 + \gamma_2^4(3 - \mu) + \gamma_2^3(3 - 2\mu) - \gamma_2^2(-\mu) + \gamma_2(-2\mu) - \mu = 0 \\ \gamma_3^5 + \gamma_3^4(2 + \mu) + \gamma_3^3(1 + 2\mu) - \gamma_3^2(\mu - 1) + \gamma_3(2\mu - 2) - (1 - \mu) = 0 \end{aligned} \tag{2.40}$$

which are derived by substituting the (x,y,z) coordinates of L_1, L_2, and L_3 into Eq. (2.39).

The location of the equilateral points L_4 and L_5 can be computed with a similar approach, that is, $\frac{\partial U^*}{\partial x} = \frac{\partial U^*}{\partial y} = 0$. The terms in this expression can be algebraically manipulated to solve for d and r, leading to unit values in both cases. Hence, with $r = 1$ and $d = 1$ and the distance between the primaries normalized to one, that is, $d_1 + d_2 = 1$, it is straightforward to deduce that L_4 and L_5 are located at the vertices of two equilateral triangles with the primaries. The distance from the equilibrium point to one of the primaries is the same as the distance between the two primaries. Thus, the angle between the line connecting the point to the primary and the line connecting the two primaries is equal to 60 degrees. Given this geometry, it is apparent that the coordinates corresponding to the equilateral points are $x = \frac{1}{2} - \mu$, $y = \pm\frac{\sqrt{3}}{2}$ and $z = 0$. Thus, in vector form, the coordinates of the L_4 and L_5 Lagrange points are written as,

$$L_4 = \left[\frac{1}{2} - \mu, \frac{\sqrt{3}}{2}, 0\right] \tag{2.41}$$

$$L_5 = \left[\frac{1}{2} - \mu, -\frac{\sqrt{3}}{2}, 0\right] \tag{2.42}$$

Both are expressed relative to the barycenter and are clearly a function of the mass fraction, μ.

2.2.6 Zero Velocity Surfaces

The new equilibrium solutions and the Jacobi constant lead to two more important concepts: zero relative velocity and the zero velocity surfaces. Reconsider the Jacobian integral, Eq. (2.37). If the relative velocity V is zero and the full expression for the pseudo-potential U^* from Eq. (2.31) is inserted, then the relationship appears as follows,

$$x^2 + y^2 + \frac{2}{d}(1 - \mu) + \frac{2}{r}\mu = C \tag{2.43}$$

Recall that C is always positive since x^2 and y^2 are always positive and $\frac{2(1-\mu)}{d} > 0$, $\frac{2\mu}{r} > 0$ as well because d and r are distances and $0 < \mu < 1$. The values of the Jacobi constant at each libration point in the Earth-Moon system are summarized in Table 2.1 and labeled C_{L_1}, C_{L_2}, C_{L_3}, C_{L_4}, and C_{L_5}. The energy levels decrease such that $C_{L_5} = C_{L_4} < C_{L_3} < C_{L_2} < C_{L_1}$.

Table 2.1
Jacobi Constant Values for the Lagrange Points
in the Earth-Moon System

C_{L_1}	3.188340
C_{L_2}	3.172160
C_{L_3}	3.012147
C_{L_4}	2.987997
C_{L_5}	2.987997

For a given value of C, an infinite number of x, y, and z combinations satisfy Eq. (2.43). Together, the solutions define a surface in three-dimensional space. Hence, Eq. (2.43) represents the equation for a surface of zero velocity. For a given value of μ, the surface will change by varying the value of C. These zero velocity surfaces delineate two types of regions: a region where motion is physically possible and a "forbidden" region, or region of exclusion, where motion is physically impossible. The surfaces cannot be crossed, so at the given energy level, it is not possible to enter the "forbidden" region. Without a maneuver that alters the velocity state and, thus, the value of Jacobi constant, the zero velocity surfaces constrain the motion throughout any time evolution.

In Figs. 2.6-2.10, these zero velocity surfaces are represented and viewed from different perspectives. A full three-dimensional perspective appears in subplot (a) in the figures; a view down the z-axis onto the xy-plane appears in subplot (b). If the surfaces are projected onto the xy-plane, the projections are curves and are denoted as zero velocity curves (ZVC). In these figures, the surfaces are colored in gray; the

black crosses represent the five equilibrium points L_1, L_2, L_3, L_4, and L_5, and the Earth and the Moon appear as black spheres, although the bodies may not be visible in all the figures.

For large values of the Jacobi constant, the solution to Eq. (2.43) yields three distinct surfaces that are apparent in Figs. 2.6-2.10. One of the zero velocity surfaces is a relatively large cylinder with its axis of symmetry parallel to the z-axis. Closer to the primaries, for smaller values of d and r, two surfaces that appear as small ovoids form about the primaries. If these surfaces are projected onto the xy-plane, three distinct curves can be identified in the plane. As the value of the Jacobi constant decreases, the *3*-D surfaces and *2*-D curves change accordingly. The outer circle shrinks in radius, the smaller ovals increase in size, and eventually the two inner curves meet at L_1, as is apparent in Fig. 2.6(b). Clearly, changing the energy level modifies the surface characteristics. By continuing to reduce the value of C, the interior region expands and a corridor opens between the larger and the smaller primary (Fig. 2.7). Trajectories that extend between the larger and smaller primaries can now exist without a maneuver to maintain the energy level. As the Jacobi constant value is decreased from C_{L_2} to a value C such that $C_{L_3} < C < C_{L_2}$, the gateway at L_2 opens. This opening gateway links the interior region near the primaries and the exterior region beyond the outer-most surface. As this interior region enlarges, the next point of intersection with the outer regions occurs at L_3, allowing free motion between the primaries and the three collinear points, as is apparent in Fig. 2.8. As the value of the Jacobi constant decreases further, two separate curves enclosing the equilibrium points L_4 and L_5 appear. These regions will shrink until $C = C_{L_4} = C_{L_5}$, where the projection of the surfaces onto the plane appears simply as two points at the location of the equilateral points. These points will disappear as the surface leaves the plane when the value of C is less than $C_{L_4} = C_{L_5}$. The associated evolving surfaces appear in Figs. 2.9-2.10. At values of C lower than those associated with L_4 and L_5, there are still large regions of three-dimensional space that are not accessible.

However, motion in the xy-plane is no longer bounded. These out-of-plane surfaces are symmetric across the plane of the primary motion.

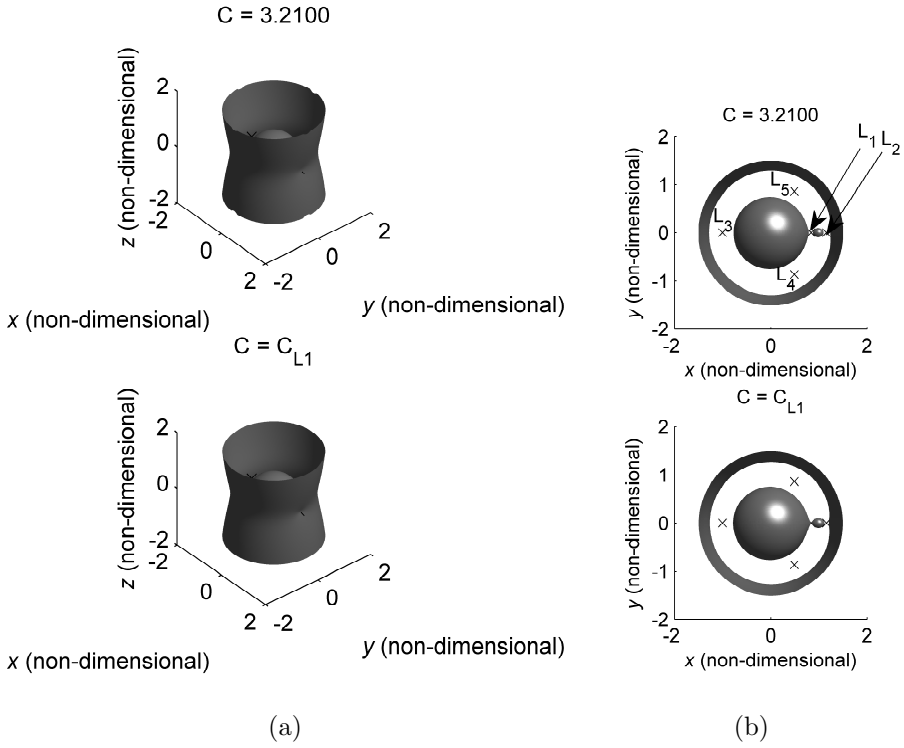

(a) (b)

Fig. 2.6. Zero Velocity Surfaces for Values of $C = 3.2100$ and $C = C_{L_1}$ in the Earth-Moon System

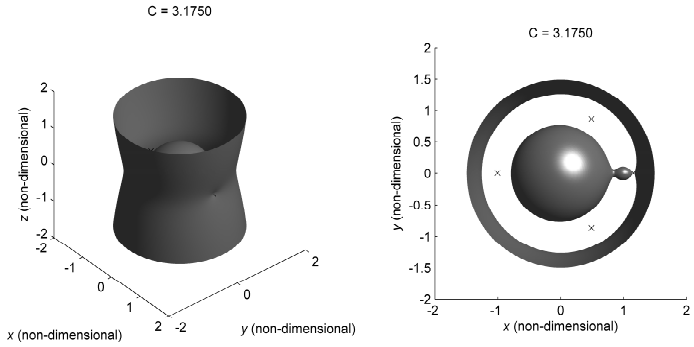

Fig. 2.7. Zero Velocity Surfaces for a Value of $C < C_{L_1}$ in the Earth-Moon System

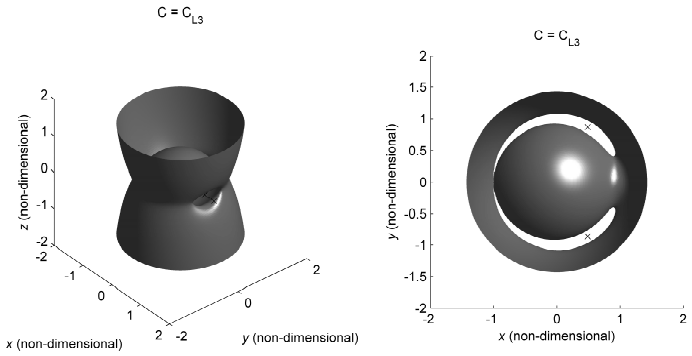

Fig. 2.8. Zero Velocity Surfaces for $C = C_{L_3}$ in the Earth-Moon System

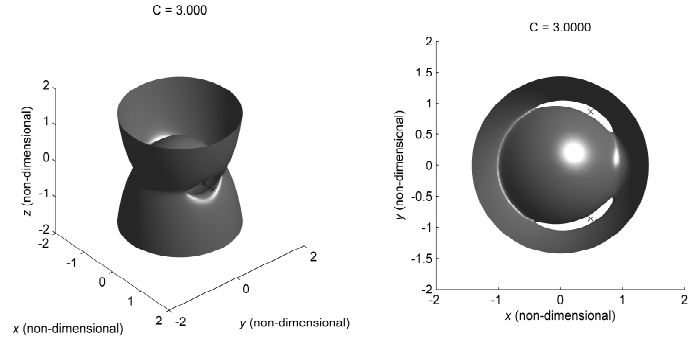

Fig. 2.9. Zero Velocity Surfaces for $C < C_{L_3}$ in the Earth-Moon System

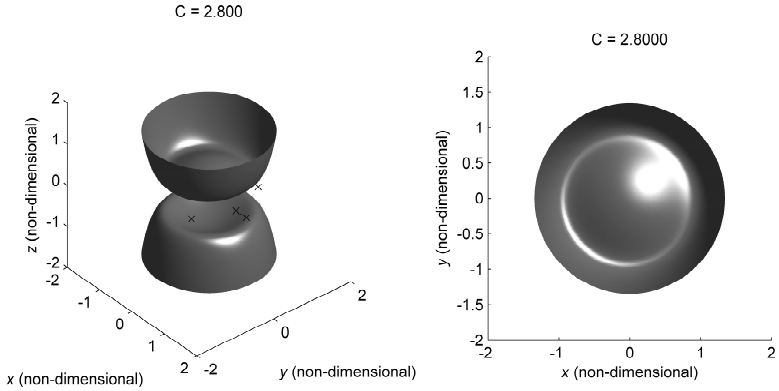

Fig. 2.10. Zero Velocity Surfaces for $C = 2.8000$ in the Earth-Moon System

2.2.7 Coordinate Transformations: Rotating Frame to/from Inertial Frame

Although visualizing trajectories in the rotating frame offers very useful information, it is also desirable to view these trajectories from the perspective of the inertial reference frame. Transformation between inertial and rotating coordinates is facilitated with the appropriate direction cosine matrix [13]. In Fig. 2.11, the angle θ is defined as the orientation angle of the rotating frame R ($\hat{x}-\hat{y}-\hat{z}$) with respect to the inertial frame I ($\hat{X}-\hat{Y}-\hat{Z}$). Recall that the orientation angle changes at a constant rate in the circular restricted three-body model, that is, $\dot{\theta}$=constant. The position vector $\bar{\rho}$ with respect to the barycenter can be expressed in terms of either the rotational or inertial unit vectors and these coordinates are related by the direction cosine matrix, ${}^{I}C^{R}$, that is,

$$\begin{bmatrix} \hat{X} \\ \hat{Y} \\ \hat{Z} \end{bmatrix} = {}^{I}C^{R}(\tau) \begin{bmatrix} \hat{x} \\ \hat{y} \\ \hat{z} \end{bmatrix} \tag{2.44}$$

This direction cosine matrix reflects a simple rotation about the z-axis, which is common to both frames. Since the angle θ varies at a constant rate, the matrix ${}^{I}C^{R}$ is an explicit function of the non-dimensional time, τ. Hence, $\theta = nt^{*} = n(\tau - \tau_0)$, where τ_0 is the initial time. By definition, the non-dimensional mean motion, n, is equal to one. Thus, the direction cosine matrix can be expressed directly in terms of the non-dimensional time as,

$${}^{I}C^{R}(\tau) = \begin{bmatrix} cos(\tau-\tau_0) & -sin(\tau-\tau_0) & 0 \\ sin(\tau-\tau_0) & cos(\tau-\tau_0) & 0 \\ 0 & 0 & 1 \end{bmatrix} \tag{2.45}$$

Note that the direction cosine matrix in Eq. (2.45) can be inverted to obtain the inverse transformation, i.e., from rotational to inertial coordinates.

The availability of the position and the velocity vectors in terms of rotational and inertial coordinates is very useful. However, such a transformation also involves the use of the Basic Kinematic Equation from Eq. (2.20). The non-dimensional

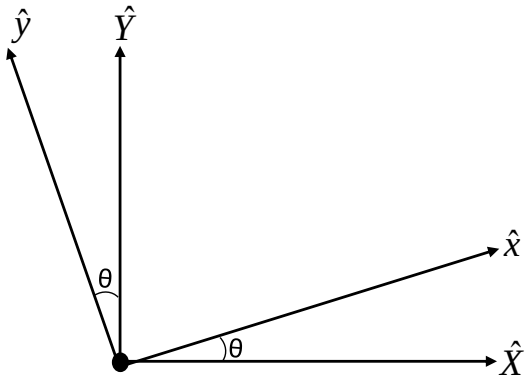

Fig. 2.11. Orientation of the Rotating Frame Relative to the Inertial Frame

position and velocity vectors expressed in terms of inertial and rotating coordinates are respectively,

$$\bar{\rho}_{in} = X\hat{X} + Y\hat{Y} + Z\hat{Z} \tag{2.46}$$

$$\bar{\rho}'_{in} = X'\hat{X} + Y'\hat{Y} + Z'\hat{Z} \tag{2.47}$$

$$\bar{\rho}_{rot} = x\hat{x} + y\hat{y} + z\hat{z} \tag{2.48}$$

$$\bar{\rho}'_{rot} = (\dot{x} - ny)\,\hat{x} + (\dot{y} + nx)\,\hat{y} + \dot{z}\hat{z} \tag{2.49}$$

leading to the position and velocity transformation. Recall the six-element state vector $\bar{X}$ defined in Eq. (2.30). Then, the transformation from rotating to inertial coordinates appears as a 6x6 block matrix, that is,

$$\begin{bmatrix} X \\ Y \\ Z \\ X' \\ Y' \\ Z' \end{bmatrix} = \begin{bmatrix} {}^{I}C^{R}(\tau) & 0_{3x3} \\ \dot{C}(\tau) & {}^{I}C^{R}(\tau) \end{bmatrix} \begin{bmatrix} x \\ y \\ z \\ \dot{x} \\ \dot{y} \\ \dot{z} \end{bmatrix} \tag{2.50}$$

where the submatrix 0_{3x3} is the 3x3 zero matrix, the submatrix ${}^{I}C^{R}(\tau)$ is represented in Eq. (2.45), and the submatrix $\dot{C}(\tau)$ is defined as,

$$\dot{C}(\tau) = \begin{bmatrix} -sin(\tau - \tau_0) & -cos(\tau - \tau_0) & 0 \\ cos(\tau - \tau_0) & -sin(\tau - \tau_0) & 0 \\ 0 & 0 & 0 \end{bmatrix} \tag{2.51}$$

The inverse of this block matrix leads to the inverse transformation.

2.3 The State Transition Matrix

In the circular restricted three-body problem, it is of great interest to explore different types of solutions to the non-linear differential equations as well as the dynamical behavior in the vicinity of these solutions. Periodic orbits in the vicinity of the libration points is one type of solution that is a particular focus in this analysis. To compute periodic orbits, the equations are typically linearized and a non-constant sensitivity matrix $\Phi(\tau, \tau_0)$ is required to determine the periodic orbits of interest. This matrix $\Phi(\tau, \tau_0)$, denoted the State Transition Matrix (STM), is associated with the variational equations relative to a reference solution that satisfies the non-linear differential equations in the CR3BP.

The first-order form of the non-linear system of differential equations is generally represented as $\dot{\bar{X}} = \bar{F}(\bar{X}, \tau)$, where the six-element vector state $\bar{X}$ is defined in Eq. (2.30). It is assumed that a particular reference solution, $\bar{X}_n(\tau)$, to the non-linear differential equations is available. Some desired solution nearby this reference, i.e., $\bar{X}(\tau) = \bar{X}_n(\tau) + \delta\bar{X}(\tau)$, can be represented in terms of a Taylor series expansion relative to the reference solution. By retaining only the linear terms, the first-order variations relative to the reference are defined. This expansion results in a linear equation expressed in terms of the variations in the state, $\delta\bar{X}(\tau)$, of the form,

$$\delta\dot{\bar{X}}(\tau) = A(\tau)\delta\bar{X} + \bar{P}(\tau) \tag{2.52}$$

In this problem, time does not appear explicitly, hence, $\bar{P}(t) = \frac{\partial \bar{X}}{\partial t}\delta\tau = 0$, leading to the linear vector variational equations,

$$\delta\dot{\bar{X}} = A(\tau)\delta\bar{X} \tag{2.53}$$

where $A(\tau)$ is the Jacobian matrix and $\delta\bar{X}(\tau) = [\delta x\ \delta y\ \delta z\ \delta\dot{x}\ \delta\dot{y}\ \delta\dot{z}]^T$. Thus, Eq. (2.53) can be expanded in matrix form as,

$$\begin{bmatrix} \delta\dot{x} \\ \delta\dot{y} \\ \delta\dot{z} \\ \delta\ddot{x} \\ \delta\ddot{y} \\ \delta\ddot{z} \end{bmatrix} = \begin{bmatrix} 0 & 0 & 0 & 1 & 0 & 0 \\ 0 & 0 & 0 & 0 & 1 & 0 \\ 0 & 0 & 0 & 0 & 0 & 1 \\ U^*_{xx} & U^*_{xy} & U^*_{xz} & 0 & 2 & 0 \\ U^*_{yx} & U^*_{yy} & U^*_{yz} & -2 & 0 & 0 \\ U^*_{zx} & U^*_{zy} & U^*_{zz} & 0 & 0 & 0 \end{bmatrix} \begin{bmatrix} \delta x \\ \delta y \\ \delta z \\ \delta\dot{x} \\ \delta\dot{y} \\ \delta\dot{z} \end{bmatrix} \tag{2.54}$$

The lower left block of the Jacobian matrix involves the second partial derivatives of the pseudo-potential function, U^*, from Eq. (2.31). The partials are evaluated individually as,

$$U^*_{xx} = \frac{\partial^2 U^*}{\partial x^2} = 1 - \frac{(1-\mu)}{d^3} + \frac{3(1-\mu)(x+\mu)^2}{d^5} - \frac{\mu}{r^3} + \frac{3\mu(x-1+\mu)^2}{r^5} \tag{2.55}$$

$$U^*_{yy} = \frac{\partial^2 U^*}{\partial y^2} = 1 - \frac{(1-\mu)}{d^3} + \frac{3(1-\mu)y^2}{d^5} - \frac{\mu}{r^3} + \frac{3\mu y^2}{r^5} \tag{2.56}$$

$$U^*_{zz} = \frac{\partial^2 U^*}{\partial z^2} = -\frac{(1-\mu)}{d^3} + \frac{3(1-\mu)z^2}{d^5} - \frac{\mu}{r^3} + \frac{3\mu z^2}{r^5} \tag{2.57}$$

$$U^*_{xy} = \frac{\partial^2 U^*}{\partial x \partial y} = U^*_{yx} = \frac{3(1-\mu)(x+\mu)y}{d^5} + \frac{3\mu(x-1+\mu)y}{r^5} \tag{2.58}$$

$$U^*_{xz} = \frac{\partial^2 U^*}{\partial x \partial z} = U^*_{zx} = \frac{3(1-\mu)(x+\mu)z}{d^5} + \frac{3\mu(x-1+\mu)z}{r^5} \tag{2.59}$$

$$U^*_{yz} = \frac{\partial^2 U^*}{\partial y \partial z} = U^*_{zy} = \frac{3(1-\mu)zy}{d^5} + \frac{3\mu zy}{r^5} \tag{2.60}$$

where d and r are defined in Eqs. (2.28)-(2.29). So, the general solution to Eq. (2.53) is of the form,

$$\delta\bar{X}(\tau) = \Phi(\tau, \tau_0)\delta\bar{X}_0 \tag{2.61}$$

where $\Phi(\tau, \tau_0)$ is the STM and $\delta\bar{X}_0$ is the six-element initial deviation from a given initial state $\bar{X}_0$ that is associated with the reference. Neither the matrix $A(\tau)$ nor

$\Phi(\tau, \tau_0)$ is constant in general. The evolution of the matrix $\Phi(\tau, \tau_0)$ is governed by the matrix differential equation,

$$\dot{\Phi}(\tau, \tau_0) = A(\tau)\Phi(\tau, \tau_0) \tag{2.62}$$

which represents 36 scalar differential equations since $\Phi(\tau, \tau_0)$ is a 6x6 matrix. Including the integration of the six scalar differential equations for the state vector $\bar{X}$ in Eq. (2.30), simulation in the CR3BP involves the numerical integration of a total of 42 differential equations. At the initial time, the matrix $\Phi(\tau, \tau_0)$ is equal to the 6x6 identity matrix.

The elements of the STM contain valuable information about the sensitivities of the final state to variations in the initial state. That is, the partial derivatives in the STM reflect the change in a final state due to a change in the corresponding initial state, that is,

$$\begin{bmatrix} \delta x_f \\ \delta y_f \\ \delta z_f \\ \delta \dot{x}_f \\ \delta \dot{y}_f \\ \delta \dot{z}_f \end{bmatrix} = \begin{bmatrix} \frac{\partial x}{\partial x_0} & \frac{\partial x}{\partial y_0} & \frac{\partial x}{\partial z_0} & \frac{\partial x}{\partial \dot{x}_0} & \frac{\partial x}{\partial \dot{y}_0} & \frac{\partial x}{\partial \dot{z}_0} \\ \frac{\partial y}{\partial x_0} & \frac{\partial y}{\partial y_0} & \frac{\partial y}{\partial z_0} & \frac{\partial y}{\partial \dot{x}_0} & \frac{\partial y}{\partial \dot{y}_0} & \frac{\partial y}{\partial \dot{z}_0} \\ \frac{\partial z}{\partial x_0} & \frac{\partial z}{\partial y_0} & \frac{\partial z}{\partial z_0} & \frac{\partial z}{\partial \dot{x}_0} & \frac{\partial z}{\partial \dot{y}_0} & \frac{\partial z}{\partial \dot{z}_0} \\ \frac{\partial \dot{x}}{\partial x_0} & \frac{\partial \dot{x}}{\partial y_0} & \frac{\partial \dot{x}}{\partial z_0} & \frac{\partial \dot{x}}{\partial \dot{x}_0} & \frac{\partial \dot{x}}{\partial \dot{y}_0} & \frac{\partial \dot{x}}{\partial \dot{z}_0} \\ \frac{\partial \dot{y}}{\partial x_0} & \frac{\partial \dot{y}}{\partial y_0} & \frac{\partial \dot{y}}{\partial z_0} & \frac{\partial \dot{y}}{\partial \dot{x}_0} & \frac{\partial \dot{y}}{\partial \dot{y}_0} & \frac{\partial \dot{y}}{\partial \dot{z}_0} \\ \frac{\partial \dot{z}}{\partial x_0} & \frac{\partial \dot{z}}{\partial y_0} & \frac{\partial \dot{z}}{\partial z_0} & \frac{\partial \dot{x}}{\partial \dot{x}_0} & \frac{\partial \dot{z}}{\partial \dot{y}_0} & \frac{\partial \dot{z}}{\partial \dot{z}_0} \end{bmatrix} \begin{bmatrix} \delta x_0 \\ \delta y_0 \\ \delta z_0 \\ \delta \dot{x}_0 \\ \delta \dot{y}_0 \\ \delta \dot{z}_0 \end{bmatrix} \tag{2.63}$$

Recall that time, τ, does not explicitly appear in the EOM, and hence, $\delta\tau_f = 0$. This matrix is an effective linear predictor of the sensitivity of the final state to variations in the initial state, or in the state at an earlier time. The use of the STM is fundamental in computing periodic orbits and assessing their stability.

2.3.1 Stability of the Constant Equilibrium Solutions, L_i

The stability of the five equilibrium points can now be investigated by using the variational equations and the STM. The non-linear system of differential equations in Eqs.(2.32)-(2.34) can be linearized relative to the equilibrium solutions yielding a set

of linear variational equations that can be employed to assess the stability, and, thus, gain insight into the nature of the motion in the vicinity of the libration points [8]. Stability can be discussed from many different perspectives. In a general sense, stability is always defined in terms of a reference solution. If a disturbance from the reference yields behavior that remains in the small neighborhood of an equilibrium point, then the reference solution is considered stable. However, there are other types of stability, such as Poisson stability, as well as Laplace or Hill stability. The stability criteria employed in this investigation to assess the equilibrium points is Lyapunov stability, and it only holds if the reference solution is constant. For computation, Lyapunov stability is based on the characteristics of the eigenvalues determined from the characteristic equation associated with matrix A, which is constant for the equilibrium points. (In the case of periodic orbits, where the Jacobian matrix is not constant but periodic, the following Lyapunov analysis is not valid and further stability concepts are introduced.) The specific developments and definitions used in this section closely follow the discussion in *Theory of Orbits: The Restricted Problem of Three Bodies*, by Szebehely [8].

- *Complex eigenvalues.* If all the eigenvalues possess negative real parts, then the equilibrium point is asymptotically stable. If some of the eigenvalues possess positive real parts, then the equilibrium point is unstable. This criteria is valid for multiple roots.

- *Pure imaginary eigenvalues.* If all the eigenvalues are imaginary, generally, the motion is oscillatory and the solution is defined as stable, but not asymptotically stable. However, if there are multiple roots, the solution contains mixed (periodic and secular) terms, and thus, is unstable.

- *Real eigenvalues.* If any of the eigenvalues are positive real integers, the reference solution is unstable. If the roots are all negative real integers, the solution is stable. This criteria holds for multiple roots.

Hence, the stability of the libration points is linked to the constant matrix A and its associated eigenvalues. This matrix is derived from the variational equations and appear in general form in Eq. (2.53). For the specific application to the libration points, the process is initiated with the five equilibrium solutions represented as $L(a, b, c)$, where a, b, and c locate L_i with the values in Table 2.1 and Eqs. (2.41)-(2.42) for L_4 and L_5. Then, the perturbed state relative to $L(a, b, c)$ is expressed as,

$$x = a + \xi \tag{2.64}$$

$$y = b + \eta \tag{2.65}$$

$$z = c + \rho \tag{2.66}$$

where ξ, η, and ρ are the variations relative to L_i. Since the L_i locations are constant in the CR3BP, the first and second time derivatives of x, y, and z can be expressed in terms of ξ, η, and ρ as,

$$\dot{x} = \dot{\xi} \tag{2.67}$$

$$\dot{y} = \dot{\eta} \tag{2.68}$$

$$\dot{z} = \dot{\rho} \tag{2.69}$$

$$\ddot{x} = \ddot{\xi} \tag{2.70}$$

$$\ddot{y} = \ddot{\eta} \tag{2.71}$$

$$\ddot{z} = \ddot{\rho} \tag{2.72}$$

Thus, an expansion about L_i using a Taylor series and neglecting the higher-order terms leads to the linear variational equations, represented in second-order form as,

$$\ddot{\xi} - 2\dot{\eta} = U^*_{xx}\xi + U^*_{xy}\eta + U^*_{xz}\rho \tag{2.73}$$

$$\ddot{\eta} + 2\dot{\xi} = U^*_{yx}\xi + U^*_{yy}\eta + U^*_{yz}\rho \tag{2.74}$$

$$\ddot{\rho} = U^*_{zx}\xi + U^*_{zy}\eta + U^*_{zz}\rho \tag{2.75}$$

The partials in Eqs. (2.73)-(2.75) appear in Eqs. (2.55)-(2.60). These partials are then evaluated at the equilibrium solution and, therefore, are constant. Recall that

all the equilibrium solutions are located in the xy-plane, hence, $z = 0$. The variational equations can be reduced and expressed as,

$$\ddot{\xi} - 2\dot{\eta} = U^*_{xx}\xi + U^*_{xy}\eta \tag{2.76}$$

$$\ddot{\eta} + 2\dot{\xi} = U^*_{yx}\xi + U^*_{yy}\eta \tag{2.77}$$

$$\ddot{\rho} = U^*_{zz}\rho \tag{2.78}$$

Note, from the variational equations, that the in-plane and out-of-plane linearized motions are decoupled, and therefore, can be examined separately. The out-of-plane motion is governed by the ordinary differential equation in Eq. (2.78), with the general form of the solution known to be sinusoidal, that is,

$$\zeta = C_1 cos(\nu\tau) + C_2 sin(\nu\tau) \tag{2.79}$$

where $\nu = \sqrt{|U_{zz}|_{L_i}}$ is the out-of-plane frequency, and C_1 and C_2 are the coefficients to be determined from the initial conditions. The eigenvalues of the characteristic equation corresponding to Eq. (2.78) are pure imaginary, which implies that the linear solution is marginally stable. The in-plane motion is governed by the coupled system of linear ordinary differential equations in Eqs. (2.76)-(2.77). This system can be generally expressed in first-order form as $\dot{\bar{X}} = A\bar{X}$, where $\bar{X}$ is reduced to four elements, that is, $\bar{X} = [\xi \;\; \eta \;\; \dot{\xi} \;\; \dot{\eta}]^T$, and A is reduced to a 4x4 matrix since all the L_i are in plane. The constant matrix A is expressed in terms of the partials and other constant coefficients as,

$$A = \begin{bmatrix} 0 & 0 & 1 & 0 \\ 0 & 0 & 0 & 1 \\ U^*_{xx} & U^*_{xy} & 0 & 2 \\ U^*_{yx} & U^*_{yy} & -2 & 0 \end{bmatrix} \tag{2.80}$$

where the partials U^*_{xx} and U^*_{yy} are available in Eq. (2.55) and Eq. (2.56), respectively; recall that since all L_i are in the plane of the primaries, $U^*_{xz} = U^*_{zx} = U^*_{yz} = U^*_{zy} = 0$,

and $U^*_{xy} = U^*_{yx}$. Given that matrix A is constant, the general solution to this system possesses the form,

$$\xi = \sum_{i=1}^{4} a_i e^{\lambda_i t} \tag{2.81}$$

$$\eta = \sum_{i=1}^{4} b_i e^{\lambda_i t} \tag{2.82}$$

where a_i and b_i are constants of integration (b_i is dependent on a_i), and λ_i are the roots of the characteristic determinant of matrix A. The characteristic equation is generally represented for any of the five equilibrium solutions by the fourth-order polynomial,

$$\lambda^4 + \left(4 - U^*_{xx} - U^*_{yy}\right)\lambda^2 + \left(U^*_{xx}U^*_{yy} - U^*_{yx}U^*_{xy}\right) = 0 \tag{2.83}$$

The stability of the equilibriums solutions is assessed by investigating the roots of this characteristic polynomial. Consider the collinear points L_1, L_2, and L_3. The y and z components corresponding to the collinear points are zero, that is, $y_{L_i} = z_{L_i}$, and thus, $U^*_{xy} = 0$, $U^*_{xx} > 0$, and $U^*_{yy} < 0$. The eigenvalues are determined and written as,

$$\lambda_{1,2} = \pm\sqrt{\Lambda_1} \tag{2.84}$$

$$\lambda_{3,4} = \pm\sqrt{\Lambda_2} \tag{2.85}$$

where the coefficients Λ_1, Λ_2, β_1, and β_2 are expressed as,

$$\Lambda_{1,2} = -\beta_1 \pm \left(\beta_1^2 + \beta_2^2\right)^{\frac{1}{2}} \tag{2.86}$$

$$\beta_1 = 2 - \frac{U^*_{xx} + U^*_{yy}}{2} \tag{2.87}$$

$$\beta_2 = -U^*_{xx}U^*_{yy} \tag{2.88}$$

The eigenvalues associated with the collinear points possess real and imaginary parts. At least one eigenvalue includes a positive real part, and thus, L_1, L_2, and L_3 are unstable. In general, one term generates unbounded values for ξ and η as $t \to \infty$. However, even though the solution L_i may be unstable by this definition of stability, it is desirable to investigate the motion in the vicinity of these equilibrium points. With

the appropriate selection of the initial conditions, ξ_0 and η_0, the divergent motion can be suppressed in the linear system, resulting in an ellipse about the libration point, L_i, with semi-major and semi-minor axes parallel to the y-axis and x-axis, respectively. Because of the instability, however, these ellipses are not periodic in the real system, and the motion will quickly diverge if propagated in the non-linear EOMs. Nonetheless, a periodic solution in the non-linear system can be determined with a numerical corrections process.

2.4 Differential Corrections - Single Shooting Method

The existence of periodic motion in the CR3BP is well-known, and identifying periodic motion in the vicinity of the libration points is useful as it provides valuable insight on these regions. The computation of this periodic motion in the non-linear system involves the use of a multi-dimensional version of a Newton-Raphson differential corrections process or "shooting method". With the availability of the appropriate mathematical model, that is, the equations of motion and the state transition matrix, the non-linear differential equations are easily numerically integrated to any future time. The configuration states are plotted as necessary to aid in visualizing the trajectory. The STM, $\Phi(\tau, \tau_0)$, associated with a trajectory arc predicts adjustments in the initial state to shift the final state to a desired set of values at the end point. The diagram in Fig. 2.12 illustrates a reference trajectory arc, as well as a perturbed path relative to the reference. The vectors $\bar{r}(\tau_i), \bar{v}(\tau_i)$ represent the position and velocity at time τ_i along the reference trajectory. The vector $\bar{r}_d(\tau_i)$ denotes the position state along the perturbed path. This state, i.e., $\bar{r}_d(\tau_i)$, might represent some desired state; the initial state on the reference is modified to deliver the vehicle to $\bar{r}_d$. At any time τ_i, $\delta\bar{X}(\tau_i)$ is the six-element variational vector representing the perturbed state relative to the reference. Note that the variational vector includes six elements, that is, variations in both position and velocity. To first-order, the variation at time τ_i can

be expressed in terms of a variation at the initial time, i.e., $\delta\bar{X}(\tau_i) = \Phi(\tau_i, \tau_0)\delta\bar{X}_0$, in terms of the STM.

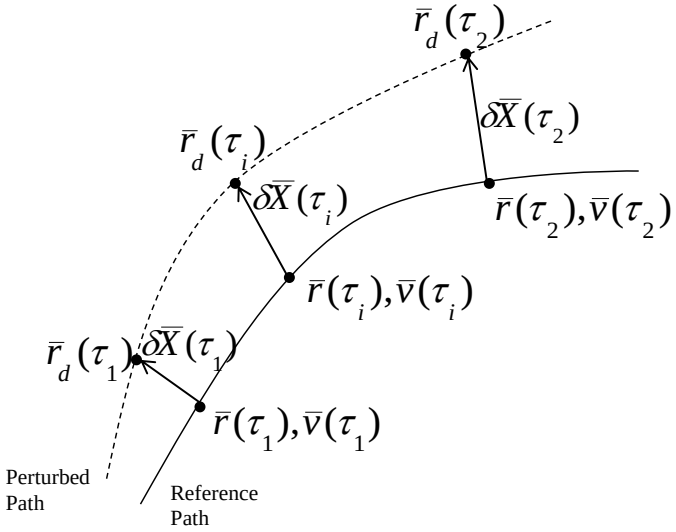

Fig. 2.12. Perturbed Path Relative to the Reference Trajectory Arc

Since the differential equations are non-linear and a solution for $\delta\bar{X}(\tau_i)$ is based upon a linear expansion, the variation $\delta\bar{X}(\tau_i)$ is clearly an approximation. Generally, the closer the perturbed state to the reference, the more accurate the approximation. For some applications, the reference is redefined (or "rectified") to maintain accuracy. But, if the variations are sufficiently small, the approximation can be employed to adjust the initial state such that the path evolves and reaches some desired state downstream. This process is the basis for all simple targeters. For example, with a suitable initial guess, this strategy is very effective to determine the appropriate initial position and velocity that produce a periodic orbit. In practice, if a periodic orbit is assumed to exist near the reference, it can be computed to a reasonable level of accuracy in a just a few iterations. To determine a specific initial state that yields a periodic orbit, that is, a periodic solution to the non-linear differential equations, the linear variational equation is employed to modify the initial conditions appropriately. To be periodic, an orbit must repeat for greater than one period and frequently

possesses a plane of symmetry. Assuming that the derivative is continuous and there are no singularities, the trajectory intersects the symmetry plane perpendicularly. Two types of periodic orbits that are known to exist near the libration points are Lyapunov and halo orbits, both of which are symmetric across the xz-plane.

The computation of periodic orbits that are symmetric across the xz-plane is simplified by observations concerning the crossing conditions. Specifically, to further simplify the problem and exploit the symmetry properties across the xz-plane, only half of the orbit is investigated. It is also convenient, but not required, to initiate the integration using a point in the plane of symmetry. Therefore, the initial conditions are defined in terms of a state vector of the form $\bar{X}_0 = [x_0 \ 0 \ z_0 \ 0 \ \dot{y}_0 \ 0]^T$. At the desired final endpoint, the state vector is also written in the same form, that is, $\bar{X}_f = [x_f \ 0 \ z_f \ 0 \ \dot{y}_f \ 0]^T$ since the initial and final states occur in the plane of symmetry. Thus, only six quantities are necessary to completely define the problem. Consequently, the number of unknowns is reduced by half, that is, $x_0, z_0, \dot{y}_0, x_f, z_f, \dot{y}_f$, plus τ_f, the time when the path re-crosses the plane perpendicularly, equal to one half of the orbit period. The number of unknowns can be further reduced to four, that is $x_0, z_0, \dot{y}_0$, and τ_f, by enforcing a stopping condition at the xz-plane crossing, i.e., $y_f = 0$. If $\dot{x}_f$ and $\dot{z}_f$ are also zero, the final state possesses the form $\bar{X}_f = [x_f \ 0 \ z_f \ 0 \ \dot{y}_f \ 0]^T$ and a periodic orbit is determined and, thus, $\tau_f + \delta\tau_f$, exactly half the period. If $\dot{x}_f$ and $\dot{z}_f$ are not exactly zero, an iteration process is triggered. It is assumed that a guess corresponding to these four initial quantities is initially available. An initial guess that is close to the desired initial state results in a periodic orbit after only a few iterations. Of course, it is also known that there exists an infinite number of periodic orbits [9]. In addition, then, a successful iteration sequence requires a good update process to identify the specified orbit that meets the goal. The final state, $\bar{X}_f$, is a function of the initial state and the time interval τ_f. The impact of a change in the

initial conditions $(x_0, y_0, z_0, \dot{x}_0, \dot{y}_0, \dot{z}_0)$ on the final states at τ_f can be investigated via the linear variational relationships in Eq. (2.63), repeated here in scalar form, that is,

$$\delta x_f = \frac{\partial x}{\partial x_0}\delta x_0 + \frac{\partial x}{\partial y_0}\delta y_0 + \frac{\partial x}{\partial z_0}\delta z_0 + \frac{\partial x}{\partial \dot{x}_0}\delta \dot{x}_0 + \frac{\partial x}{\partial \dot{y}_0}\delta \dot{y}_0 + \frac{\partial x}{\partial \dot{z}_0}\delta \dot{z}_0 + \frac{\partial x}{\partial \tau}\delta\tau \tag{2.89}$$

$$\delta y_f = \frac{\partial y}{\partial x_0}\delta x_0 + \frac{\partial y}{\partial y_0}\delta y_0 + \frac{\partial y}{\partial z_0}\delta z_0 + \frac{\partial y}{\partial \dot{x}_0}\delta \dot{x}_0 + \frac{\partial y}{\partial \dot{y}_0}\delta \dot{y}_0 + \frac{\partial y}{\partial \dot{z}_0}\delta \dot{z}_0 + \frac{\partial y}{\partial \tau}\delta\tau \tag{2.90}$$

$$\delta z_f = \frac{\partial z}{\partial x_0}\delta x_0 + \frac{\partial z}{\partial y_0}\delta y_0 + \frac{\partial z}{\partial z_0}\delta z_0 + \frac{\partial z}{\partial \dot{x}_0}\delta \dot{x}_0 + \frac{\partial z}{\partial \dot{y}_0}\delta \dot{y}_0 + \frac{\partial z}{\partial \dot{z}_0}\delta \dot{z}_0 + \frac{\partial z}{\partial \tau}\delta\tau \tag{2.91}$$

$$\delta \dot{x}_f = \frac{\partial \dot{x}}{\partial x_0}\delta x_0 + \frac{\partial \dot{x}}{\partial y_0}\delta y_0 + \frac{\partial \dot{x}}{\partial z_0}\delta z_0 + \frac{\partial \dot{x}}{\partial \dot{x}_0}\delta \dot{x}_0 + \frac{\partial \dot{x}}{\partial \dot{y}_0}\delta \dot{y}_0 + \frac{\partial \dot{x}}{\partial \dot{z}_0}\delta \dot{z}_0 + \frac{\partial \dot{x}}{\partial \tau}\delta\tau \tag{2.92}$$

$$\delta \dot{y}_f = \frac{\partial \dot{x}}{\partial x_0}\delta x_0 + \frac{\partial \dot{y}}{\partial y_0}\delta y_0 + \frac{\partial \dot{y}}{\partial z_0}\delta z_0 + \frac{\partial \dot{y}}{\partial \dot{x}_0}\delta \dot{x}_0 + \frac{\partial \dot{y}}{\partial \dot{y}_0}\delta \dot{y}_0 + \frac{\partial \dot{y}}{\partial \dot{z}_0}\delta \dot{z}_0 + \frac{\partial \dot{y}}{\partial \tau}\delta\tau \tag{2.93}$$

$$\delta \dot{z}_f = \frac{\partial \dot{z}}{\partial x_0}\delta x_0 + \frac{\partial \dot{z}}{\partial y_0}\delta y_0 + \frac{\partial \dot{z}}{\partial z_0}\delta z_0 + \frac{\partial \dot{z}}{\partial \dot{x}_0}\delta \dot{x}_0 + \frac{\partial \dot{z}}{\partial \dot{y}_0}\delta \dot{y}_0 + \frac{\partial \dot{z}}{\partial \dot{z}_0}\delta \dot{z}_0 + \frac{\partial \dot{z}}{\partial \tau}\delta\tau \tag{2.94}$$

Recall that these partial derivatives are all evaluated at time τ_f. The partial derivatives with respect to the components of the state vector are actually elements of the state transition matrix and evaluated at time τ_f, i.e., $\phi(\tau_f, \tau_0)$. Since there is only one independent variable, $\frac{\partial}{\partial t} = \frac{d}{dt}$. Thus,

$$\frac{\partial x}{\partial \tau} = \frac{dx}{dt} = \dot{x}|_{\tau_f} \tag{2.95}$$

$$\frac{\partial y}{\partial \tau} = \frac{dy}{dt} = \dot{y}|_{\tau_f} \tag{2.96}$$

$$\frac{\partial z}{\partial \tau} = \frac{dz}{dt} = \dot{z}|_{\tau_f} \tag{2.97}$$

$$\frac{\partial \dot{x}}{\partial \tau} = \frac{d\dot{x}}{dt} = \ddot{x}|_{\tau_f} \tag{2.98}$$

$$\frac{\partial \dot{y}}{\partial \tau} = \frac{d\dot{y}}{dt} = \ddot{y}|_{\tau_f} \tag{2.99}$$

$$\frac{\partial \dot{z}}{\partial \tau} = \frac{d\dot{z}}{dt} = \ddot{z}|_{\tau_f} \tag{2.100}$$

where the vertical bar indicates state evaluation at the final time, τ_f. Thus, the linear variational equations representing the six scalar equations can be written in vector form as,

$$\delta \bar{X} = \Phi(\tau_f, 0)\delta \bar{X}_0 + \dot{\bar{X}}|_{\tau_f}\delta\tau_f \tag{2.101}$$

or expressed in matrix form as,

$$\begin{bmatrix} \delta x \\ \delta y \\ \delta z \\ \delta \dot{x} \\ \delta \dot{y} \\ \delta \dot{z} \end{bmatrix}_{\tau_f} = \begin{bmatrix} \phi_{11} & \phi_{12} & \phi_{13} & \phi_{14} & \phi_{15} & \phi_{16} \\ \phi_{21} & \phi_{22} & \phi_{23} & \phi_{24} & \phi_{25} & \phi_{26} \\ \phi_{31} & \phi_{32} & \phi_{33} & \phi_{34} & \phi_{35} & \phi_{36} \\ \phi_{41} & \phi_{42} & \phi_{43} & \phi_{44} & \phi_{45} & \phi_{46} \\ \phi_{51} & \phi_{52} & \phi_{53} & \phi_{54} & \phi_{55} & \phi_{56} \\ \phi_{61} & \phi_{62} & \phi_{63} & \phi_{64} & \phi_{65} & \phi_{66} \end{bmatrix}_{\tau_f} \begin{bmatrix} \delta x_0 \\ \delta y_0 \\ \delta z_0 \\ \delta \dot{x}_0 \\ \delta \dot{y}_0 \\ \delta \dot{z}_0 \end{bmatrix} + \begin{bmatrix} \dot{x} \\ \dot{y} \\ \dot{z} \\ \ddot{x} \\ \dot{y} \\ \dot{z} \end{bmatrix}_{\tau_f} (\delta \tau_f) \quad (2.102)$$

where the subscript τ_f indicates that the corresponding quantities are evaluated at the final time.

The matrix Eq. (2.102) can be further reduced. Recall that the initial state is integrated until $y_f = 0$, the "stopping condition", and the corresponding time is defined as τ_f. The desired final value for y is zero, so $\delta y_f = 0$. Since a perpendicular crossing of the xz-plane is enforced, the final desired values for $\dot{x}$ and $\dot{z}$ are zero, that is, $\dot{x}_f = \dot{z}_f = 0$, and consequently $\delta \dot{x}_f = \delta \dot{z}_f = 0$ after convergence. However, these values are not zero until the iterative process is complete and the algorithm converges to the desired final values (to within some acceptable tolerance). To achieve these desired values, the changes in $\dot{x}$ and $\dot{z}$ in Eq. (2.102) are specified such that $\delta \dot{x}_f = -\dot{x}_f$ and $\delta \dot{z}_f = -\dot{z}_f$, respectively. Equations (2.90), (2.92), and (2.94) are used to solve for the unknown variables, that is, the changes in the initial states, δx_0, δz_0, and $\delta \dot{y}_0$ to target a perpendicular crossing; the goal of this iterative process is to improve the initial guess for the initial state by correcting the values for $x_0, z_0, \dot{y}_0$. Recall that the initial state possesses the form $[x_0\ 0\ z_0\ 0\ \dot{y}_0\ 0]^T$, so $\delta y_0 = \delta \dot{x}_0 = \delta \dot{z}_0 = 0$. Substituting these values into matrix equation (2.102) leads to the following scalar equations,

$$\delta y_f = \phi_{21} \delta x_0 + \phi_{23} \delta z_0 + \phi_{25} \delta \dot{y}_0 + \dot{y}_f \delta \tau_f \quad (2.103)$$

$$\delta \dot{x}_f = \phi_{41} \delta x_0 + \phi_{43} \delta z_0 + \phi_{45} \delta \dot{y}_0 + \ddot{x}_f \delta \tau_f \quad (2.104)$$

$$\delta \dot{z}_f = \phi_{61} \delta x_0 + \phi_{63} \delta z_0 + \phi_{65} \delta \dot{y}_0 + \ddot{z}_f \delta \tau_f \quad (2.105)$$

which can be expressed in matrix form as,

$$\begin{pmatrix} \delta y_f \\ \delta \dot{x}_f \\ \delta \dot{z}_f \end{pmatrix} = \begin{pmatrix} \phi_{21} & \phi_{23} & \phi_{25} & \dot{y}_f \\ \phi_{41} & \phi_{43} & \phi_{45} & \ddot{x}_f \\ \phi_{61} & \phi_{63} & \phi_{65} & \ddot{z}_f \end{pmatrix} \begin{pmatrix} \delta x_0 \\ \delta z_0 \\ \delta \dot{y}_0 \\ \delta \tau_f \end{pmatrix} \tag{2.106}$$

This system results in a set of three equations in the four unknowns $\delta x_0, \delta z_0, \delta \dot{y}_0, \delta \tau_f$. There are various available options to solve this system of equations. The option employed in this analysis involves reducing the number of unknowns to three by arbitrarily selecting one initial condition and constraining it to be fixed throughout the simulation. For example, select x_0 and fix the value throughout the integration, such that $\delta x_0 = 0$. Equation (2.106) reduces to three equations in three unknowns,

$$\begin{bmatrix} \delta y \\ \delta \dot{x} \\ \delta \dot{z} \end{bmatrix}_{\tau_f} = \begin{pmatrix} \phi_{23} & \phi_{25} & \dot{y}_f \\ \phi_{43} & \phi_{45} & \ddot{x}_f \\ \phi_{63} & \phi_{65} & \ddot{z}_f \end{pmatrix} \begin{bmatrix} \delta z_0 \\ \delta \dot{y}_0 \\ \delta \tau_f \end{bmatrix} \tag{2.107}$$

Thus, the matrix in Eq. (2.107) is square and can be inverted to solve for $\delta z_0, \delta \dot{y}_0$, and $\delta \tau_f$. The system is then integrated with the updated initial conditions. Since this is a linear corrections process for a non-linear problem, the process is iterative. This procedure is repeated until the values for $\dot{x}$ and $\dot{z}$ are zero to within a specified tolerance. The problem is further reduced, to a 2x2 matrix inversion, by exploiting the information concerning the variation in the period, $\delta \tau_f$. Recall that $\delta y_f = 0$ because this statement represents the stopping condition. Therefore, if Eq. (2.103) for $\delta y_f = 0 = \phi_{21}\delta x_0 + \phi_{23}\delta z_0 + \phi_{25}\delta \dot{y}_0 + \dot{y}_f \delta \tau_f$ is inverted to solve for $\delta \tau_f$, the result is,

$$\delta \tau_f = -\frac{\phi_{21}\delta x_0 + \phi_{23}\delta z_0 + \phi_{25}\delta \dot{y}_0}{\dot{y}_f} \tag{2.108}$$

This expression is substituted into Eq. (2.107) to yield,

$$\begin{pmatrix} \delta \dot{x}_f \\ \delta \dot{z}_f \end{pmatrix} = \left[\begin{pmatrix} \phi_{43} & \phi_{45} \\ \phi_{63} & \phi_{65} \end{pmatrix} - \frac{1}{\dot{y}_f} \begin{pmatrix} \ddot{x} \\ \ddot{z} \end{pmatrix} \begin{pmatrix} \phi_{23} & \phi_{25} \end{pmatrix} \right] \begin{pmatrix} \delta z_0 \\ \delta \dot{y}_0 \end{pmatrix} \tag{2.109}$$

The matrix Eq. (2.109) is inverted to produce new values for the appropriate set of initial conditions given a fixed value of x_0, that is,

$$\begin{pmatrix} \delta z_0 \\ \delta \dot{y}_0 \end{pmatrix} = \left[\begin{pmatrix} \phi_{43} & \phi_{45} \\ \phi_{63} & \phi_{65} \end{pmatrix} - \frac{1}{\dot{y}_f} \begin{pmatrix} \ddot{x} \\ \ddot{z} \end{pmatrix} \begin{pmatrix} \phi_{23} & \phi_{25} \end{pmatrix} \right]^{-1} \begin{pmatrix} \delta \dot{x}_f \\ \delta \dot{z}_f \end{pmatrix} \tag{2.110}$$

Similarly, if the value of z_0 is fixed throughout the process, the initial variations are computed as,

$$\begin{pmatrix} \delta x_0 \\ \delta \dot{y}_0 \end{pmatrix} = \left[\begin{pmatrix} \phi_{41} & \phi_{45} \\ \phi_{61} & \phi_{65} \end{pmatrix} - \frac{1}{\dot{y}_f} \begin{pmatrix} \ddot{x} \\ \ddot{z} \end{pmatrix} \begin{pmatrix} \phi_{21} & \phi_{25} \end{pmatrix} \right]^{-1} \begin{pmatrix} \delta \dot{x}_f \\ \delta \dot{z}_f \end{pmatrix} \tag{2.111}$$

After this iteration process is complete, a perpendicular crossing is assumed and a periodic orbit in the CR3BP is determined.

Independent of the option selected to compute a periodic orbit, the basis for the targeting algorithm is the same: a multi-dimensional Newton-Raphson method that generally converges to a solution within three to four iterations. Numerical examples of periodic orbits appear in the following sections.

2.4.1 Planar Periodic Orbits in the CR3BP: Lyapunov Orbits

2.4.1.1 Sample Lyapunov Orbits

There are an infinite number of periodic orbits in the CR3BP. A planar, periodic orbit is a straightforward example for introducing the computational process. As an example, a Lyapunov orbit is a periodic orbit in the plane of motion of the primaries, that is, a planar orbit in the xy-plane that is symmetric across the x-axis. In the planar problem, the 2x2 matrix inverse in Eq. (2.110) and Eq. (2.111) is reduced to one equation in one unknown since $\delta z_0 = \delta \dot{z}_0 = 0$. Therefore, the variation in the initial y-component of velocity to target a perpendicular crossing of the x-axis is evaluated as,

$$\delta \dot{y}_0 = \delta \dot{x}_f \frac{\dot{y}_f}{\phi_{45}\dot{y}_f - \phi_{25}\ddot{x}_f} \tag{2.112}$$

where ϕ_{45} and ϕ_{25} are components of the STM. Equation (2.112) is then employed in the targeting algorithm to compute a planar periodic orbit in the vicinity of one of the Lagrange points. As a first numerical example, a Lyapunov orbit in the vicinity of L_1 in the Earth-Moon system appears in Fig. 2.13. Each Lyapunov orbit is uniquely characterized by the parameter A_y, that is, the maximum y-excursion as measured from the x-axis. In particular, the planar, periodic orbit plotted in Fig. 2.13 is characterized by a y-amplitude of 15,267 km and a period of 11.798 days. The Earth, although it does not appear in Fig. 2.13 at this scale, is located to the left at a distance of 317,029.76 km from the location of L_1. The distance between L_1 and the Moon is equal to 58,017.33 km, and the mass fraction for this system is equal to a value of $\mu = 0.01215057$. (Both the Earth and the Moon are sized to the correct scale.)

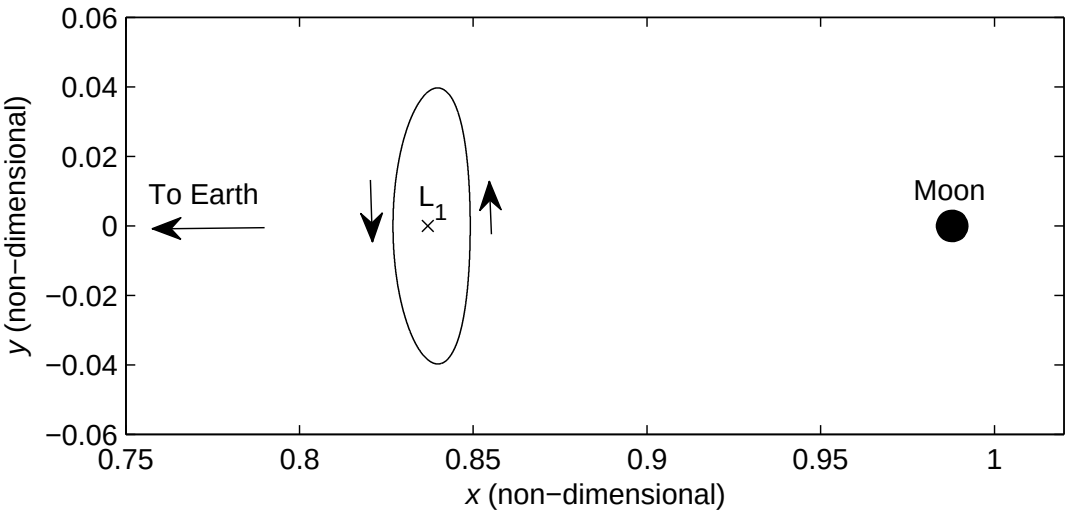

Fig. 2.13. Planar Periodic Orbit near L_1 in the Earth-Moon System (Characteristic Distance $l^* = 384,388.174$ km)

It is often desirable to identify a group of related periodic orbits rather than a single trajectory. A continuation method is used to generate a family of planar periodic orbits in the vicinity of the libration point. This continuation process was first introduced by Henri Poincaré in 1892 [9]. In a family of periodic orbits, 'continuation'

is a technique used to compute multiple trajectories by determining each orbit using Eq. (2.107) and a corrections process. In developing Eq.(2.107), x_0 is selected as fixed and the result is Eq. (2.110). But, it is not necessary that the constrained quantity be a state; rather, Jacobi constant or a perturbation parameter are equally valid. Once periodicity is determined and the first orbit is computed, the value of the constraining parameter is modified and the process repeats to determine a second orbit. In general, the initial velocity from the first orbit is employed as the initial guess to target the the second periodic orbit. Let the initial state representing the first Lyapunov orbit in the family be $\bar{X}_1(\tau_0) = [x_1, y_1, z_1, \dot{x}_1, \dot{y}_1, \dot{z}_1]$, and define $\Delta X(\tau_0)$ as a fixed step in the x-direction where $x(\tau_0)$ is the fixed quantity in the determination of each orbit. Then, the initial guess for the initial state corresponding to the next Lyapunov orbit in the family is obtained by adding the fixed step $\Delta X(\tau_0)$ to the x-component of $\bar{X}_1(\tau_0)$, that is, $\bar{X}_2(\tau_0) = [x_1 + \Delta X(\tau_0), y_1, z_1, \dot{x}_1, \dot{y}_1, \dot{z}_1]$. The differential corrections process is applied to obtain the correct initial state for this second periodic, Lyapunov orbit in the family, and the process is continued to generate additional orbits in the family. The fixed step is applied in any direction. However, maintaining a minimum distance from the closest primary during any simulation avoids numerical issues that arise when approaching a singularity. Representative members of a family of Lyapunov orbits in the vicinity of L_1 appear in Fig. 2.14, although there are an infinite number of periodic orbits in each family.

Planar periodic orbits can also be computed in the vicinity of all other Lagrange points. As representative examples, families of L_2 and L_3 Lyapunov orbits are computed using a corrections process with continuation again in the x-direction, and are plotted in Figs. 2.15 and 2.16, respectively. Representative members of the L_2 Lyapunov family appear in Fig. 2.15, and Fig. 2.16 includes representative members in a family of Lyapunov orbits in the vicinity of L_3. In the Earth-Moon system, the distance between L_3 and the Earth is equal to 391,004.72 km.

For completeness, Table 2.2 includes the non-zero initial conditions and corresponding values of the Jacobi constant associated with the smallest and largest mem-

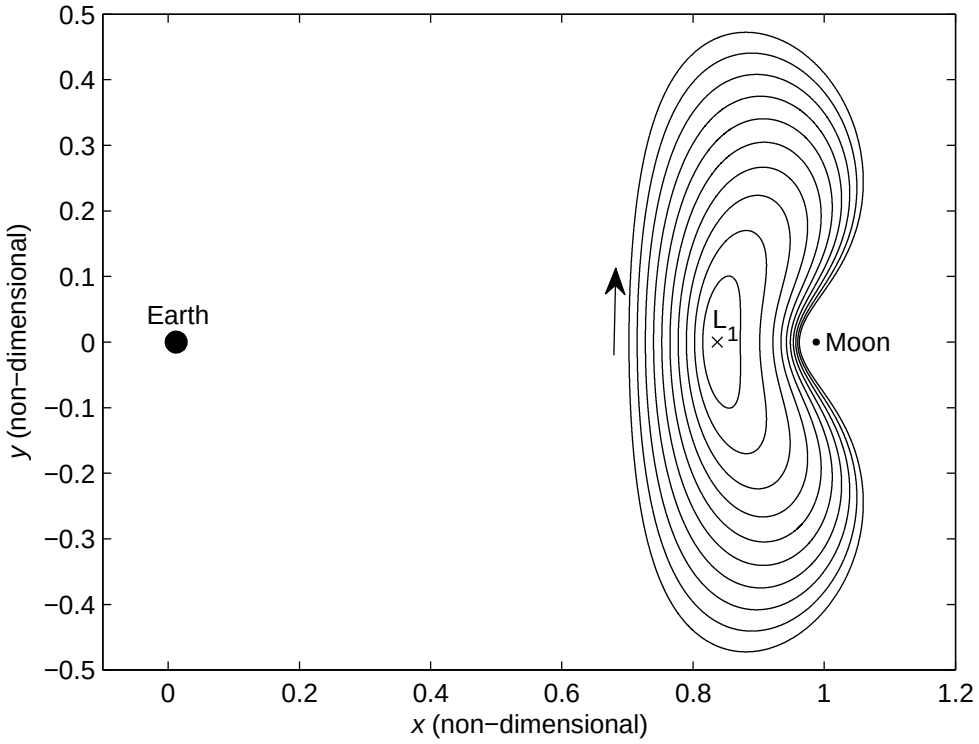

Fig. 2.14. Family of Planar Periodic Orbits Emanating from the Vicinity of L_1 in the Earth-Moon System (Characteristic Distance $l^* = 384,388.174$ km)

bers that are plotted in each of the three families of planar, periodic orbits in the vicinity of the collinear points as represented in Figs. 2.14-2.16. The initial y-component of position and the initial x-component of velocity are zero for each periodic orbit in the family, i.e., $y_0 = \dot{x}_0 = 0$. Recall that these orbits are all planar; thus, $z = \dot{z} = 0$. For comparison, the three planar periodic orbit families near L_1, L_2, and L_3 are plotted in Fig. 2.17. Notice the relative size of the orbits in the L_3 Lyapunov family, plotted in magenta, versus the size of the orbits in the L_1 and L_2 Lyapunov families, plotted in green and blue, respectively. Families of Lyapunov orbits also exist in the vicinity of the equilateral points L_4 and L_5 for all values of μ. Examples of short and long period planar solutions have been computed by various researchers [33].

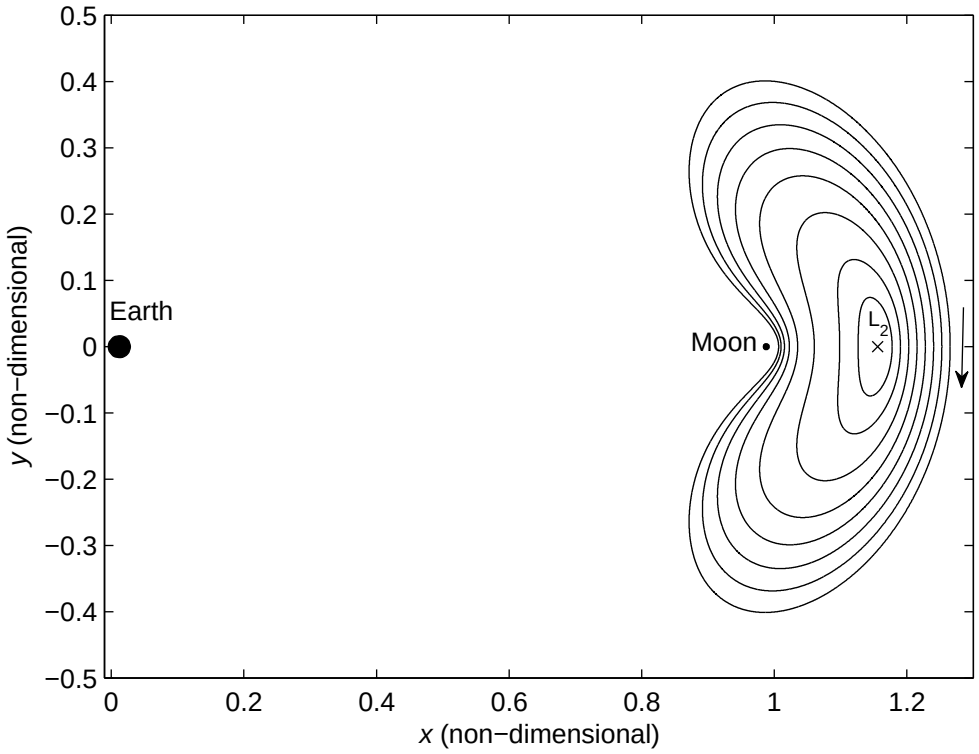

Fig. 2.15. Family of Planar Periodic Orbits near L_2 in the Earth-Moon System

Table 2.2
Initial Conditions and Jacobi Constant (JC) Values Corresponding to the Smallest and Largest Lyapunov Orbits that Appear in Figs. 2.14-2.16

Lyapunov orbit	x (km)	$\dot{y}$ (km/sec)	Period (days)	JC
Small L_1	313,243.763	0.213679	12.4437	3.145484
Large L_1	270,000.094	0.617882	25.1819	2.942655
Small L_2	452,687.076	-0.136258	14.7755	3.157746
Large L_2	489,203.952	-0.547656	24.6174	2.957027
Small L_3	-426,502.757	0.211343	27.0037	3.000490
Large L_3	-754,770.257	1.881937	27.2660	1.502348

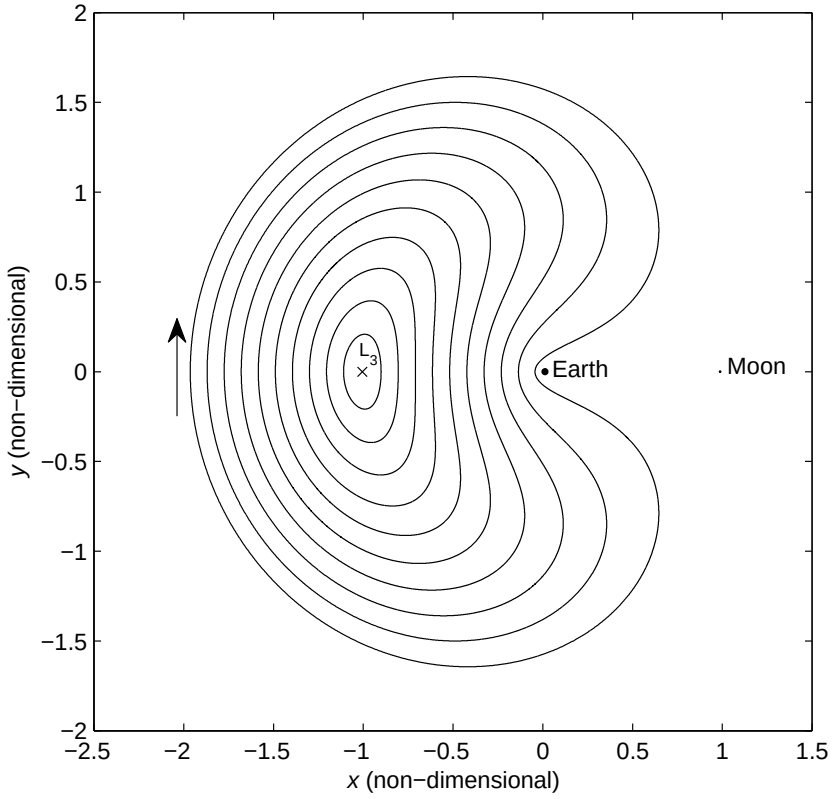

Fig. 2.16. Family of Planar Periodic Orbits near L_3 in the Earth-Moon System

2.4.1.2 Orbital Stability

For astrodynamics applications, the stability of any trajectory or periodic orbit is frequently critical in judging its suitability. Unlike the libration points, however, a Lyapunov orbit is not a constant solution. Nevertheless, the stability of each of these planar, periodic orbits in the vicinity of the collinear libration points can be assessed by investigating the eigenvalues of the corresponding monodromy matrix. The monodromy matrix is defined as the state transition matrix evaluated after exactly one orbital revolution. The eigenvalues of the monodromy matrix are computed for each periodic orbit in a family, and can be examined as the family evolves. The eigenvalues possess exactly the same value irregardless of the point along the orbit at which they

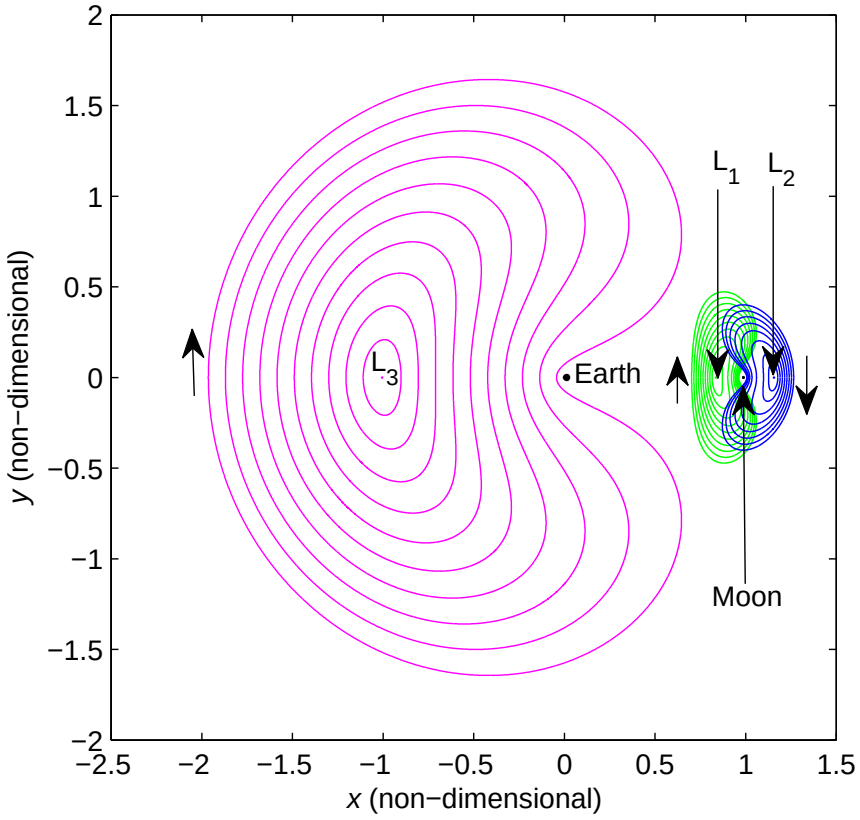

Fig. 2.17. Planar Periodic Orbits in the Vicinity of the Collinear Libration Points L_1, L_2, and L_3 in the Earth-Moon System

are computed. The eigenvalues of the monodromy matrix are also known to appear in reciprocal pairs, as stated in Lyapunov's Theorem [34] [33]:

Theorem 2.4.1 (Lyapunov's Theorem) *If λ_j is an eigenvalue of the monodromy matrix $\Phi(\tau_0+T,\tau_0)$ of a t-invariant system, then λ_j^{-1} is also an eigenvalue of $\Phi(\tau_0+T,\tau_0)$, with the same structure of elemetary divisors.*

In the CR3BP, the second-order system possesses three degrees of freedom and, thus, the monodromy matrix is defined in terms of six eigenvalues. For a periodic orbit to exist in the CR3BP, a minimum pair of eigenvalues must be equal to one because of the reciprocal nature of the eigenvalues. The monodromy matrix is a real matrix, so its eigenvalues are real or, if complex, appear in complex conjugate pairs. However,

because general complex conjugate pairs are not reciprocal, the eigenvalues of the monodromy matrix appear only in certain configurations in the complex plane, that is, in complex pairs on the unit circle. To assess the stability of a periodic orbit, it is necessary to investigate the characteristics of these eigenvalues associated with the monodromy matrix. A periodic orbit is defined as unstable if $|\lambda| > 1$, that is, the magnitude of the eigenvector goes to infinity as time goes to infinity. If $|\lambda| < 1$, the magnitude of the eigenvector approaches zero as time goes to infinity, and the trajectory is considered stable. Finally, if $|\lambda| = 1$, the magnitude of the eigenvector does not change, and the eigenvalue corresponds to the center subspace [35]. When representing these eigenvalues, the unstable λ are located outside the unit circle; the stable λ are inside, and the unity eigenvalues are on the unit circle. To illustrate this concept of the eigenvalues on the unit circle, consider the smallest Lyapunov orbit plotted in Fig. 2.14. The eigenvalues from the computed monodromy matrix are listed in Table 2.3. Notice that two of the eigenvalues are unity, and all appear in reciprocal pairs, that is, $\lambda_1 = \frac{1}{\lambda_2} = 1$, $\lambda_3 = \frac{1}{\lambda_4}$, and $\lambda_5 = \frac{1}{\lambda_6}$. These eigenvalues are represented in Fig. 2.18 on the unit circle. For the Lyapunov orbit in Fig. 2.18, two eigenvalues include positive real parts, and thus, the periodic orbit is unstable. A similar stability analysis is completed for each periodic orbit in the family to assess whether the orbits are stable or unstable, and to investigate the evolution of stability along the family.

Table 2.3
Eigenvalues of the Monodromy Matrix of the Smallest Lyapunov Orbit Plotted in Fig. 2.14

λ_1	1.000000	λ_2	1.000000
λ_3	1,796.577106	λ_4	0.000556
λ_5	0.769147	λ_6	1.300141

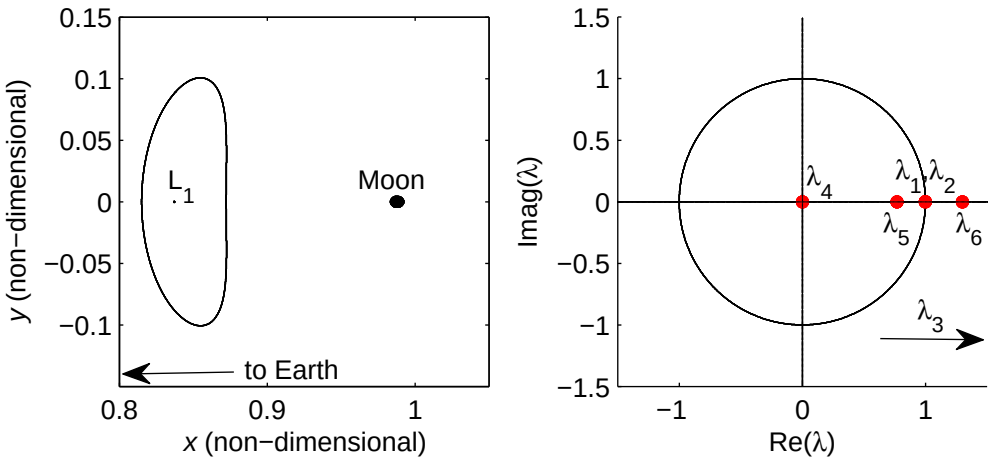

Fig. 2.18. Representation of the Eigenvalues of the Monodromy Matrix Corresponding to the Smallest Lyapunov Orbit in Fig. 2.14

2.4.2 Three-Dimensional Periodic Orbits in the CR3BP: Halo Orbits

Another example of periodic motion in the vicinity of the collinear libration points are three-dimensional, 'halo' orbits. These orbits were first introduced for astrodynamics applications by Robert Farquhar in his Ph.D. dissertation in 1968 [36]. Numerous other researchers have subsequently investigated these orbits and they have served as the basis for spacecraft trajectories in a number of successful missions [16].

Three-dimensional halo trajectories are symmetric across the xz-plane. Halo orbits bifurcate from the family of Lyapunov orbits. Thus, a common orbit exists in both the planar, periodic Lyapunov family as well as the halo family of three-dimensional periodic orbits. Hence, the two families intersect at this one single orbit, i.e., the bifurcating orbit. An abrupt change in stability, as reflected in the eigenvalues of the monodromy matrix, indicates the presence of a bifurcating orbit. The stability properties change whenever the eigenvalues depart from or arrive at the unit circle in the complex plane.

A strategy that is an extension of the scheme used to compute planar, periodic orbits, is employed to determine three-dimensional, periodic orbits. Once the bifurcat-

ing Lyapunov orbit is identified, a corrections process with continuation is employed to compute a three-dimensional halo orbit. In the corrections process to compute a *3*-D, periodic orbit, the out-of-plane component, z, is fixed at a specific value. The value of z at the initiation of the corrections process is also employed as the continuation parameter. The initial state that produces the bifurcating orbit is perturbed by a small distance Δz in the z-direction, and used as the initial guess to compute the out-of-plane halo orbit. Thus, the initial guess for the corrections process is in the form $\bar{X}_0 = [x_{bif}\ 0\ \Delta z\ 0\ \dot{y}_{bif}\ 0]^T$, and Eq.(2.111) is then used to compute the variations in the initial state to yield a three-dimensional, periodic orbit. Each halo orbit is uniquely characterized by the A_z parameter, that is, the orbit's maximum z-excursion measured relative to the xy-plane. An example of a halo orbit in the vicinity of L_1 in the Earth-Moon system appears in Fig. 2.19; this orbit possesses a z-amplitude of 38,438.81 km and a period of 11.91 days. The family of L_1 halo orbits in the Earth-Moon system is represented in Figs. 2.20-2.21.

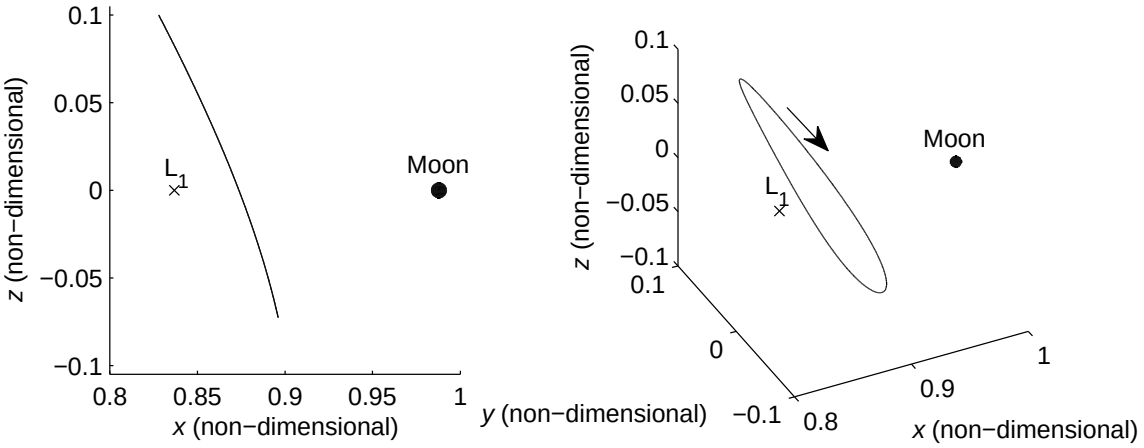

Fig. 2.19. Three-Dimensional, Periodic Orbit in the Vicinity of L_1 in the Earth-Moon System (Characteristic Distance $l^* = 384,388.174$ km)

As in the case of the planar periodic orbits, it is desirable to generate a family of three-dimensional, periodic orbits with the same characteristics. A corrections scheme with continuation is employed to generate a family of halo orbits. To compute the next orbit in the family from the previous one, a fixed step is taken in the z-direction and the corrections process is repeated at each step to yield a new three-dimensional halo orbit. The form of the mathematical model for the CR3BP lends itself to two types of analytical symmetry: time-invariance symmetry and xy-plane symmetry [37]. That is, if the independent variable, time (τ), is transformed to $t = -\tau$, it is clear that, if $[x\ y\ z\ \dot{x}\ \dot{y}\ \dot{z}]^T$ satisfies the EOMs for $\Delta\tau > 0$, then $[x\ -y\ z\ -\dot{x}\ \dot{y}\ -\dot{z}]^T$ satisfies the EOMs for $\Delta\tau < 0$, and if $[x\ y\ z\ \dot{x}\ \dot{y}\ \dot{z}]^T$ satisfies the equations of motion, then so does $[x\ y\ -z\ \dot{x}\ \dot{y}\ -\dot{z}]^T$, respectively. Thus, due to the xy-plane symmetry property, each of these out-of-plane orbits is associated with a mirror image trajectory across the xy-plane. The "northern" halo orbits extend in the positive z-direction; the "southern" halo family expands along the negative z-direction. Members of a family of northern halo orbits in the vicinity of L_1 appear in Figure 2.20. For further reference, Table 2.4 includes the non-zero initial conditions, period, and value of Jacobi constant for the smallest and largest members of the halo family in the vicinity of the collinear equilibrium point L_1 represented in Figs. 2.20-2.21. Note that the largest halo orbit plotted in these figures is not the termination of the family; it is simply the last orbit computed in the continuation process. Recall that, at a crossing of the xz-plane, $y = \dot{x} = \dot{z} = 0$ due to periodicity. As in the case of Lyapunov orbits, halo orbits also exist in the vicinity of the collinear libration points L_2 and L_3.

These families of planar and three-dimensional periodic orbits have been investigated by numerous researchers in the last three decades, and extensive literature is available on these orbits and their computation. It is also well known that these orbits exist for all values of the mass fraction μ and are now employed in a wide variety of applications in mission design.

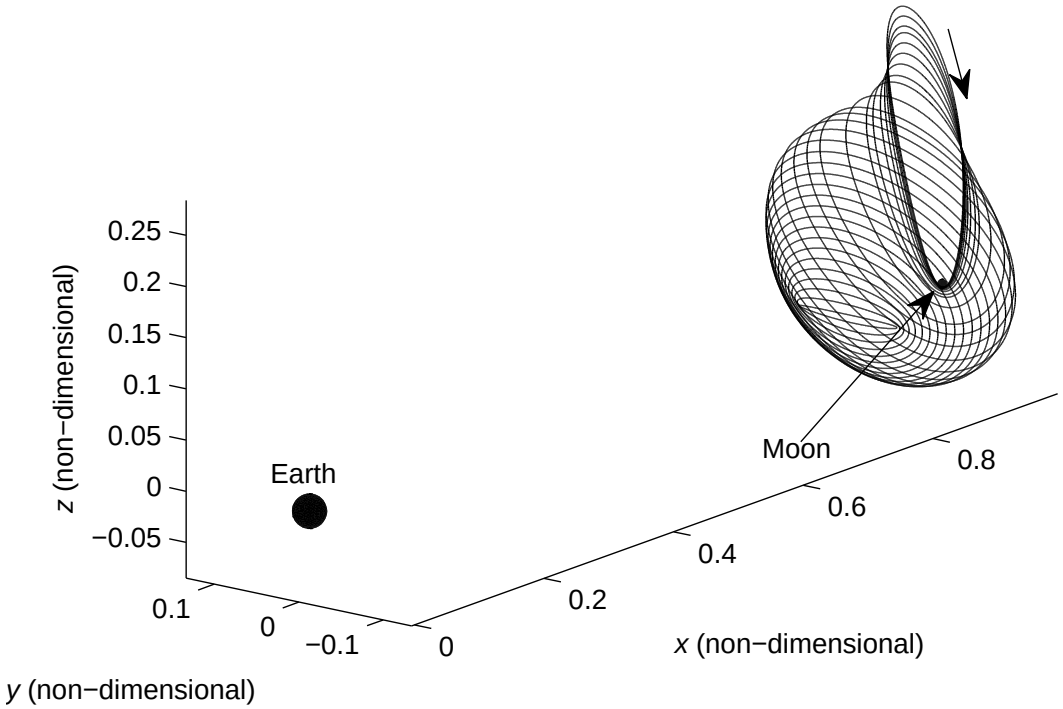

Fig. 2.20. Three-Dimensional, Periodic, Halo Orbits in the vicinity of L_1 in the Earth-Moon System

Table 2.4
Non-Zero Initial Conditions and Jacobi Constant Values of the Smallest and Largest L_1 Halo Orbits plotted in Fig. 2.20

L_1 halo orbit	x (km)	z (km)	$\dot{y}$ (km/sec)	Period (days)	JC
Smallest	316,501.721	384.388	0.129446	11.9108	3.174344
Largest	357,667.009	109,222.587	0.083816	9.1858	3.030422

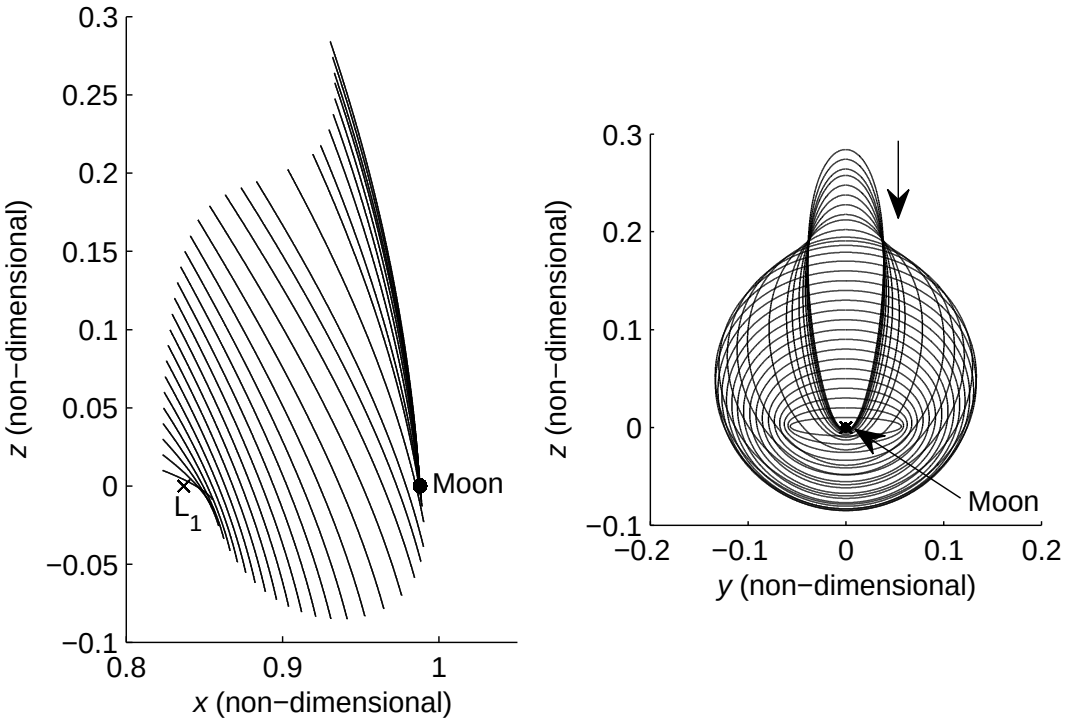

Fig. 2.21. Two-Dimensional Views of a Family of Halo Orbits near L_1 in the Earth-Moon System

3. BACKGROUND - RESONANT ORBITS AND MAPS

The main focus of this investigation is the use of Poincaré sections as valuable tools to analyze the invariant manifold structure of planar, unstable resonant orbits. Thus, some background in resonant orbits is necessary, starting with their definition in the two-body model and, subsequently, their computation in the CR3BP. A mathematical background in invariant manifold theory and Poincaré sections is also included, as well as numerical strategies for the computation of resonant orbits, the associated invariant manifolds, and Poincaré sections within the context of the CR3BP.

3.1 Resonant Orbits

The solar system possesses a high degree of structure. Under Newton's laws of motion, subtle gravitational effects determine this dynamical structure. One result is the phenomenon of resonance. The main focus of this investigation is the wide array of resonant orbits in Sun-planet and well as planet-moon systems. Resonant orbits are, by definition, periodic. In contrast to Lyapunov or halo orbits, however, resonant orbits are not directly related to the Lagrange equilibrium points. The different types of resonances are introduced here, as well as a method to compute resonant orbits in the two-body and three-body models.

3.1.1 Concept of Resonance

A resonance exists when there is a simple numerical relationship between frequencies or periods [38]. Resonances occur under different conditions, such as mean motion resonance, Laplace resonance, secular resonance, and Kozai resonance. However, the focus of this investigation is orbit-orbit resonance, when the periods involved repre-

sent the orbits of two or more bodies. Consider two bodies of arbitrary mass, denoted as A and B and consider the relationship that may exist between the periods of their motion. An orbit-orbit resonance is defined by the ratio p:q, where p indicates the period of motion for body B and q represents the period of motion for body A in resonance with body B. These 'periods' p and q can be rotational and orbital periods of a single body, as in the case of spin-orbit coupling (the orbital period of our Moon is equal to its rotational period), or the orbital periods of two or more bodies, as in the case of orbit-orbit coupling (Neptune and Pluto are in a 3:2 resonance.) In addition to the resonances involving their orbital periods, some of the planets in the solar system are also involved in long-term or secular resonances associated with the precession of the planetary orbits in space [38].

Orbit-orbit resonance does not occur only for Sun-planet systems. Many of the moons in the Saturn and Jupiter systems are in resonance. For example, three of the satellites in the Jupiter system possess orbital periods that are related by an integer ratio. Io is in a 2:1 resonance with Europa, but Europa is also in a 2:1 resonance with Ganymede. These three satellites together move in a configuration labeled as a Laplace resonance. In a Laplace resonance, three or more orbiting bodies possess a simple integer ratio between their orbital periods. In this case, Ganymede, Europa, and Io are in a 1:2:4 orbital resonance. The Saturn system has the widest variety of resonant phenomena. Mimas and Tethys share a 4:2 orbit-orbit resonance, Enceladus and Dione share a 2:1 orbit-orbit resonance and Titan and Hyperion share a 4:3 orbit-orbit resonance. Moreover, almost all the gaps between Saturn's rings can be explained by resonant effects.

3.1.2 Resonant Orbits in the Two-Body Model

The focus of this investigation is orbit-orbit resonance, also known as mean motion orbital resonance. To introduce these types of resonant orbits, some important

definitions and concepts are more easily discussed within the context of the two-body problem.

In the two-body problem, there are three types of conic sections: ellipses, parabolas, and hyperbolas. Parabolic and hyperbolic trajectories escape the vicinity of the attractive center, and therefore, are not of interest in the discussion of resonant trajectories, which, by definition, repeat a given configuration. Elliptical orbits, however, are closed and periodic relative to the inertial frame. Circular orbits are a special case of elliptical orbits, and are considered as such.

To investigate conic resonance, consider two bodies, A and B, in orbit about a primary body. The primary represents a planet or the Sun; thus, body A is a 'massless' second planet or moon. Body B then models a spacecraft, moon, or asteroid, of much smaller mass than the primary body. Body B is defined to be in orbital resonance with the massless body A when it completes exactly p orbits about the primary in the same time that is required for body A to complete q orbits. For convenience, the primary body is subsequently selected to be a planet, body A is defined as a moon associated with the primary planet, and body B represents a spacecraft. In this definition of orbital resonance, p and q are positive integers, and by convention, p is associated with body B, that is, the spacecraft, and q reflects the period of body A, that is, the moon about the planet. For example, a spacecraft in a 1:2 resonance with Europa completes one revolution around Jupiter in the same time that Europa completes two periods. In an orbit-orbit resonance, the spacecraft and the moon possess periods of revolution that are a simple integer ratio. Assume that the spacecraft and the moon possess orbital periods T_p and T_q respectively, such that ratio between periods is,

$$\frac{p}{q} = \frac{n_p}{n_q} = \frac{\frac{1}{T_p}}{\frac{1}{T_q}} = \frac{T_q}{T_p} \tag{3.1}$$

The mean motion n_i corresponding to body i, is a function of the mass of the planet and the semi-major axis of the orbit, i.e.,

$$n_i = \sqrt{\frac{Gm_1}{a_i^3}} \tag{3.2}$$

where Gm_1 is the gravitational parameter of the planet in this two-body model. The orbital period T_i is proportional to the inverse of the mean motion, n_i. The most straightforward approach to generate a planar resonant orbit in the two-body model is by selection of the set of initial conditions at periapsis or apoapsis. In the two-body problem, periapsis is defined as the point along an elliptical trajectory that is closest to the primary gravitational source, and apoapsis is the point of greatest separation from the attracting center. The six-element initial state vector required to compute a resonant orbit has the form $\bar{q}_0 = [x_0\ y_0\ z_0\ \dot{x}_0\ \dot{y}_0\ \dot{z}_0]^T$. For a planar resonant orbit, let $z = \dot{z} = 0$, and thus, $z_0 = \dot{z}_0 = 0$. If the set of initial conditions is selected at an apse location, then $y_0 = 0$, and the initial velocity is entirely in the y-direction, that is, $\dot{x}_0 = 0$. Hence, the initial state reduces to the form $\bar{q}_0 = [x_0\ 0\ 0\ 0\ \dot{y}_0\ 0]^T$, where x_0 and $\dot{y}_0$ are the initial position along the x-axis and the velocity is completely in the y-direction, respectively. The initial state is expressed in terms of inertial coordinates and can be computed from the expressions for the selected orbital elements, that is,

$$a = \left[\mu_{2B}\left(\frac{P}{2\pi}\right)^2\right]^{\frac{1}{3}} \tag{3.3}$$

$$r = \frac{p}{1 + ecos\theta^*} \tag{3.4}$$

$$p = a(1 - e^2) \tag{3.5}$$

$$v = \sqrt{2\mu_{2B}\left(\frac{1}{r} - \frac{1}{2a}\right)} \tag{3.6}$$

where p is the semilatus rectum, v the inertial velocity in the y-direction. The angle θ^* is the true anomaly, that is, the angle that defines the position of the particle along the conic trajectory. At periapsis, $\theta^* = 0°$; at apoapsis $\theta^* = 180°$. In Eq. (3.3), μ_{2B} is the gravitational parameter, defined as $\mu_{2B} = Gm_A$, where m_A is the mass of the primary. To initiate a search for resonant orbits, the orbital eccentricity, e, is arbitrarily selected such that, initially, the spacecraft r_p lies between the two primaries, that is, the planet and the moon. For a resonant orbit, let the period, P,

be equal to the period of the spacecraft, therefore, it is also a function of the resonant ratio p:q and the period of the moon, that is,

$$P = P_{s/c} = \left(\frac{q}{p}\right) P_{moon} \tag{3.7}$$

where $P_{s/c}$ is the period of the spacecraft and P_{moon} is the period of the moon in resonance with the spacecraft. For clarification, both the spacecraft and the moon are orbiting a primary body, i.e., a planet, in a two-body model. Once the initial state is defined, it is possible to compute the resonant trajectory of interest in the inertial reference frame employing the analytical solution available. However, valuable insight is obtained from a view of this resonant trajectory in a rotating frame. The three axes corresponding to a rotating frame in the two-body model are defined such that the planet and its moon remain stationary along the x-axis, the z-axis is parallel to the orbital angular momentum vector, and the y-axis completes the right-handed triad. With this definition of the rotating frame, the initial state can be transformed from inertial to rotating coordinates using the transformation in Eq. (2.50).

To illustrate orbital resonance within the context of a two-body model, consider the 2:3 resonant orbit in Fig. 3.1. This resonant orbit is computed in the two-body Jupiter system, where Europa is temporarily assumed to be massless and orbiting Jupiter in a circular orbit ($e = 0$) with a radius equal to Europa's semi-major axis, $a = 671101.9638$ km. The pericenter of the spacecraft elliptical orbit is selected such that it intersects Europa's orbit when the spacecraft is at periapsis, r_p. This initial state is determined by selecting a value for the eccentricity such that the spacecraft pericenter is the same as Europa's pericenter, that is, $e = 0.236857171631112$. The corresponding initial values for position and velocity are calculated from Eqs. (3.3)-(3.6) using the specified values for a and e. The inertial and rotating views of the 2:3 resonant trajectory in the two-body model are illustrated in Fig. 3.1. Recall that in this p:q resonance, the spacecraft completes two revolutions around Jupiter in the exact same time interval that is required for Europa to complete three revolutions. In the inertial view, Europa's trajectory around Jupiter is plotted in magenta, and the

spacecraft resonant trajectory appears in green. For illustration purposes, Europa is enlarged 5x in the rotating view.

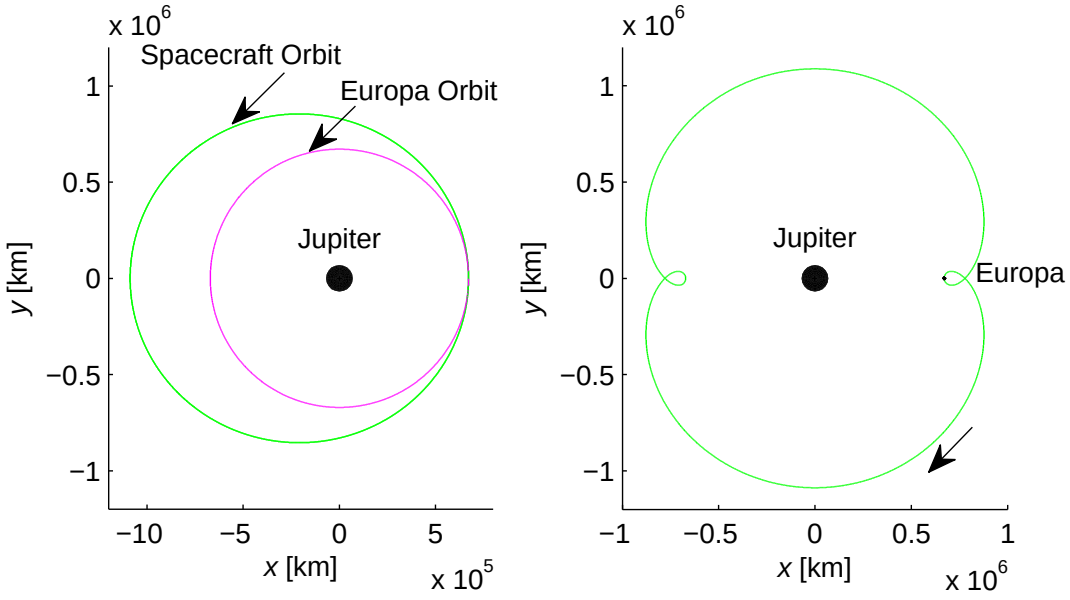

Fig. 3.1. Inertial and Rotating Views of a 2:3 Resonant Orbit around Jupiter - Two-Body Model; Europa Enlarged 5x

Resonant orbits viewed from the perspective of the rotating frame offer valuable insight since this view illustrates the relationship between resonance and the frequency of conjunctions [38], in this case, with Europa. A conjunction occurs when the planet, the moon, and the spacecraft are aligned. Note the relative positions of Jupiter, Europa, and the spacecraft at $t = 0$ in Fig. 3.1. In this example, Europa, the spacecraft, and Jupiter are aligned with the spacecraft at periapsis and between the moon and the planet. This conjunction occurs at periapsis. A special feature of resonant orbits, and one that occurs only in the rotating frame, is the formation of "loops". These loops are apparent in Fig. 3.1 and occur at pericenter and apocenter; hence, the number of loops in the trajectory determines p in a p:q resonance. Resonant orbits are categorized based on the p:q ratio. Exterior resonant orbits have a p:q ratio such that $p<q$, while in an interior resonance the ratio p:q is such that $p>q$.

3.1.3 Resonant Orbits in the CR3BP

The determination of orbital resonance conditions in the CR3BP is even more complex than the analysis in terms of conic orbits. In the restricted three-body model, the p:q resonant ratio is not precisely equal to the ratio of the orbital periods corresponding to the bodies in resonance. In a multi-body problem, with the gravity of two or more bodies incorporated in the model, the time to complete a revolution is not even constant. Instead, for a p:q resonance in the circular restricted three-body problem, the spacecraft completes p orbits around the primary in *approximately* the same time required for the moon to complete q revolutions; thus, the ratio of the orbital periods is not rational, but rather an approximate rational fraction. However, resonant orbits in the CR3BP are still closed, periodic trajectories as observed in the rotating reference frame.

3.1.3.1 Two-Dimensional Resonant Orbits in the CR3BP

Adding a third gravity field to the two-body model adds perturbations to the trajectory, generally resulting in a orbit that is not closed or periodic. Hence, a strategy is required to compute closed, periodic, resonant orbits in the CR3BP. A targeting scheme, similar to one employed to compute planar, periodic orbits in the vicinity of the Lagrange points, can be applied to the computation of periodic resonant orbits in the CR3BP. A reasonably accurate starting estimate for the initial state is generated from the two-body model, but with the state transformed to the rotating reference frame. This starting vector seeds the corrections scheme to target a perpendicular crossing of the x-axis in a non-linear propagation. Recall the form of the initial state vector, that is, $\bar{q}_0 = [x_0 \ 0 \ 0 \ 0 \ \dot{y}_0 \ 0]^T$. After the corrections process is applied and a perpendicular crossing is determined, the end state at the perpendicular crossing is of the final form $\bar{q}_f = [x_f \ 0 \ 0 \ 0 \ \dot{y}_f \ 0]^T$. Two-dimensional resonant orbits, like Lyapunov orbits, are symmetric across the xz-plane; thus, it is sufficient to investigate only half of the resonant path, and then use symmetry to compute the second half of the

orbit. For implementation of the corrections procedure, note that, for most resonant orbits, additional non-perpendicular crossings of the x-axis are likely to occur. The numerical integration process is forced to terminate only at the desired perpendicular crossing, i.e., one half the resonant orbit. There are several ways to construct the algorithm. One method consists of incorporating the period as the stopping condition for the corrections algorithm; that is, if the period of the desired resonant orbit is known, the algorithm can be forced to stop at a time approximately equal to one-half of the period of the resonant orbit. Alternatively, restricting the location of the x-axis crossing is also effective. Of course, if the period and the location of the perpendicular crossing along the x-axis is available, these two methods can be combined to speed the convergence process by reducing the number of iterations. An example of a planar, periodic, resonant orbit with multiple non-perpendicular crossings in the Jupiter-Europa system is plotted in Fig. 3.2. Note that the gravity of both Jupiter and Europa is incorporated in the model. Along this 3:5 resonant trajectory, the spacecraft completes three revolutions around Jupiter in the time required for Europa to complete five revolutions. To illustrate the perturbating effects of the additional gravity field in the CR3BP, the initial guess computed from the two-body model and the corrected initial state in the three-body model for the 3:5 resonant orbit are listed in Table 3.1 and the resonant orbit appears in Fig. 3.2. For comparison, the periods for both trajectories are listed in the table as well. For this particular resonant orbit, adding a third attracting center results in a an orbital period 1.3818 minutes shorter.

Table 3.1
Two-Body Initial Guess and Three-Body Corrected Initial State of a
3:5 Resonant Orbit in the Rotating Frame - Jupiter-Europa System

3:5 resonance	x (km)	y (km)	$\dot{x}$ (km/sec)	$\dot{y}$ (km/sec)	Period (days)
2-Body model	471,691.098	0	0	10.414691	17.760437
3-Body model	471,687.122	0	0	10.415956	17.759477

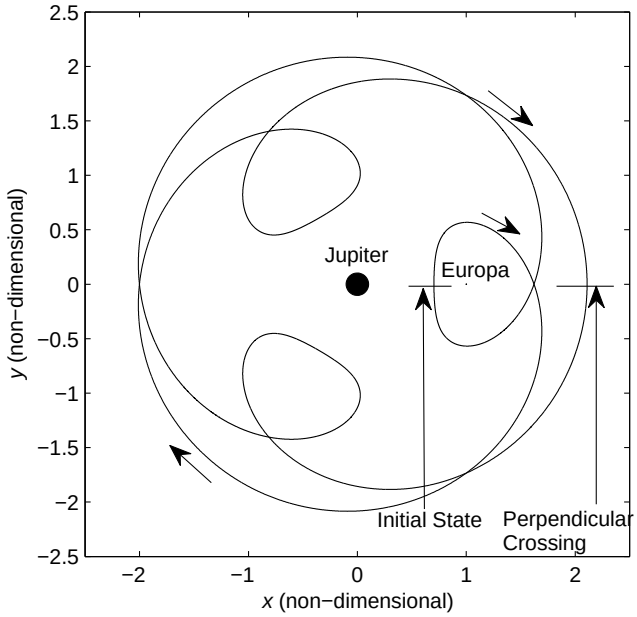

Fig. 3.2. A Periodic 3:5 Resonant Orbit in the Jupiter-Europa System; Plotted in the Rotating Reference Frame

Once a single, periodic, resonant orbit is determined in the CR3BP, it is possible to generate multiple resonant orbits with the same characteristics, that is, a family of p:q resonant orbits, by employing the continuation method in the corrections scheme that is discussed in Section 2.4.1. Members of a representative family of 3:5 resonant orbits appear in Fig. 3.3. The same strategy is employed to generate almost any family of interior and exterior resonant orbits. Families of 5:6 and 5:4 resonant orbits are selected as representative examples of exterior and interior resonant orbits, respectively, and are plotted in Fig. 3.4 and Fig. 3.5.

3.1.3.2 Three-Dimensional Resonant Orbits in the CR3BP

Similar to families of Lyapunov orbits, these families of resonant orbits also include bifurcating orbits to three-dimensional, periodic resonant orbits. These bifurcating orbits can be identified by examining the eigenvalues of the monodromy matrix cor-

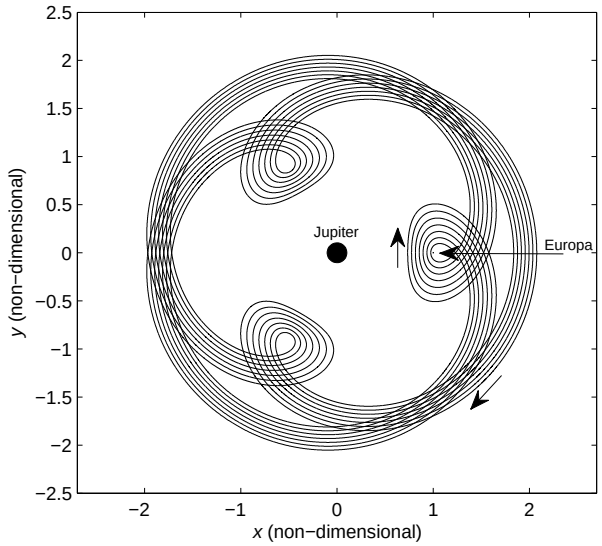

Fig. 3.3. Representative Orbits in a Family of 3:5 Exterior Resonant Orbits in the Jupiter-Europa System

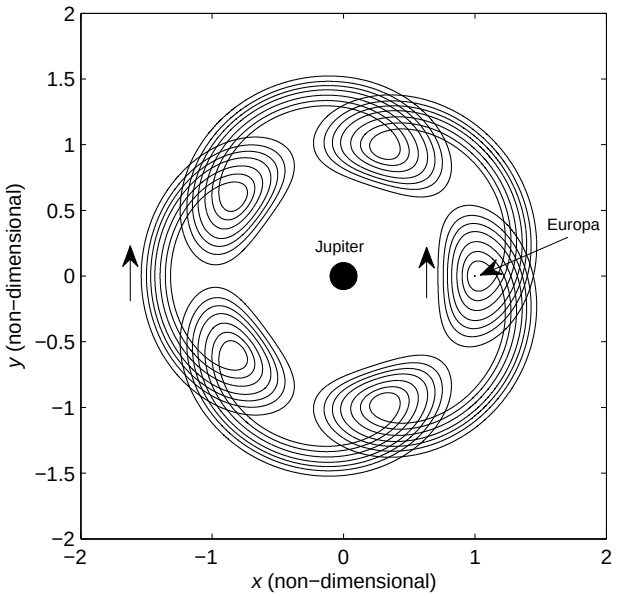

Fig. 3.4. Representative Orbits in a Family of 5:6 Exterior Resonant Orbits in the Jupiter-Europa System

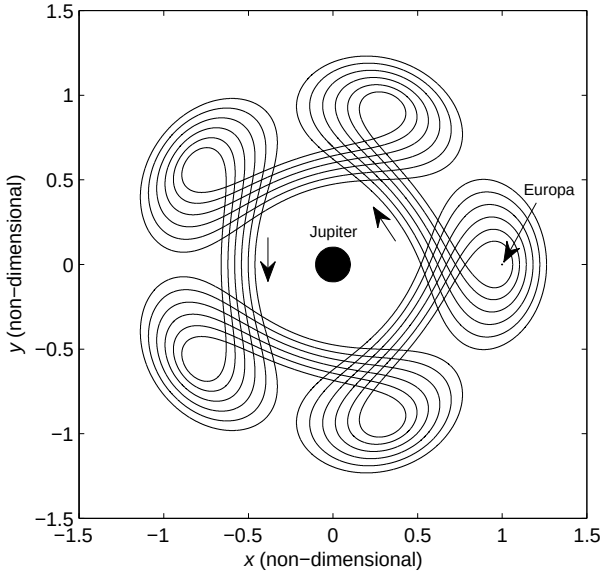

Fig. 3.5. Representative Orbits in a Family of 5:4 Interior Resonant Orbits in the Jupiter-Europa System

responding to each orbit in the family. Recall that the presence of a bifurcating orbit is indicated by an abrupt change in stability, as reflected in the eigenvalues of the monodromy matrix. The stability properties change whenever the eigenvalues depart from or arrive at the unit circle in the complex plane. As an illustrative example, consider the family of planar 3:5 resonant orbits plotted in Fig. 3.3. A stability analysis is completed and the bifurcating orbit is determined; the associated non-zero initial conditions, Jacobi constant (JC), and period are listed in Table 3.2. To illustrate this change in stability, the eigenvalues of the monodromy matrix are represented in the complex plane in Fig. 3.6; Fig. 3.6(a) includes the eigenvalues of a member of the 3:5 resonant orbit family that is closest to the bifurcating orbit and Fig. 3.6(b) includes the eigenvalues of the actual bifurcating orbit. Note that the eigenvalues depart from the unit circle. The actual eigenvalues for both orbits are listed in Table 3.3.

Once the bifurcating orbit is identified, it is possible to target these out-of-plane families by employing an algorithm based on the same scheme used to compute halo orbits from a bifurcating Lyapunov orbit. First, the resonant orbit that bifurcates to

Table 3.2
Initial Conditions of the Bifurcating 3:5 Resonant Orbit Corresponding to the 3:5 Resonant Orbit Family Plotted in Fig. 3.3

x (km)	y (km)	$\dot{x}$ (km/sec)	$\dot{y}$ (km/sec)	JC	Period (days)
638,120.4	0	0	3.180825	2.954818	17.74520

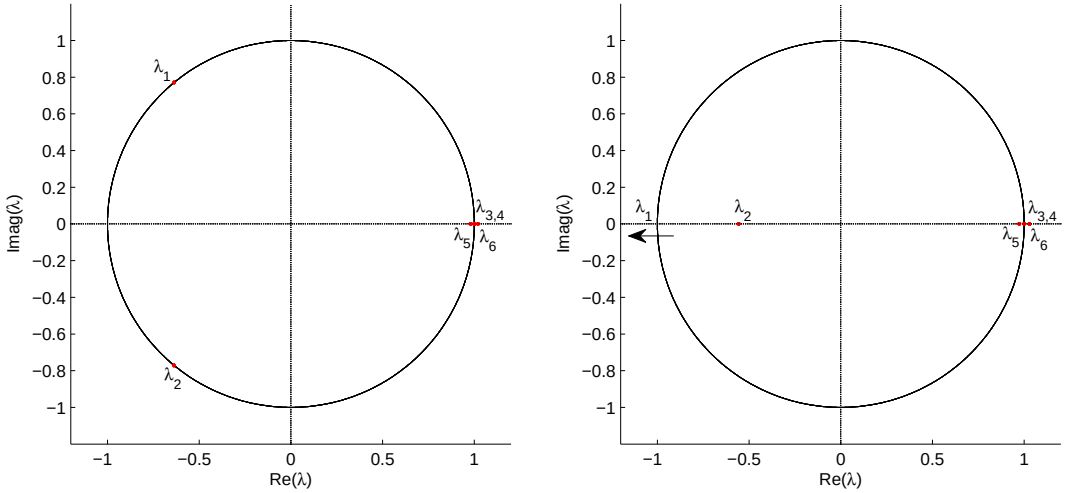

(a) Eigenvalues of a 3:5 Resonant Orbit (b) Eigenvalues of the 3:5 Bifurcating Orbit

Fig. 3.6. Representation of the Eigenvalues of the Monodromy Matrix Corresponding to (a) a 3:5 Resonant Orbit in the Vicinity of the Bifurcating Orbit, and (b) the Bifurcating Orbit Plotted in Fig. 3.3

a different family of orbits is isolated by examining the eigenvalues of the monodromy matrix computed for each orbit in the family, and identifying an abrupt change in the characteristics of these eigenvalues. The bifurcating orbit is then slightly perturbed in the z-direction and the resulting state seeds the corrections scheme to target a three-dimensional resonant orbit. As in the case of planar resonant orbits, additional non-perpendicular crossings may occur along these families of *3*-D resonant orbits. Thus, the corrections algorithm targets a perpendicular crossing. Recall that convergence to a three-dimensional resonant orbit can be accomplished by including the

Table 3.3
Eigenvalues of the Monodromy Matrix Corresponding to the Orbit Closest to the Bifurcating Orbit, and the Bifurcating 3:5 Resonant Orbit

Eigenvalues	Closest 3:5 Orbit	Bifurcating 3:5 Orbit
λ_1	-0.636897 + 0.770948i	-1.798649
λ_2	-0.636897 - 0.770948i	-0.555972
λ_3	1.000000	1.000000
λ_4	1.000000	1.000000
λ_5	0.980301	0.972642
λ_6	1.020094	1.028126

orbital period and the approximate location of the perpendicular crossing along the x-axis to the stopping conditions. Thus, the search is limited to a specific region that contains the appropriate perpendicular crossing. Samples from these families of three-dimensional resonant orbits appear in Figs. 3.7-3.12. Representative members from the family of *3*-D 3:5 resonant orbits that intersect the *2*-D family in Fig. 3.3 are plotted in Fig. 3.7; Fig. 3.9 includes representative members in the family of *3*-D 5:6 resonant orbits bifurcating from the planar family plotted in Fig. 3.4. For completeness, Table 3.4 includes the non-zero initial conditions, values of Jacobi Constant, and orbital periods corresponding to the smallest three-dimensional orbits represented in each family in Figs. 3.7, 3.9, and 3.11. Recall that the zero elements in each set of initial conditions are y and $\dot{x}$, that is, $y = \dot{x} = 0$.

Similar families of three-dimensional resonant orbits are straightforwardly computed for different values of the mass fraction μ. In particular, the same family of *3*-D 3:5 resonant orbits illustrated in Fig.3.7 also exists for a value of $\mu = 0.00023658$, which corresponds to the Saturn-Titan system. Representative members of this family are plotted in Fig. 3.11; Fig. 3.12 includes two-dimensional views of this three-dimensional family of resonant orbits.

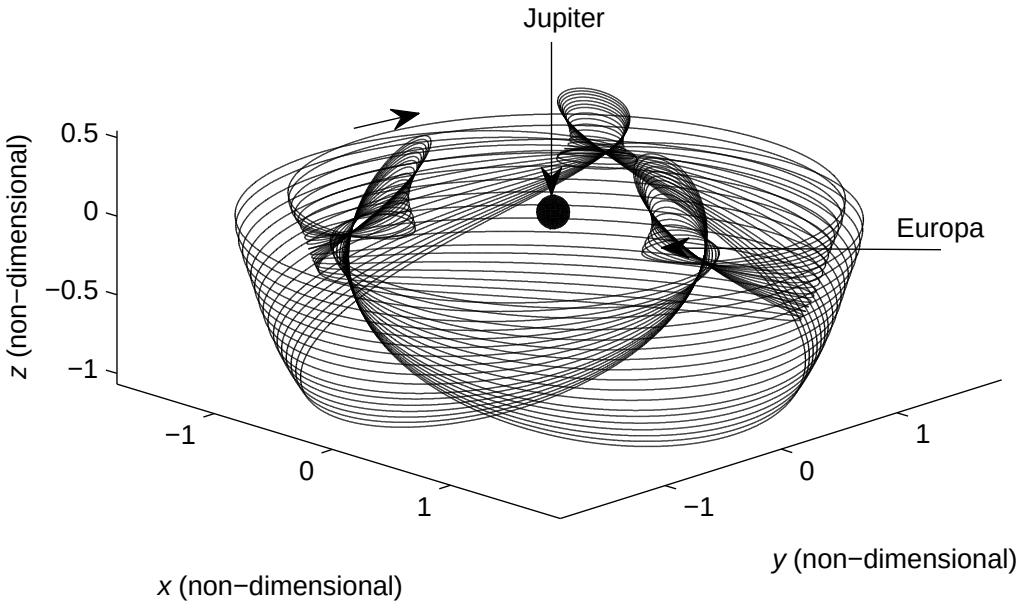

Fig. 3.7. Representative Orbits in a Three-Dimensional Family of 3:5 Resonant Orbits in the Jupiter-Europa System - Rotating Frame

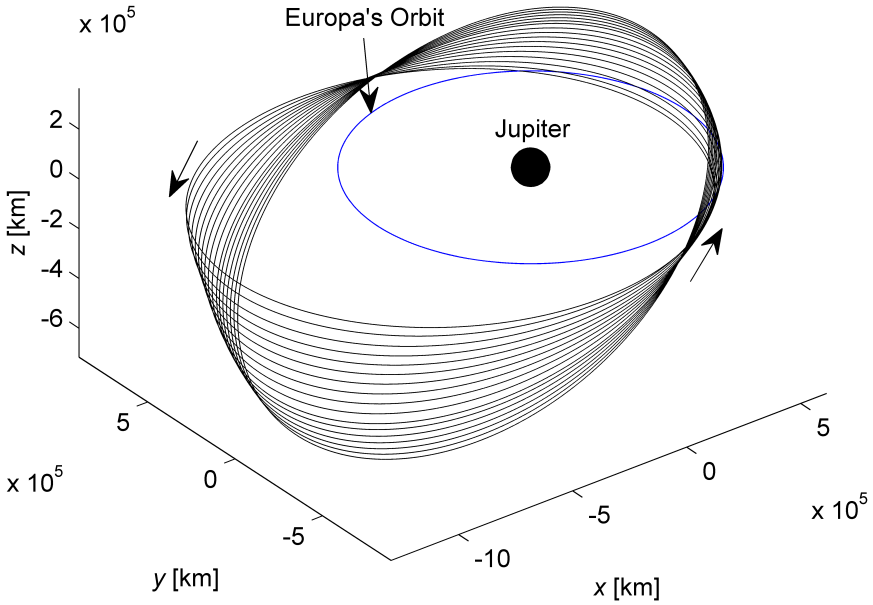

Fig. 3.8. Representative Orbits in a Three-Dimensional Family of 3:5 Resonant Orbits in the Jupiter-Europa System - Inertial Frame

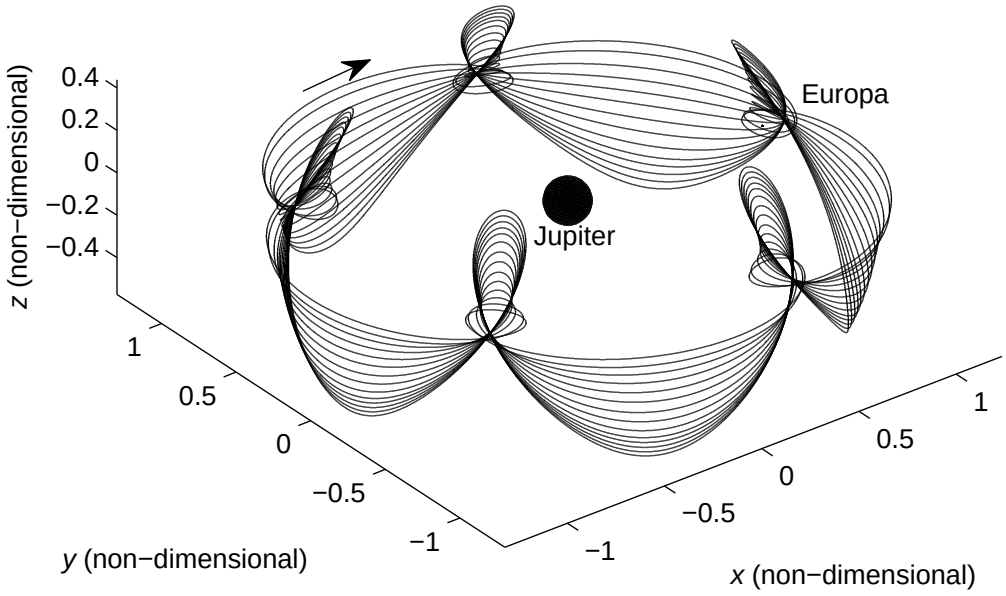

Fig. 3.9. Representative Orbits in a Three-Dimensional Family of 5:6 Resonant Orbits in the Jupiter-Europa System - Rotating Frame

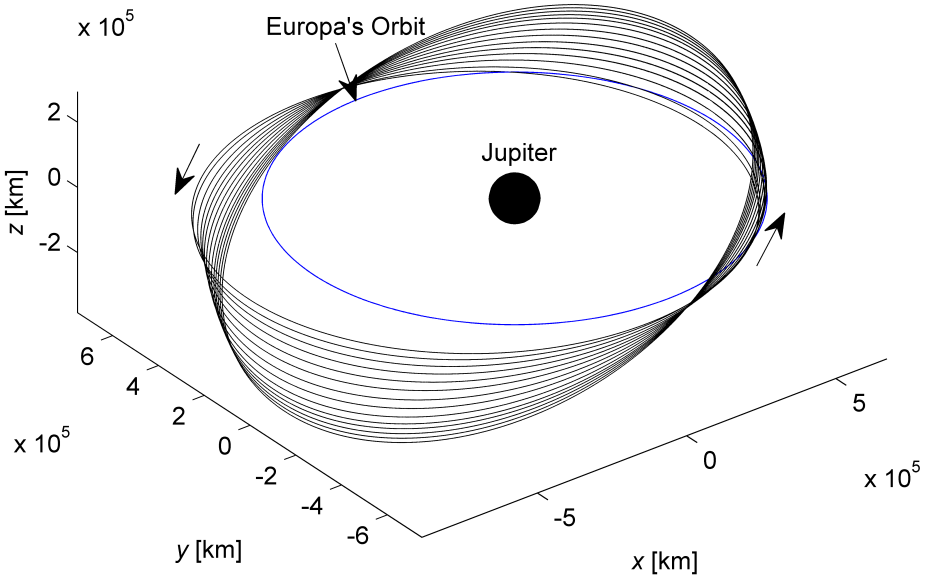

Fig. 3.10. Representative Orbits in a Three-Dimensional Family of 5:6 Resonant Orbits in the Jupiter-Europa System - Inertial Frame

Table 3.4
Non-Zero Initial Conditions and Jacobi Constant Values Corresponding to the Smallest Three-Dimensional p:q Resonant Orbits in Each Family

p:q	system	x (km)	z (km)	$\dot{y}$ (km/sec)	JC	P (days)
3:5	Jupiter-Europa	591,122.22	671.10	5.06348	2.77511	17.7557
3:5	Saturn-Titan	1,103,240.31	137,154.22	1.79388	2.92443	79.5756
5:6	Jupiter-Europa	629,857.41	67.11	2.47808	2.98000	21.2723

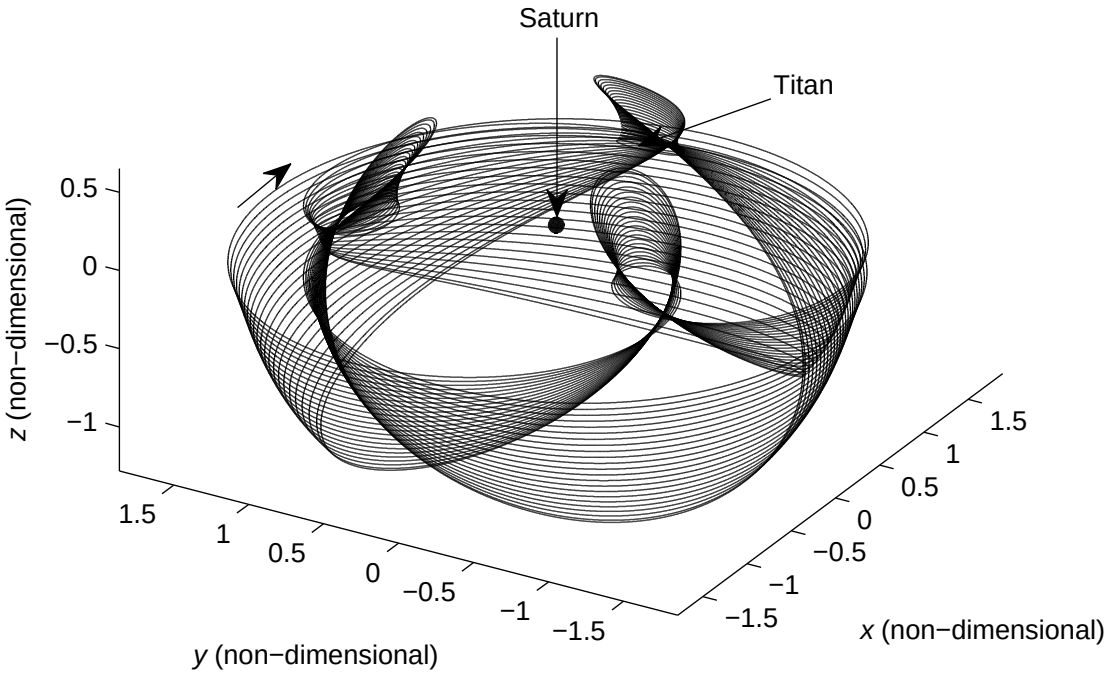

Fig. 3.11. Representative Orbits in a Three-Dimensional Family of 3:5 Resonant Orbits in the Saturn-Titan System - Rotating Frame

3.2 Invariant Manifold Theory

The role of invariant manifolds is significant in building a framework to model the dynamical structure in the CR3BP. Knowledge of any manifold structure improves

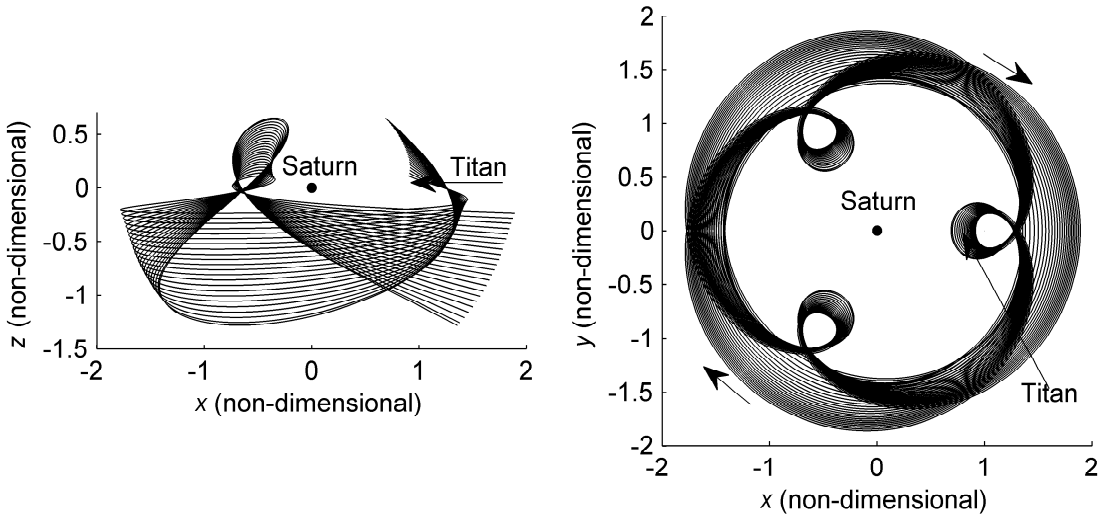

Fig. 3.12. Two-Dimensional Views of the Three-Dimensional Family of 3:5 Resonant Orbits in the Saturn-Titan System - Rotating Frame

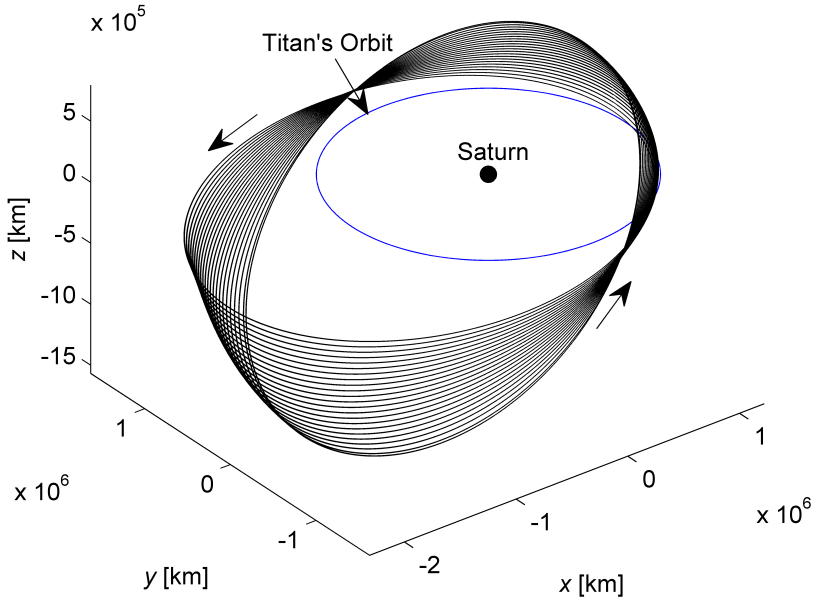

Fig. 3.13. Representative Orbits in a Three-Dimensional Family of 3:5 Resonant Orbits in the Saturn-Titan System - Inertial Frame

the efficiency of trajectory design in this regime. The use of invariant manifolds in the design of transfers between resonant orbits for different values of the mass fraction, μ, is the focus of this effort. Therefore, a general background concerning the phase space near periodic orbits in the CR3BP is key and necessary for the understanding of resonant orbits and their associated manifolds. In addition to this basic theoretical background in invariant manifold theory, a method for the numerical computation of the unstable and stable manifolds is also detailed.

3.2.1 Invariant Manifolds for Fixed Points

The geometrical theory of dynamical systems is based on the phase portrait associated with solutions to a non-linear set of differential equations. In the CR3BP, equilibirum points and periodic solutions are two types of solutions that yield a very interesting structure in terms of the phase space. The geometry of the phase space is investigated by considering these particular solutions to non-linear differential equations and the structure associated with the local flow. The following background information follows directly from the discussion in Parker and Chua [39], Guckenheimer and Holmes [40], and Perko [41] on continuous and discrete time autonomous systems.

Recall the equilibrium solutions, L_i. The phase portrait near these equilibrium points is determined from the variational equations. Recall that the initial conditions near a reference solution, $\bar{x}_{eq}(\tau)$, is represented in terms of a variation $\delta\bar{x}$, that is, $\bar{x}(\tau) = \bar{x}_{eq}(\tau) + \delta\bar{x}(\tau)$. Consider the system of non-linear differential equations,

$$\dot{\bar{x}}(\tau) = \bar{f}(\bar{x}(\tau)) \tag{3.8}$$

This system can be linearized about some reference solution $\bar{x}_{eq}(\tau)$ such that,

$$\delta\dot{\bar{x}}(\tau) = A(\tau)\delta\bar{x}(\tau) \tag{3.9}$$

where $A(\tau) = D\bar{f}(x(\bar{\tau}))$ is the Jacobian matrix comprised of the first partial derivatives of $\bar{f}$ evaluated at the reference solution. If the reference solution is a fixed point

such as $\bar{x}_{eq}(\tau) = \bar{x}_{eq}$, that is, an equilibrium solution of the system in Eq. (3.8), then the Jacobian matrix $A(\tau) = A$ is constant. In such a case, the general solution to Eq. (3.9) is,

$$\delta\bar{x}(\tau) = e^{A(t-t_0)}\delta\bar{x}(\tau_0) \tag{3.10}$$

which can also be expanded and written in the form,

$$\delta\bar{x}(\tau) = \sum_{j=1}^{n} c_j e^{\lambda_j(t-t_0)}\bar{v}_j \tag{3.11}$$

where the coefficients c_j are determined from the initial conditions, and λ_j and $\bar{v}_j$ represent the eigenvalues and eigenvectors associated with the Jacobian matrix A.

The stability of the equilibrium points is determined from the characteristics of the eigenvalues λ_j that are computed from the constant Jacobian matrix. If the real part of the eigenvalue is negative for all λ_j, then sufficiently small perturbations tend to zero as time approaches infinity, and $\bar{x}_{eq}$ is defined as asymptotically stable. If the real part of the eigenvalue is positive for any λ_j, then a perturbation grows with time, and $\bar{x}_{eq}$ is denoted as unstable. If i, j exist such that the real parts of the eigenvalues are both positive and negative, then $\bar{x}_{eq}$ is non-stable. A non-stable equilibrium point is a saddle point, which is consistent with an examination of the collinear points L_1, L_2, and L_3; a stable or unstable equilibirum point with no complex eigenvalues is labeled a node, and an equilibrium point is hyperbolic if all eigenvalues possess non-zero real parts.

For purposes of a stability discussion, the system is 'linear'. Let the Jacobian matrix for the system described by Eq. (3.9) possess n_s eigenvalues with positive real parts, n_u eigenvalues with negative real parts, and n_c eigenvalues with zero real parts. The eigenvectors associated with these eigenvalues are linearly independent, thus, they span $\Re^n$. The n-dimensional space $\Re^n$ is generally represented in terms of three fundamental subspaces: the stable subspace E^s, the unstable subspace E^u, and the center subspace E^c. These are the invariant subspaces associated with the linear variational equations in Eq. (3.9). Subscripts s, u, c reflect the dimension of each subspace such that $n = s + u + c$, or, $n = n_s + n_u + n_c$. A solution initially in a

specific subspace remains in that subspace for all time, leading to the definitions of the local stable and unstable manifolds. Given the equilibrium solution, $\bar{x}_{eq}$, the Stable Manifold Theorem (Guckenheimer and Holmes [40]) states that if all eigenvalues, λ_j, associated with the constant Jacobian matrix A possess non-zero real parts, then $\bar{x}_{eq}$ is a hyperbolic equilibrium point, and does not possess a center manifold. Local stable and unstable invariant manifolds, W^s_{loc} and W^u_{loc}, are related to the invariant subspaces E^s and E^u associated with the linear system. The term "invariant" indicates that a point on the manifold will remain on the manifold as time progresses [40]:

Theorem 3.2.1 (Stable Manifold Theorem) *Suppose $\dot{\bar{x}}(\tau) = \bar{f}(\bar{x}(\tau))$ possesses a hyperbolic equilibrium point $\bar{x}_{eq}$. Then there exist local stable and unstable manifolds $W^s_{loc}(\bar{x}_{eq})$, $W^u_{loc}(\bar{x}_{eq})$, of the same dimension n_s, n_u, as those of the eigenspaces E^s, E^u, of the linearized system in Eq. (3.9), and tangent to E^s and E^u at $\bar{x}_{eq}$. These local stable and unstable manifolds, $W^s_{loc}(\bar{x}_{eq})$, $W^u_{loc}(\bar{x}_{eq})$, are as smooth as function $\bar{f}$.*

Let $\bar{x}_{eq}$ be the equilibrium point of a two-dimensional first-order system with eigenvalues λ_s and λ_u, as well as eigenvectors $\bar{v}_s$ and $\bar{v}_u$, that span the subspaces E^s and E^u. Hence, $\bar{v}_s$ and $\bar{v}_u$ form a basis in $\Re^2$. The diagram in Fig. 3.14 illustrates the flow to and from $\bar{x}_{eq}$, which is governed by the corresponding eigenstructure, that is, the figure is a representation of a planar projection of the stable and unstable manifolds at $\bar{x}_{eq}$. For this particular example, the stable and unstable eigenvector subspaces are each comprised of one eigenvector, that is, $E_s = \bar{v}_s$, and $E_u = \bar{v}_u$. The local branch of the invariant manifold $W^{s^+}_{loc}$ is represented by $\bar{v}_s$, and $W^{s^-}_{loc}$ corresponds to $-\bar{v}_s$. Similarly, $W^{u^+}_{loc}$ is defined by $\bar{v}_u$, and $W^{u^-}_{loc}$ corresponds to $-\bar{v}_u$. In other words, the local stable and unstable manifolds are parallel to the stable and unstable eiegnvectors. The local invariant manifolds W^s_{loc} and W^u_{loc} possess nonlinear global analogs W^s and W^u that can be approximated by propagating the flow backwards in time along W^s_{loc} and forward in time along W^u_{loc}, respectively.

If $\bar{x}_{eq}$ is a non-hyperbolic equilibrium point, that is, n_s, n_u, and n_c are <u>all</u> non-zero, the structure of the local flow is governed by the Center Manifold Theorem for Flows, as stated by Guckenheimer and Holmes [40]:

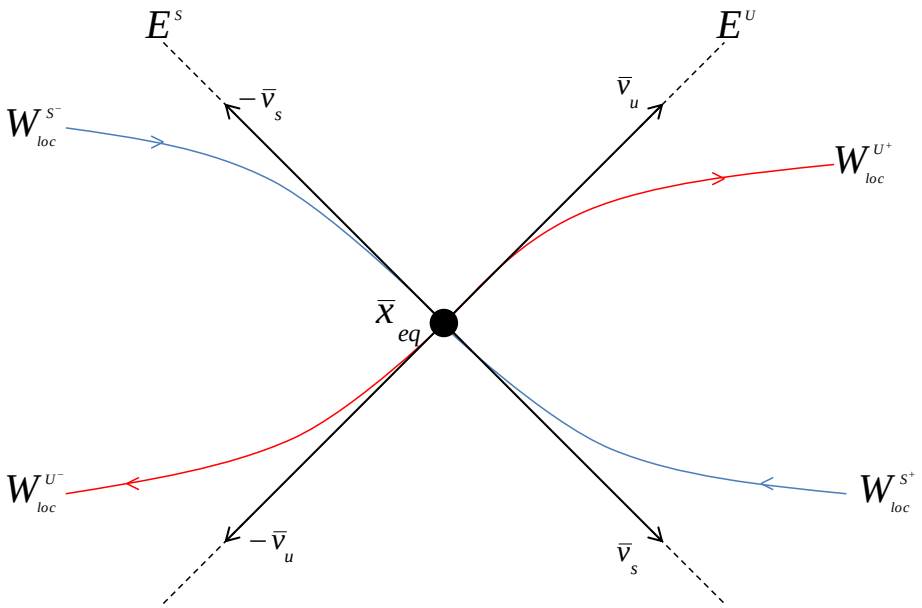

Fig. 3.14. Stable and Unstable Manifolds of an Equilibrium Point

Theorem 3.2.2 (Center Manifold Theorem for Flows) *Let $\bar{f}$ be a vector field on $\Re^n$ vanishing at the origin $\bar{f}(\bar{x}_{eq}) = \bar{0}$ and $A = D\bar{f}(\bar{x}_{eq})$. The spectrum of A is divided into three parts n_s,n_c, and n_u with*

$$Re[\lambda] < 0; \lambda \in n_s \tag{3.12}$$

$$Re[\lambda] = 0; \lambda \in n_c \tag{3.13}$$

$$Re[\lambda] > 0; \lambda \in n_u \tag{3.14}$$

Let the generalized eigenspaces be E^s, E^c, and E^u, respectively. Then, there exist stable and unstable invariant manifolds W^u and W^s tangent to the E^u and E^s at $\bar{x}_{eq}$, and a center manifold at W^c tangent to the center subspace E^c at $\bar{x}_{eq}$. The manifolds W^u, W^s, and W^c are all invariant for the flow $\bar{f}$. The stable and unstable manifolds are unique, but W^c need not be.

The existence of a center manifold implies that the structure of the flow near the equilibrium point, possessing at least one zero eigenvalue, is more diverse than an

equilibrium point with no center subspace. The solutions initially in the center manifold neither grow nor decay over time, relative to $\bar{x}_{eq}$. Periodic orbits such as Lyapunov orbits as well as quasi-periodic trajectories, for example, near-vertical, out-of-plane orbits, are examples of types of motion that might exist in the center subspace near the equilibrium point, $\bar{x}_{eq}$.

Manifold structures have been studied by many researchers, and their application to trajectory design in multi-body regimes has been demonstrated. In fact, transfers between different three-body systems are a new focus for potential mission scenarios [42], in which the exploitation of the invariant manifolds associated with these orbits plays a crucial role.

3.2.2 Invariant Manifolds for Periodic Orbits

Calculating stable, unstable, and possibly center manifolds associated with periodic orbits is more complex than the underlying structure for equilibrium points. Although a periodic orbit is a solution of the non-linear differential equations in Eqs. (3.8), the associated variational equation in Eq. (3.9) yields a Jacobian matrix that is not constant. However, it is possible to discretize the continuous time system to form a map. Various types of maps are useful, but Poincaré maps are most applicable for interpretation of the phase space in this problem. Poincaré maps reduce the dimensionality of the problem and are a valuable tool in the study of a periodic orbit. The concept for construction of a Poincaré map representing a low-dimensional system is illustrated in Figure 3.15. To construct this map, a surface Σ that is transverse to the flow, is defined at a particular point along the flow. In Fig. 3.15, a periodic orbit, defined in terms of the state $\bar{x}$ and labeled Γ, is initiated in the plane Σ and returns to intersect the plane after exactly one period. A truly periodic orbit returns to exactly the same point on the plane after each revolution. Such a point is denoted a 'fixed point', labeled in the map as $\bar{x}^*$. Then, for any point $\bar{x} \in \Sigma$ sufficiently close to the fixed point, $\bar{x}^*$, a propagation of the differential equation in Eq.(3.8) through $\bar{x}$,

intersects the plane Σ again at the first return point $P(\bar{x})$, generally near the original fixed point.

Because Poincaré maps preserve most of the properties of periodic and quasi-periodic trajectories from the original system, they are also used as a powerful tool for stability analysis. The stability of a periodic orbit from the original system is closely related to the stability of the fixed point of the associated Poincaré map. Thus, Poincaré maps offer evidence of stability and manifold representations. Consider the diagrams in Fig. 3.16. A numerical simulation from an initial state $\bar{x}$, close to the fixed point $\bar{x}^*$, is propagated to the next crossing of the plane Σ. The first return to the map is labeled $P_1(\bar{x})$, and subsequent returns are labeled $P_2(\bar{x})$, $P_3(\bar{x})$, continuing to the last return, $P_n(\bar{x})$. If subsequent returns to the map diverge from the original fixed point, $\bar{x}^*$, then, the orbit is defined as unstable (Fig. 3.16(b)); if the recurring crossings of the map approach the original point, then, the orbit is considered stable (Fig. 3.16(a)). Finally, as illustrated in Fig. 3.16(c), if there is no pattern that is detectable for subsequent returns to the map, i.e., no departure or approach to $\bar{x}^*$ in time, then the orbit is labeled chaotic. The dots illustrated in Figs. 3.16(a)- 3.16(b) represent the stable and unstable manifolds of the fixed point $\bar{x}^*$.

The fixed points along a periodic orbit are used to compute the corresponding stable and unstable manifolds. The phase space in the vicinity of different fixed points is examined by placing the surface Σ transverse to the flow at different points along the periodic orbit. Each of these points, then, serves as a fixed point for the computation of stable and unstable manifolds. Each of the fixed points is an (*n-1*)-dimensional representation of the periodic orbit in $\Re^n$. Therefore, the stable, unstable, and center subspaces possess the dimensions of n_s, n_u, and n_c. That is, the stable manifold associated with the fixed point, $W^s(\bar{x}^*)$, has dimension n_s, and the unstable manifold associated with the fixed point, $W^u(\bar{x}^*)$, has dimension n_u. The dimension of the unstable and stable manifolds of a periodic orbit is stated in the Stable Manifold Theorem for Periodic Orbits [41]:

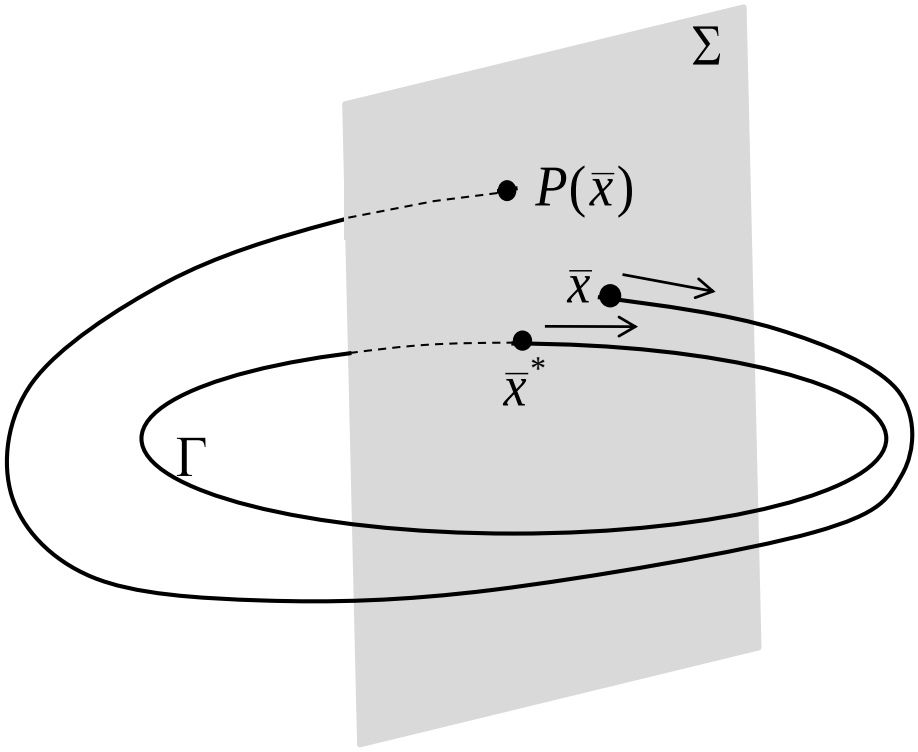

Fig. 3.15. The Poincaré Map

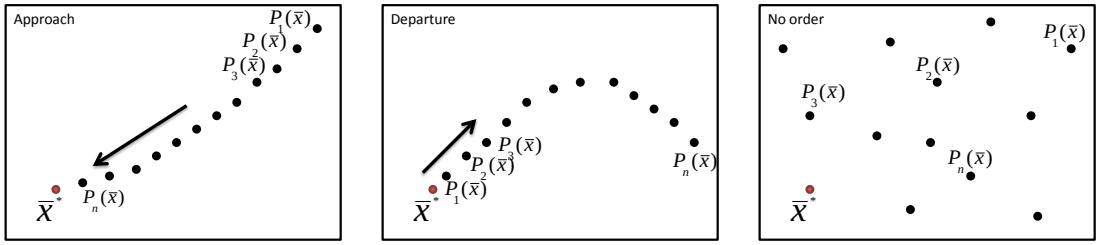

(a) Stable (b) Unstable (c) Chaos

Fig. 3.16. Illustration of Subsequent Returns to a Poincaré Map

Theorem 3.2.3 (Stable Manifold Theorem for Periodic Orbits) *Let an open subset of $\Re^n$ contain a periodic orbit $\Gamma : \bar{x} = \gamma(\tau)$ of period T. Let ϕ_t be the flow and $\gamma(\tau) = \phi_\tau(\bar{x}^*)$. If k characteristic exponents of $\gamma(\tau)$ have a negative real part where*

$0 \leq k \leq n-1$ and $n-k-1$ of them have a positive real part, then there is a $\delta > 0$ such that the stable manifold of Γ,

$$S(\Gamma) = \bar{x} \in N_\delta(\Gamma) | d(\phi_\tau(\bar{x}), \Gamma) \to 0 \text{ as } \tau \to \infty \text{ and } \phi_\tau(\bar{x}) \in N_\delta(\Gamma) \text{ for all } \tau \geq 0$$

is a (k+1)-dimensional, differentiable manifold which is positively invariant under the flow ϕ_τ, and the unstable manifold Γ,

$$U(\Gamma) = \bar{x} \in N_\delta(\Gamma) | d(\phi_\tau(\bar{x}), \Gamma) \to 0 \text{ as } \tau \to -\infty \text{ and } \phi_\tau(\bar{x}) \in N_\delta(\Gamma) \text{ for all } \tau \leq 0$$

is an (n-k)-dimensional, differentiable manifold which is negatively invariant under the flow ϕ_τ. Furthermore, the stable and unstable manifolds of Γ intersect transversally in Γ.

The stable manifold associated with the periodic orbit Γ, that is, $W^s(\Gamma)$, possesses a dimension $n_s + 1$, and the unstable manifold associated with the periodic orbit, i.e., $W^u(\Gamma)$, has dimension $n_u + 1$. Hence, the dimensions of $W^s(\Gamma)$ and $W^u(\Gamma)$ are always one degree higher than E^s and E^u, respectively.

Recall the monodromy matrix, $\Phi(\tau_0 + T, \tau_0)$, first introduced in connection with orbital stability (Section 2.4.3), and Lyapunov's Theorem 2.4.1. For stable and unstable manifolds of a periodic orbit to exist, the monodromy matrix must possess at least one stable and one unstable eigenvalue. However, not all the members in a given family of periodic orbits in the CR3BP possess a stable and unstable eigenvalue. Therefore, it is convenient to develop a method to identify which members in the family do possess stable and unstable eigenvalues, and thus, stable and unstable manifolds. A stability index, ν, associated with each member in a family of periodic orbits is defined such that [16],

$$\nu = \frac{1}{2}(|\lambda_s| + |\lambda_u|) \tag{3.15}$$

In Eq. (3.15), λ_s and λ_u are a real-valued, reciprocal pair of eigenvalues, that is, $\lambda_s = \frac{1}{\lambda_u}$. If the stability index is less than or equal to one, that is, $|\nu| \leq 1$, then, the periodic orbit is considered to be marginally stable, in which case the corresponding

eigenvalues do not yield stable and unstable invariant manifolds. For application purposes, the periodic orbits possessing this type of stability index do not allow for transfers shadowing invariant manifolds to and from the orbit, and, thus, are not of interest in this investigation. Similarly, if $|\nu| \geq 1$, the periodic orbit includes an eigenvalue with magnitude greater than one, and its associated stable and unstable invariant manifolds can be computed [16]. Moreover, the size of the stability index determines how fast the invariant manifolds approach or depart the orbit [16] [43], that is, the larger the size of ν, the faster the manifolds approach/depart the orbit.

3.2.3 Numerical Computation of Invariant Manifolds

Once the periodic orbits and their associated invariant manifolds are identified, the search for potential transfers to and from these orbits in the CR3BP requires the computation of the actual unstable and stable manifolds. The invariant manifolds corresponding to a periodic orbit can be computed by using the eigenvector corresponding to an eigenvalue greater than one in the direction of the local unstable manifold, and the eigenvector corresponding to an eigenvalue less than one in the direction of the local stable manifold. That is, $W_{loc}^{u^+}$ departs the fixed point, $\bar{x}^*$, along the positive direction of $\bar{v}_u$, and $W_{loc}^{u^-}$ departs $\bar{x}^*$ along the negative direction consistent with $\bar{v}_u$. Similarly, $W_{loc}^{s^+}$ approaches the fixed point on the periodic orbit along $+\bar{v}_s$, and $W_{loc}^{s^-}$ approaches the fixed point from the direction of $-\bar{v}_s$. As illustrated in Fig. 3.16, the dots on the surface of section corresponding to the unstable manifolds will diverge from the fixed point as $t \to \infty$, and the returns associated with the stable manifolds will approach the fixed point on the orbit.

The computation of the invariant manifolds requires the propagation of an initial state close to the fixed point in the direction of the desired eigenvector. The algorithm to compute these trajectories is defined as follows: $\bar{x}_{u^+}$ is defined as a point on the local unstable manifold and along the positive direction, $W_{loc}^{u^+}$. Then, integrating forward and backward from point $\bar{x}_{u^+}$ yields W^{u^+}. Calculating a half manifold involves

locating a point on $W_{loc}^{u^+}$, and integrating from this point. To locate a point locally near $\bar{x}^*$, $W_{loc}^{u^+}$ is approximated to first order by the unstable eigenvector $\bar{v}_u$, i.e., by choosing a point close to $\bar{x}^*$ that lies on $\bar{v}_u$, that is,

$$\bar{x}_{u^\pm} = \bar{x}^* \pm l\bar{v}_u \tag{3.16}$$

In Eq. (3.16), l is the offset in the direction of the unstable eigenvector, and its value is of critical importance. If l is too large, the computed value for $\bar{x}_{u^\pm}$ is not a good approximation; if l is too small, the trajectory spends too long near the fixed point and the integration error accumulates with little progress along the path. There are various ways of selecting the appropriate value of l. One option that has proven useful for conceptual insight is to define the components of the unstable eigenvector, $\bar{v}_u = [x_u \; y_u \; z_u \; \dot{x}_u \; \dot{y}_u \; \dot{z}_u]^T$, and define $\bar{v}^{W_u}$ such that,

$$\bar{v}^{W_u} = \frac{\bar{v}_u}{[x_u^2 + y_u^2 + z_u^2]^{\frac{1}{2}}} \tag{3.17}$$

$$\bar{x}_{u^\pm} = \bar{x}^* \pm d \cdot \bar{v}^{W_u} \tag{3.18}$$

In Eq. (3.18), the value d, or the attenuation factor, is selected by interpreting it as a distance relative to the fixed point. Similarly, the positive and negative branches of the local stable manifold can be computed in a similar way by defining the components of the stable eigenvector, $\bar{v}_s = [x_s \; y_s \; z_s \; \dot{x}_s \; \dot{y}_s \; \dot{z}_s]^T$, and defining $\bar{v}^{W_s}$ such that,

$$\bar{v}^{W_s} = \frac{\bar{v}_s}{[x_s^2 + y_s^2 + z_s^2]^{\frac{1}{2}}} \tag{3.19}$$

$$\bar{x}_{s^\pm} = \bar{x}^* \pm d \cdot \bar{v}^{W_s} \tag{3.20}$$

where the symbol $\pm$ represents $\bar{x}_{s^+}$ for the half-manifold in the positive direction along the stable eigenvector and $\bar{x}_{s^-}$ for the half-manifold associated with a direction opposite to the stable eigenvector, that is, $-\bar{v}_s$. As a representative example, the global invariant manifolds corresponding to the smallest Lyapunov orbit in the vicinity of L_1 included in Fig. 2.14 are computed and plotted in Figs. 3.17-3.20. Recall that the initial conditions corresponding to this L_1 Lyapunov orbit are listed in Table 2.2.

The magenta trajectories correspond to the unstable manifolds, and the blue trajectories reflect the stable manifolds. The global invariant manifolds associated with a single fixed point along the L_1 are illustrated in Fig. 3.17 and Fig. 3.18, respectively. However, to better indentify the manifold structure, it is desirable to compute the trajectories from multiple fixed points along the orbit. Note that the eigenvalues and eigenvectors are independent of the number of fixed points selected, and whether these points are evenly spaced in time or position. For illustration purposes, a total of 40 (evenly-spaced in time) fixed points along the periodic orbit are represented in Fig. 3.19 and Fig. 3.20. An offset value of 40 km is a reasonable choice for this periodic orbit in the Earth-Moon system, and the propagation time to construct both the stable and the unstable manifolds is the same and equal to $\tau = 5$ non-dimensional time units, equivalent to 21.7114 days.

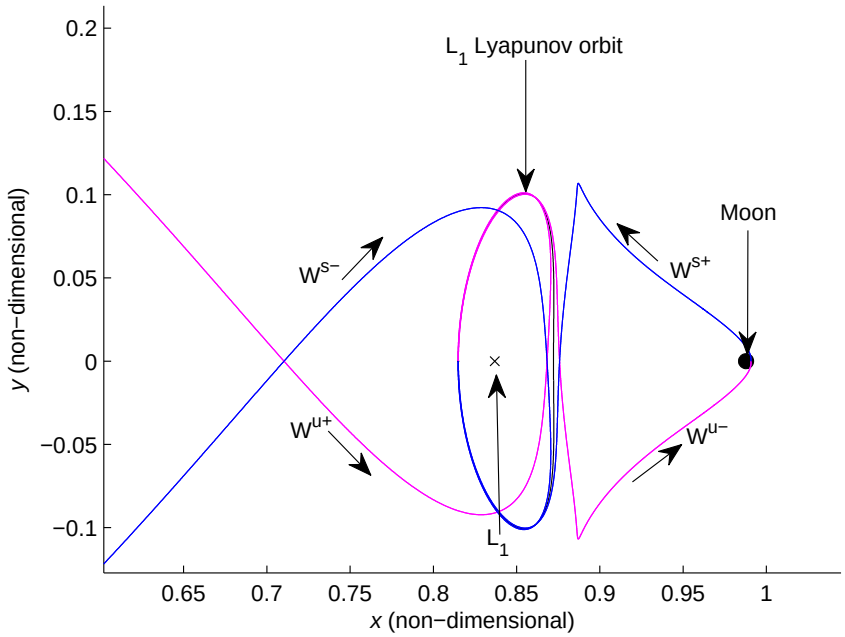

Fig. 3.17. In the Vicinity of L_1, Stable and Unstable Manifolds of a Fixed Point along the Smallest Lyapunov Orbit from Fig. 2.14 (Zoomed View)

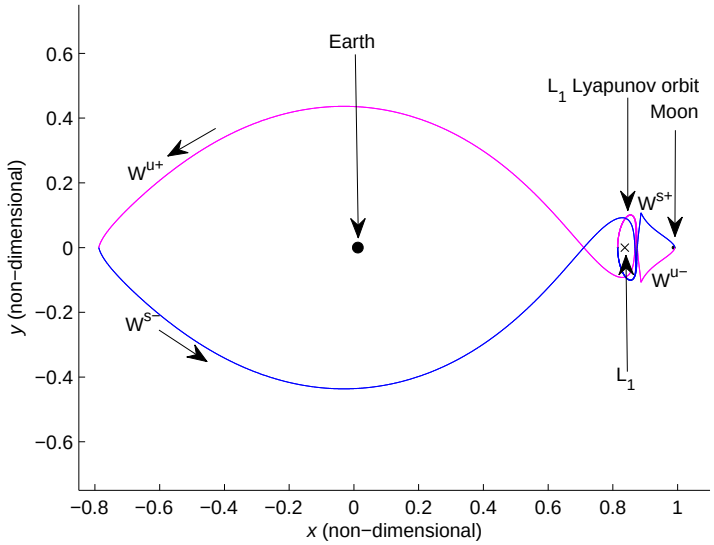

Fig. 3.18. In the Vicinity of L_1, Stable and Unstable Manifolds of a Fixed Point along the Smallest Lyapunov Orbit from Fig. 2.14

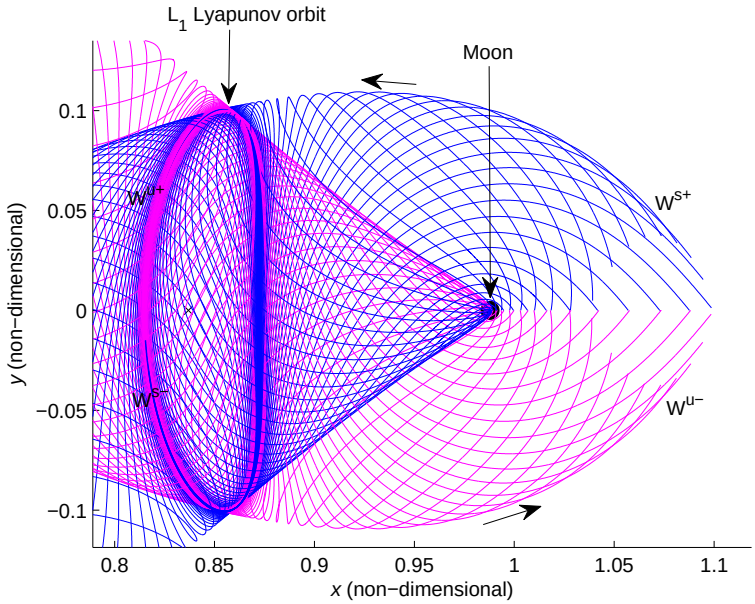

Fig. 3.19. In the Vicinity of L_1, Stable and Unstable Manifolds Corresponding to the Smallest Lyapunov Orbit from Fig. 2.14 (Zoomed View)

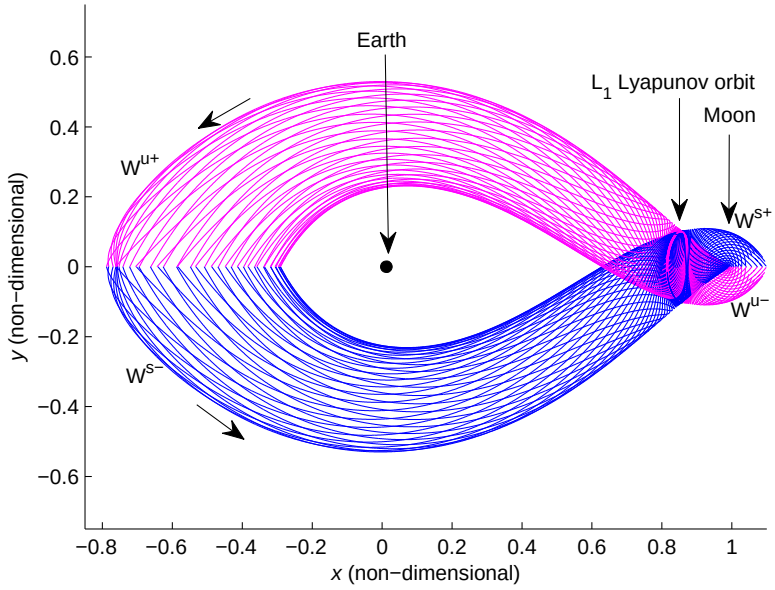

Fig. 3.20. In the Vicinity of L_1, Stable and Unstable Manifolds Corresponding to the Smallest Lyapunov Orbit from Fig. 2.14

3.3 Poincaré Maps

In general, maps are used to describe the time evolution of a vector at discrete intervals. The use of very simple maps allows the representation of the properties of generic dynamical systems that are described by the differential equations. Maps have been used extensively in the last few decades, especially to add insight and expose dynamical structure in complex systems. Due to Henri Poincaré (1899), many systems of differential equations can be represented in terms of maps by reducing the study of a continuous time system to the study of an associated discrete time system. Poincaré first utilized this concept in his studies of the CR3BP; now, virtually any discrete time system that is associated with a set of ordinary differential equations (ODEs) is labeled a "Poincaré map". This technique offers three main advantages: reduction of dimension, global dynamics, and conceptual clarity. The construction of a Poincaré map eliminates at least one variable in the problem, resulting in the analysis of a lower-dimensional system. In lower-dimensional problems, numerically

computed Poincaré maps deliver an insightful and, sometimes, dramatic display of the global dynamics of a system. In fact, for this application, Poincaré sections can highlight the existence of periodic and quasi-periodic orbits [5].

The computation of a Poincaré map for an autonomous higher-dimensional system in $\Re^n$ requires the use of a hyperplane or surface of section, labeled as Σ in $\Re^{n-1}$ which is placed transverse to the flow, as illustrated in Fig. 3.15. A trajectory intersecting the hyperplane is integrated until it intersects the hyperplane once again. As previously noted, the mapping is from one intersection to the next, and so on. For the planar CR3BP in $\Re^4$, the surface of section, or hyperplane Σ, is typically specified by fixing one of the coordinates, usually $y = 0$, producing a surface in $\Re^3$. The three-dimensional surface is projected onto a plane by specification of another parameter. For example, to generate a two-dimensional Poincaré section in the CR3BP, a value for the Jacobi constant can be specified and a grid of initial conditions for x and $\dot{x}$ are selected and integrated forward in time. The grid represents a range of initial conditions originally in the hyperplane, generating many trajectories. The intersections of each trajectory with the surface of section create the Poincaré map. With C, x and $\dot{x}$ initially defined, as well as the hyperplane $y = 0$, the corresponding initial values for $\dot{y}$ can be calculated from the expression for the Jacobi constant in Eq. (2.37), that is,

$$\dot{y} = \sqrt{x^2 + y^2 + \frac{2(1-\mu)}{d} + \frac{2\mu}{r} - \dot{x}^2 - C} \tag{3.21}$$

where d and r are calculated from Eqs. (2.28)-(2.29). Alternatively, an initial range of values for $\dot{y}$ can be defined and the corresponding values for $\dot{x}$ can be calculated from Eq. (2.37). In a Poincaré map, the points defined by the mapping are then plotted. A variety of quantities can be computed and displayed at each iteration of the map. The quantities used to plot the intersections in this investigation are x and $\dot{x}$, although other authors consider quantities such as Delaunay variables, as well as a wide range of other dynamical quantities [5].

As an introductory example to explore the information available in Poincaré sections, consider the Hénon map in Fig. 3.21. The original plots and a more extended

discussion on surfaces of section is offered by Hénon [44]. Hénon produced maps in the 1960's for application to the restricted three-body problem. For relatively high values of the Jacobi constant, the orbits possess Hill stability and, if C is sufficiently high, the perturbations are weak and most orbits are periodic or quasi-periodic. An orbit is Hill stable when the Jacobi constant is larger than the value of Jacobi constant at the equilibrium point L_2, that is, the gateways are closed. In contrast, if $C < C_{L_i}$, the gateway and consequently the zero velocity curve is open and escape is possible [45]. The section in Fig. 3.21 is a section constructed in the planar CR3BP for $\mu = 0.5$. In this system, the mass of the larger primary is the same as the mass of the smaller primary, that is, $m_1 = m_2$. This μ value might represent a binary star system consisting of two stars orbiting around their center of mass. The section is defined such that $C = 4.5$, $y = 0$ and $\dot{y} > 0$. A range of values for x_0 and $\dot{x}_0$ are selected and sufficient returns to the hyperplane are used to yield curves that indicate quasi-periodic orbits. Recall that the corresponding initial values for $\dot{y}_0$ are calculated from the equation for the Jacobi constant. There are two main structures that are easily identified from the map; "chain of islands" structures, and "dusty" or chaotic regions, where the plotted points do not appear to form any specific pattern. The chain of islands structure is a very common structure in this type of map. The center of each island contains a point that intersects the surface of section repeatedly a finite number of times before repeating. These crossings correspond to stable, periodic trajectories. Note that, because only the negative side of the map is considered, that is, $x < 0$, the map is labeled a 'one-sided' map.

Each crossing that forms a chain of islands corresponds to a single quasi-periodic trajectory. To further illustrate these concepts, the crossings corresponding to two different quasi-periodic orbits are plotted in green and blue, respectively, in the map in Fig. 3.22. The actual quasi-periodic trajectories that correspond to the orbits in the section appear in Fig. 3.23. The crossings plotted in green in Fig. 3.22 correspond to the quasi-periodic orbit represented in green in Fig. 3.23; likewise, the crossings plotted in blue in Fig. 3.22 correspond to the quasi-periodic orbit that appears in

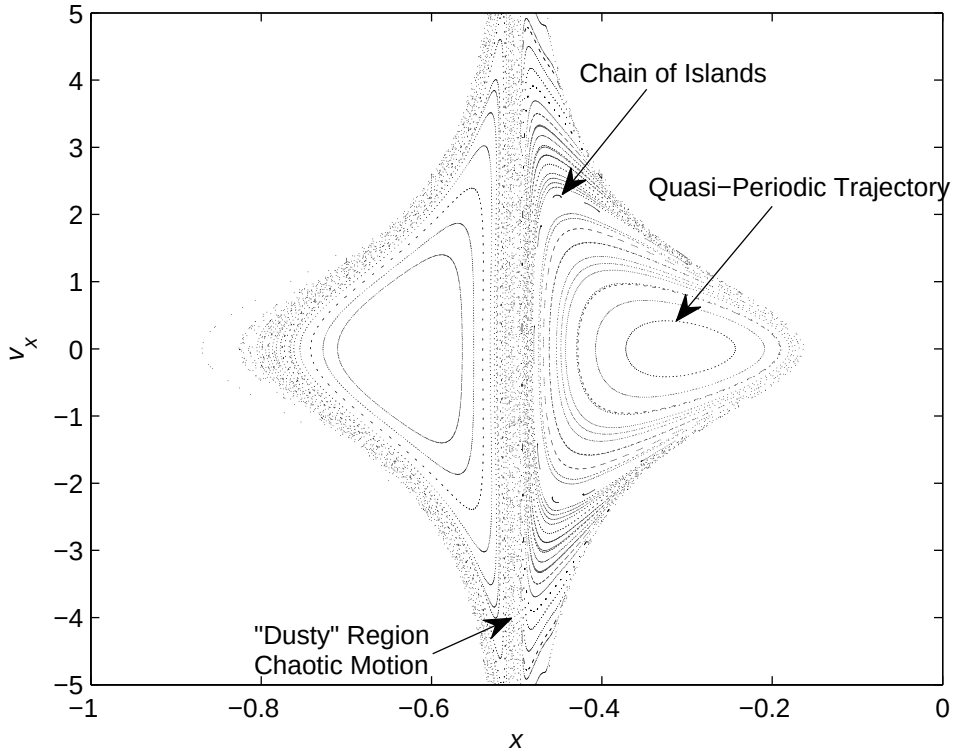

Fig. 3.21. Surface of Section for $C = 4.5$, $\mu = 0.5$

blue in Fig. 3.23. The center crossing plotted in magenta in Fig. 3.22 is the center of one of the chain of islands; this intersection corresponds to the periodic orbit that appears in Fig. 3.24. Recall that this trajectory appears as a single point in the map, and each stable periodic orbit is surrounded by many chains of islands corresponding to quasi-periodic orbits.

The other phenomena that occurs between curves and chains of islands is the formation of "dusty" regions or zones of chaos, where continuity is broken and the regions between curves are filled with unordered crossings. These chaotic zones are not easily apparent in Fig. 3.21 since the perturbations are quite small. The bigger the perturbations, the more dense these regions. For a Jacobi constant value of 3.5, perturbations are large and chaotic motion predominates over structured regions. At this energy level, the points in the chaotic regions do not fill a curve or create a

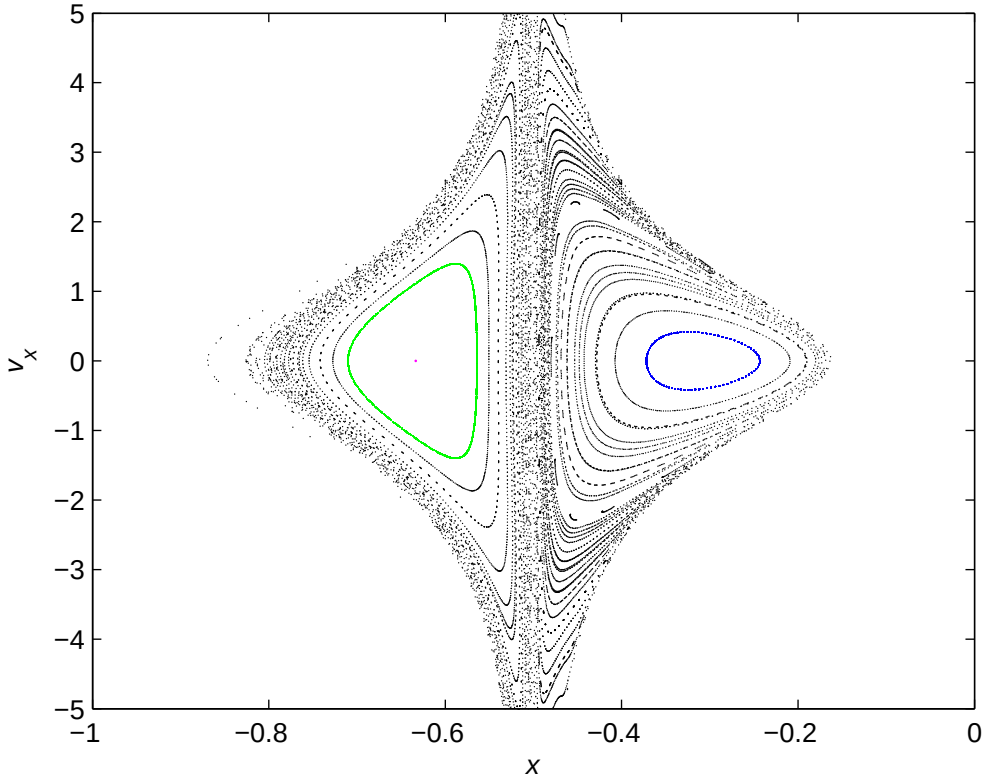

Fig. 3.22. Surface of Section for $C = 4.5$ and $\mu = 0.5$ with Crossings Corresponding to Quasi-periodic Orbits

chain of islands; rather the points fill a surface that encompasses more than half the domain. A surface of section for a value of $\mu = 0.5$ and $C = 3.5$ is plotted in Fig. 3.25. There remain quasi-periodic orbits corresponding to the closed curves or to chains of islands, but the chaotic regions predominate. To illustrate the behavior in this region, a chaotic trajectory is plotted in Fig. 3.26. For reference, the first 20 crossings with the hyperplane are plotted in blue in Fig. 3.25; the dots representing each crossing are enlarged to aid in visualization. As the energy level varies, the surface of section changes in character, and one particular structure may become more predominant than another. Hénon considered systems with $C < 3.456796...$, that is, energy levels such that the orbits are no longer Hill stable. In such systems, there remain quasi-periodic motions corresponding to closed curves or to chains of islands, but almost

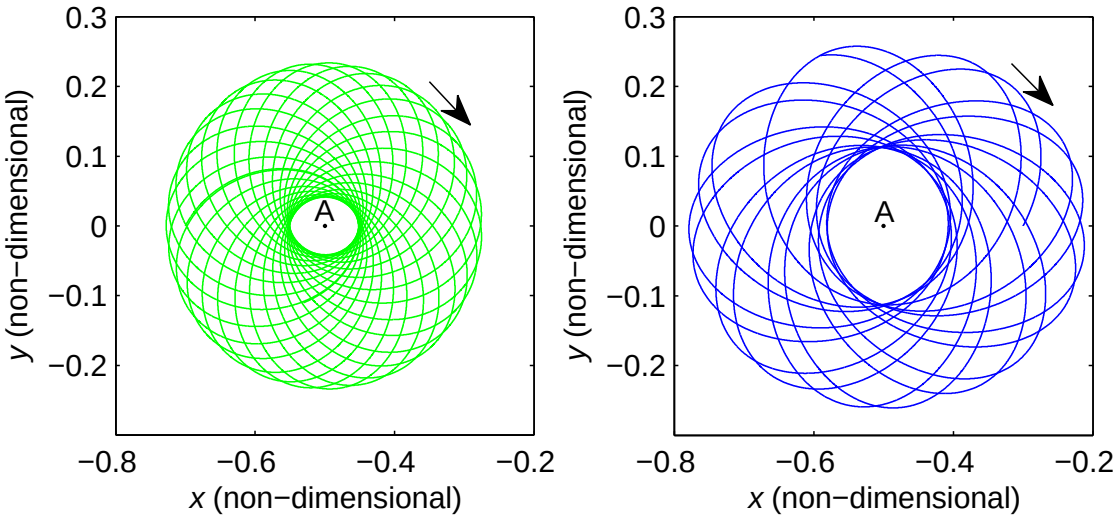

Fig. 3.23. Quasi-periodic Orbits in the Vicinity of A Corresponding to $C = 4.5$, $\mu = 0.5$

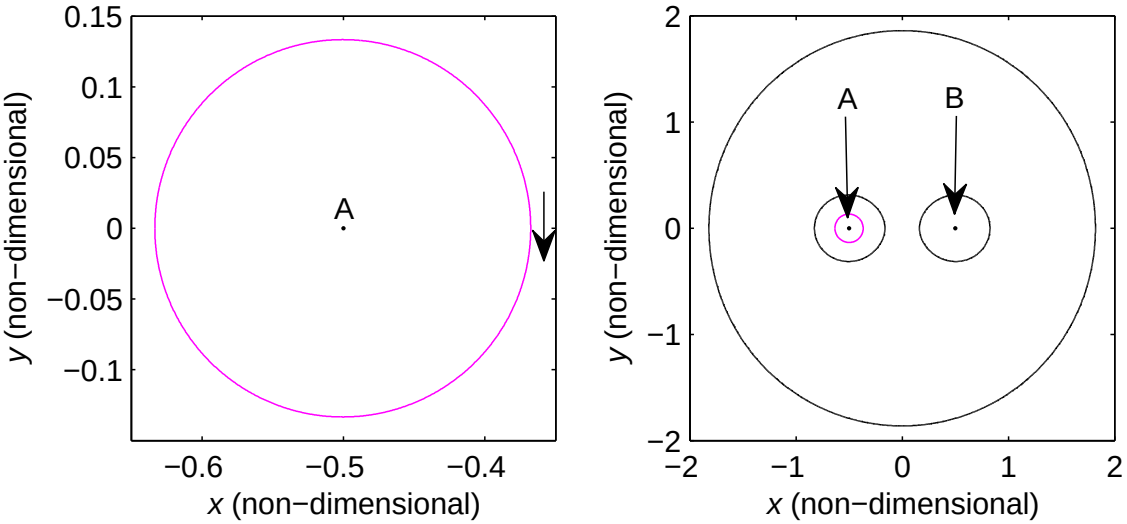

Fig. 3.24. Periodic Orbit in the Vicinity of A Corresponding to $C = 4.5$, $\mu = 0.5$

all motions outside the largest closed curves lead to an escape of the small mass to infinity. However, closed curves of islands demonstrate the possibility of bounded motion even below the limit of Hill stability.

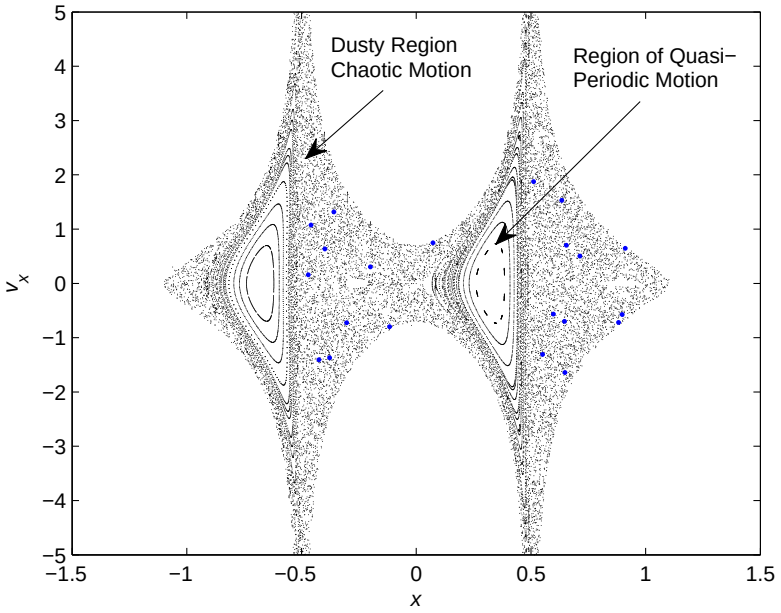

Fig. 3.25. Hénon Surface of Section for $C = 3.5$ and $\mu = 0.5$ with Chaotic Trajectory Crossings

3.4 The Jovian and Saturnian Systems

The majority of this investigation is focused on resonant trajectories in the Jupiter-Europa and Saturn-Titan systems. Therefore, this section offers useful physical parameters and notable characteristic quantities in the CR3BP that correspond to these systems.

The Jovian system is comprised of Jupiter and its four primary moons, ranging from larger to smaller in terms of mean radius: Ganymede, Callisto, Io and Europa. These Jupiter satellites are often termed the Galilean Moons, after their discovery in 1610 by Galileo [5]. The Saturnian system is comprised of Saturn plus its primary

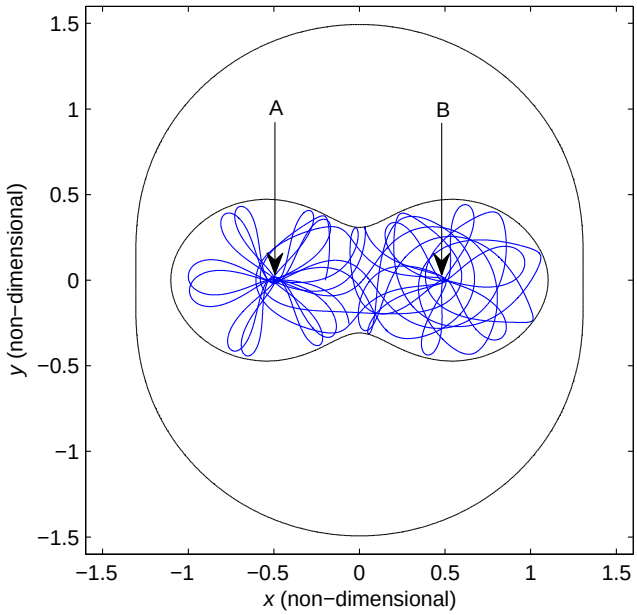

Fig. 3.26. Chaotic Trajectory with Zero Velocity Curves in the Vicinity of A Corresponding to $C = 3.5$, $\mu = 0.5$

moons, from larger to smaller mean radius: Titan, Rhea, Iapetus, Mimas, Enceladus, Tethys, Dione, and Hyperion. Titan, Saturn's largest moon and the second largest moon in the solar system, was discovered in 1655 by Huygens [46]; Tethys, Dione, Rhea, and Iapetus were identified in 1671-1672 by Cassini [46]; Mimas and Enceladus were discovered in 1789 by Herschel [46], and Hyperion was first observed in 1898 by Bond and Lassell [46].

3.4.1 The Jupiter-Europa and Saturn-Titan Systems

Within the Jovian and Saturnian systems, the emphasis is on two particular planet-moon combinations: Jupiter-Europa and Saturn-Titan. These two systems are of special interest for many scientific reasons. Saturn's moon Titan was the focus of the NASA-ESA *Huygens-Cassini* robotic spacecraft mission [47]. The *Cassini-Huygens* spacecraft reached Saturn in 2004 with the purpose of mapping Titan's

surface by radar. In 2005, the probe *Huygens* landed on Titan's surface while the *Cassini* spacecraft initiated a series of planned, targeted close flybys of Titan, proving the mission to be extremely successful, and providing the scientific community with valuable information about Titan. Jupiter's moon Europa is also scientifically interesting. Recently, much attention has been focused on Europa because of previous observations of its icy and smooth surface. In 1979, NASA's *Voyager* spacecraft processed valuable images of Europa, allowing scientists to speculate about its interior composition [48]. Today, most planetary scientists believe that a layer of liquid water exists beneath Europa's surface [49]. As a result of these scientific discoveries and theories, feasible trajectories near these moons may someday serve as the basis for future missions.

For completeness and to facilitate the understanding of the results presented in this investigation, the values of various physical parameters and charateristics quantities in the CR3BP are listed in Tables 3.5, 3.6, and 3.7. The data provided in the following three tables is obtained or calculated from the Jet Propulsion Laboratory Solar System Dynamics website [50], which provides information related to orbits and physical characteristics of most natural bodies in the known solar system. Some of the relevant physical properties of the planets and their satellites, that is, Jupiter, Europa, Saturn, Titan, and Enceladus appear in Table 3.5. The gravitational parameter, μ_G, is equal to the mass of the body times the well known gravitational constant, G, and should be clearly distinguished from the CR3BP mass fraction, μ. A few significant orbital parameters, that is, gravitational parameter, orbital period, and semi-major axis are listed in Table 3.6. The values for the mass fraction, μ, and the semi-major axis, a, are calculated from the masses and periods using Eq. (2.14) and Eq. (3.3), respectively. The values of the Jacobi constant at the libration points are useful as a reference when compared to the energy levels corresponding to periodic orbits and other trajectories from this analysis. The Jacobi constant values at each of the libration points in the Jupiter-Europa and Saturn-Titan systems appear in Table 3.7. Recall that the same values in the Earth-Moon system are in Table 2.1.

Table 3.5
Physical Constants

Body	μ_G (km^3/s^2)	Mean Radius (km)
Jupiter	1.266622×10^8	69,911.0
Europa	3202.739000	1,560.8
Saturn	3.792392×10^7	58,232.0
Titan	8.978138×10^3	2,575.5
Enceladus	7.202700	252.1

Table 3.6
CR3BP Constants

System	μ	Orbital Period (days)	Semi-major Axis (km)
Jupiter-Europa	2.526644×10^{-5}	3.552412	671,101.0
Saturn-Titan	2.366846×10^{-4}	15.949398	1,221,865.0
Saturn-Enceladus	1.899249×10^{-7}	1.371437	238,037.0

Table 3.7
Values of Jacobi constant at the Libration Points

Jupiter-Europa system	Jacobi constant	Saturn-Titan system	Jacobi constant
C_{L_1}	3.003643	C_{L_1}	3.015769
C_{L_2}	3.003609	C_{L_2}	3.015453
C_{L_3}	3.000025	C_{L_3}	3.000236
C_{L_4}	2.999974	C_{L_4}	2.999763
C_{L_5}	2.999974	C_{L_5}	2.999763

4. RESONANCE TRANSITION

Given the necessary background in periodic orbits and dynamical systems theory, the relationship between unstable resonant orbits and their invariant manifolds is explored. Unstable resonant orbits in the Jupiter-Europa and Saturn-Titan systems are considered, including the resonances involved in the Europa Orbiter flyby trajectory. A technique to estimate resonant ratios from a surface of section is detailed, and Poincaré maps are employed to display the associated stable and unstable manifolds. In addition, to demonstrate the presence of a chaotic dynamical environment, various homoclinic connections are computed.

4.1 Unstable Resonant Orbits

The determination of stable periodic orbits from a surface of section is fairly straightforward, since their locations are readily identified. Stable periodic orbits can be computed using a variety of techniques, as detailed in Section 3.3. However, the determination of unstable orbits in chaotic regions is more challenging. Once a point in the Poincaré section is identified as a potential unstable resonant orbit, it is not trivial to compute the actual trajectory in the CR3BP if the period is unknown. A strategy to automatically determine the p:q ratio for a potential resonant orbit from its location in the map is summarized. This technique involves the use of Poincaré sections and two-body approximations as initial conditions to a differential corrections scheme.

4.1.1 A Strategy to Estimate Resonant Ratios from a Surface of Section

To exploit the stable and unstable manifolds for transfers, unstable resonant orbits must be available. The first step in the determination of an unstable resonant orbit from a Poincaré section is the selection of the position and velocity values from the map, that is, $[x, y, z]$ and $[\dot{x}, \dot{y}, \dot{z}]$. Recall that for planar resonant orbits $y = z = 0$, and due to periodicity, $\dot{x} = \dot{z} = 0$. The value for $\dot{y}$ is computed from Eq. (3.21), so the state obtained from the surface of section possesses the form $[x, 0, 0, 0, \dot{y}, 0]$. After the values for x and $\dot{y}$ are identified, it is necessary to transform the state from rotating to inertial coordinates via the BKE in Eq. (2.20), that is,

$$\bar{r}_i = [x_0 \;\; 0 \;\; 0]^T \tag{4.1}$$

$$\bar{v}_i = [0 \;\; sin\theta(\dot{x}_0 - \omega y_0) + cos\theta(\dot{y}_0 + \omega x_0)) \;\; 0]^T \tag{4.2}$$

where $\bar{r}_i$ and $\bar{v}_i$ represent the position and velocity vectors in inertial coordinates, with an origin at the barycenter of the system. Recall that initially, $t = 0$, $\theta = 0$, $\omega = 0$, and μ is the CR3BP mass fraction parameter. The following transformation is used to translate the state in inertial coordinates from the barycenter to body-centered coordinates, that is,

$$\bar{r}_b = (\bar{r}_i + \mu[cos(t) \;\; sin(t) \;\; 0]^T)l^* \tag{4.3}$$

$$\bar{v}_b = (\bar{v}_i + \omega\mu[-sin(t) \;\; cos(t) \;\; 0]^T)\frac{l^*}{t^*} \tag{4.4}$$

where $\bar{r}_b$ and $\bar{v}_b$ represent the position and velocity vectors in body-centered intertial coordinates. Notice that the position and velocity are now expressed in dimensional units, that is, km and km/sec, respectively. The values for the semi-major axis

and eccentricity are instantaneously computed from the equations for the angular momentum vector, $\bar{h}$, and the semilatus rectum, p, that is,

$$\bar{h} = \bar{r}_b \times \bar{v}_b \tag{4.5}$$

$$\bar{e} = \frac{\bar{v}_b \times \bar{h}}{\mu_{2B}} - \frac{\bar{r}_b}{|\bar{r}_b|} \tag{4.6}$$

$$e = \sqrt{\bar{e} \cdot \bar{e}} \tag{4.7}$$

$$p = \frac{h^2}{\mu_{2B}} \tag{4.8}$$

$$a = \frac{p}{1 - e^2} \tag{4.9}$$

where μ_{2B} is the gravitational parameter. The calculation of the orbital elements in Eq. (4.7) and Eq. (4.9) is necessary to determine the instantaneous period of the resonant orbit, and hence, the resonant ratio p:q, that is,

$$P = 2\pi\sqrt{\frac{a^3}{\mu_{2B}}} \tag{4.10}$$

$$\frac{p}{q} = \frac{P_{moon}}{P_{s/c}} = \frac{2\pi t^*}{P} \tag{4.11}$$

The values for e, a, and P are used to compute the approximate two-body resonant orbit. The number of loops in the resonant trajectory, as observed in the rotating frame, determines p in the p:q ratio, so q can be easily computed from the value of p and the ratio in Eq. (4.11). Then, the values for position and velocity obtained from the surface of section and the p:q ratio obtained from the two-body approximation are used as the initial condition in the corrections algorithm to compute the desired resonant orbit in the CR3BP. However, these initial conditions, when employed in the corrections algorithm described in Section 2.4, may not lead to a periodic orbit with the exact same value of Jacobi constant as that of the energy level at which the Poincaré section is computed. Therefore, the corrections scheme forces the algorithm to search for a perpendicular crossing and to target a specific value of Jacobi constant. These constraints ensure that the resulting unstable resonant orbit exists at the correct energy level. This type of algorithm is labeled 'Jacobi constant targeter' in

this investigation. This targeter is essentially identical to the single shooting routine described in Section 2.4; the scheme is extended to incorporate one more variable, that is, δC_f. Recall the set of linear variational equations, written in matrix form in Eq. (2.102), and the expression for Jacobi constant in Eq. (2.36). Using the same simplifications discussed in Section2.4, the variational equations in Eq. (2.102) reduce to,

$$\begin{pmatrix} \delta x_0 \\ \delta \dot{y}_0 \\ \delta \tau_f \end{pmatrix} = \begin{pmatrix} \phi_{21} & \phi_{25} & \dot{y}_f \\ \phi_{41} & \phi_{45} & \ddot{x}_f \\ \frac{\partial C}{\partial x_0} & \frac{\partial C}{\partial \dot{y}_0} & 0 \end{pmatrix}^{-1}_{\tau_f} \begin{pmatrix} \delta y_f \\ \delta \ddot{x}_f \\ \delta C_f \end{pmatrix} \tag{4.12}$$

The partials in Eq. (4.12) are calculated as,

$$\frac{\partial C}{\partial x_0} = 2x - \frac{2(1-\mu)(x+\mu)}{(\sqrt{(x+\mu)^2+y^2+z^2})^3} - \frac{2\mu(x-1+\mu)}{(\sqrt{(x-1+\mu)^2+y^2+z^2})^3} \tag{4.13}$$

$$\frac{\partial C}{\partial \dot{y}_0} = -2\dot{y} \tag{4.14}$$

and are evaluated at τ_f. This system of equations is further reduced by incorporating the expression for the variation in the final time, $\delta\tau_f$, given in Eq. (2.108) . This expression can be substituted into Eq. 4.12, resulting in a system of two equations in two unknowns, that is,

$$\begin{pmatrix} \delta x_0 \\ \delta \dot{y}_0 \end{pmatrix} = \begin{pmatrix} \phi_{41} - \frac{\ddot{x}_f}{\dot{y}_f}\phi_{21} & \phi_{45} - \frac{\ddot{x}_f}{\dot{y}_f}\phi_{25} \\ \frac{\partial C}{\partial x_0} & \frac{\partial C}{\partial \dot{y}_0} \end{pmatrix}^{-1} \begin{pmatrix} \delta \dot{x}_f \\ \partial C_f \end{pmatrix} \tag{4.15}$$

Recall that ϕ_{41}, ϕ_{21}, ϕ_{45}, and ϕ_{25} are components of the STM. This strategy includes two-body approximations to estimate the period of the orbit and a Jacobi constant targeter. In combination, this technique is successfully employed to determine unstable resonant orbits from surfaces of sections.

4.2 Computation of Invariant Manifolds Associated with Resonant Orbits

The computation of invariant manifolds that are associated with unstable resonant orbits requires the monodromy matrix. Given the STM after exactly one period

of the orbit, the unstable and stable directions are available via the eigenvectors. Generation of a series of trajectories in these directions is described in section 3.2. The trajectories along the invariant manifolds corresponding to the unstable resonant orbits possess their own distinctive behavior. However, the trajectories are tangled, so plotting these trajectories in the xy-plane does not offer any insight. In contrast to libration point orbits, the trajectories on the resonant orbit manifolds frequently pass close to different resonances, but also remain in the vicinity of the original resonant orbit in configuration space [5]. A Poincaré section that reflects the behavior in the vicinity of these resonant periodic orbits and the manifolds also emerges. These manifold trajectories aid in visualization and provide valuable insight concerning the relationship between these manifolds and other structures in the phase space.

Two specific parameters are key in the computation of invariant manifolds associated with unstable periodic orbits and their display in a Poincaré section: the size and the direction of the offset along the eigenvector. For libration point orbits, this offset is assessed in both the positive and negative eigendirections to obtain the global behavior of the stable and unstable manifolds, respectively. To "fill out" the curves representing the invariant manifolds in the Poincaré section, it is desirable to use a series of offsets and short integration times [5]. The offset values range from 0.1 to 10 km in the Jupiter-Europa and Saturn-Titan systems, which are similar to the distances used in other studies [5]. It is observed that using more fixed points along the orbit to compute the manifolds leads to more well-defined curves in the surface of section.

As an illustrative example of the computation and representation of the invariant manifolds associated with an unstable resonant orbit in a Poincaré map, consider the 2:3 resonant trajectory in Fig. 4.1. Observe that $p = 2$ but the orbit includes a double loop in the vicinity of Titan. For reference, Table 4.1 includes the non-zero initial conditions, eigenvalues, and the value of the Jacobi constant corresponding to this periodic orbit, with an orbital period of 66.986 days. The eigenstructure from the monodromy matrix in the vicinity of this orbit indicates that it is unstable with a

large positive real eigenvalue. In fact, the stability index computed from Eq. 3.15 is equal to $\nu = 6,442.220$. A noticeable feature of this resonant orbit is the formation of a double loop in the vicinity of Titan. Hence, to distinguish this type of 2:3 resonant orbit from other 2:3 resonant orbits, it is labeled as a "double-loop 2:3 resonant orbit" in this investigation. To compute some of the stable and unstable manifolds associated with this trajectory, a total of 40 fixed points are selected along the resonant orbit at evenly spaced time intervals, represented as black dots in Fig. 4.1. A single offset value of 10 km is defined in both the positive and negative eigen-directions. The integration time is 50 non-dimensional time units, equivalent to 126.88 days. The resulting trajectories along the manifolds are plotted in Fig. 4.2 in the xy-plane. The stable manifolds are represented in blue and labeled $W^s_{2:3}$ and the unstable manifolds are plotted in magenta, labeled $W^u_{2:3}$.

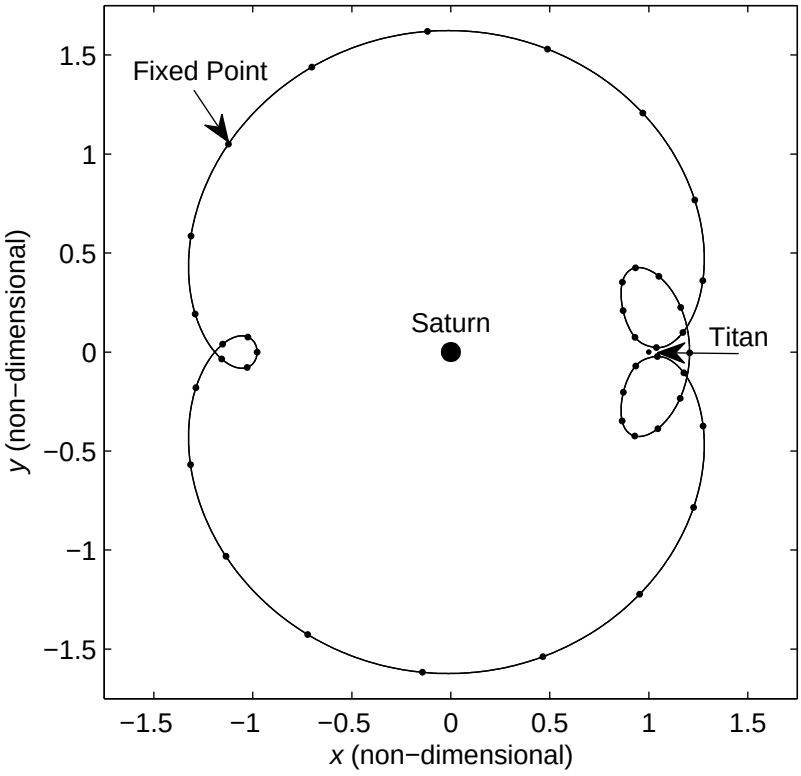

Fig. 4.1. Double-loop Planar 2:3 Resonant Orbit in the Saturn-Titan System

Table 4.1
Non-zero Initial Conditions, Unstable and Stable Eigenvalues, and Jacobi Constant for the Double-loop 2:3 Resonant Orbit - Saturn-Titan System

x (km)	$\dot{y}$ (km/sec)	C	λ_u	λ_s
-1,195,287.8	-0.843470	2.978775	12,884.44	7.761298×10^{-5}

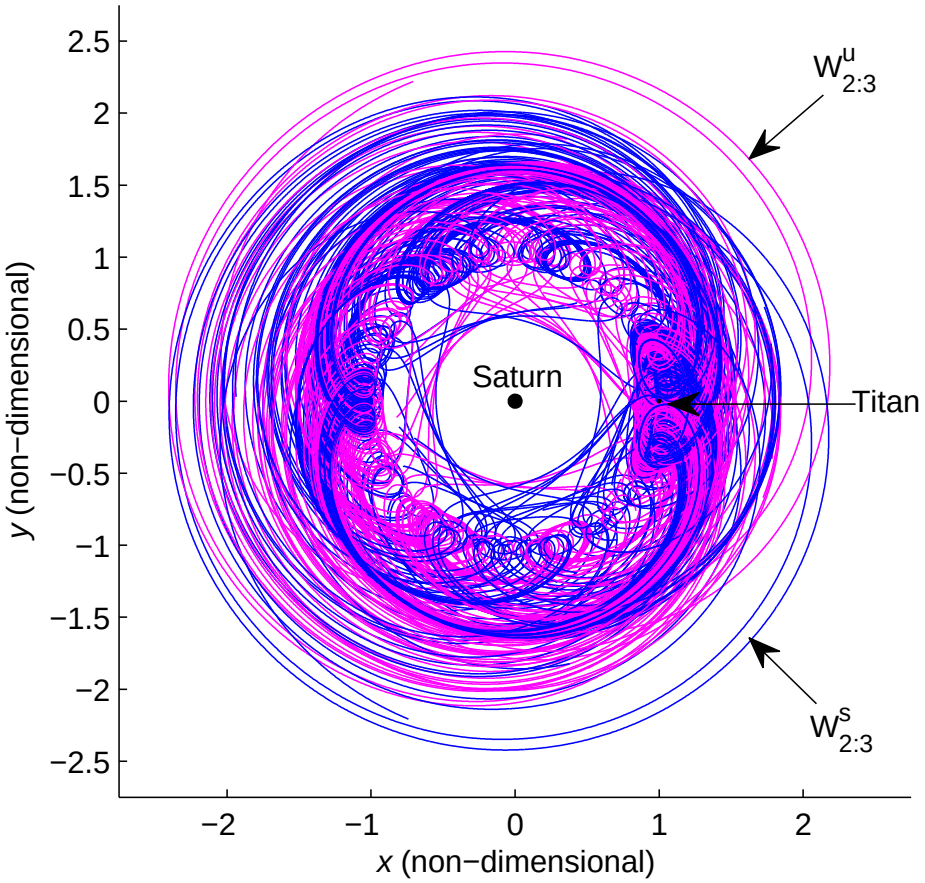

Fig. 4.2. Invariant Manifolds of the Double-loop Planar 2:3 Resonant Orbit in the Saturn-Titan System (Characteristic Distance $l^* = 1,221,830$)

As illustrated in Fig. 4.2, identifying a manifold structure or any characteristic behavior emanating from this double-loop 2:3 resonant orbit becomes almost impos-

sible to discern when the manifolds are simply propagated forward and backward in time and plotted in configuration space. Yet, the goal of this investagation is an understanding of the invariant manifolds as a whole and their relationship to other dynamical structures. Potential transfers may exist between unstable resonant orbits via these invariant manifolds. An alternative approach to view the manifold structures and to pursue the dynamical relationships is Poincaré sections. The computation of a surface of section that reflects invariant manifolds is similar to the process detailed in section 3.3. The hyperplane Σ that defines the surface of section is placed to intersect the unstable orbit of interest; in this example, Σ is located such that y =0. Then, the manifolds originating near each fixed point along the unstable resonant orbit are integrated backward and forward in time to compute the global stable and unstable manifolds, respectively. These manifold trajectories are then integrated until they intersect the hyperplane, defined by $y = 0$, and the intersecting points are recorded and plotted. To illustrate the results of this method, consider the double-loop 2:3 resonant orbit plotted in Fig. 4.1, and the set of initial conditions in Table 4.1. Although the relationship between the manifolds representing the double-loop 2:3 resonant orbit and other structures in phase space are not initially apparent, the manifold structure is visually more apparent in a surface of section, as noted in Fig. 4.3. The returns on the map that correspond to the unstable manifold trajectories ($W^u_{2:3}$) are plotted in magenta and the returns associated with the stable manifolds ($W^s_{2:3}$) are represented in blue; x and $v_x = \dot{x}$ are the quantities selected for plotting.

4.3 Resonant Orbits in the Jupiter-Europa System

Recall that the motivation for this investigation is expanding the role of invariant manifolds in the design and optimization of interplanetary trajectories [2] [3] [4] [5]. Various authors consider these applications of invariant manifolds and have obtained promising results [2] [3] [4]. The Europa Orbiter is a sample mission investigated by Anderson and Lo for invariant manifold applications. The original Europa Orbiter

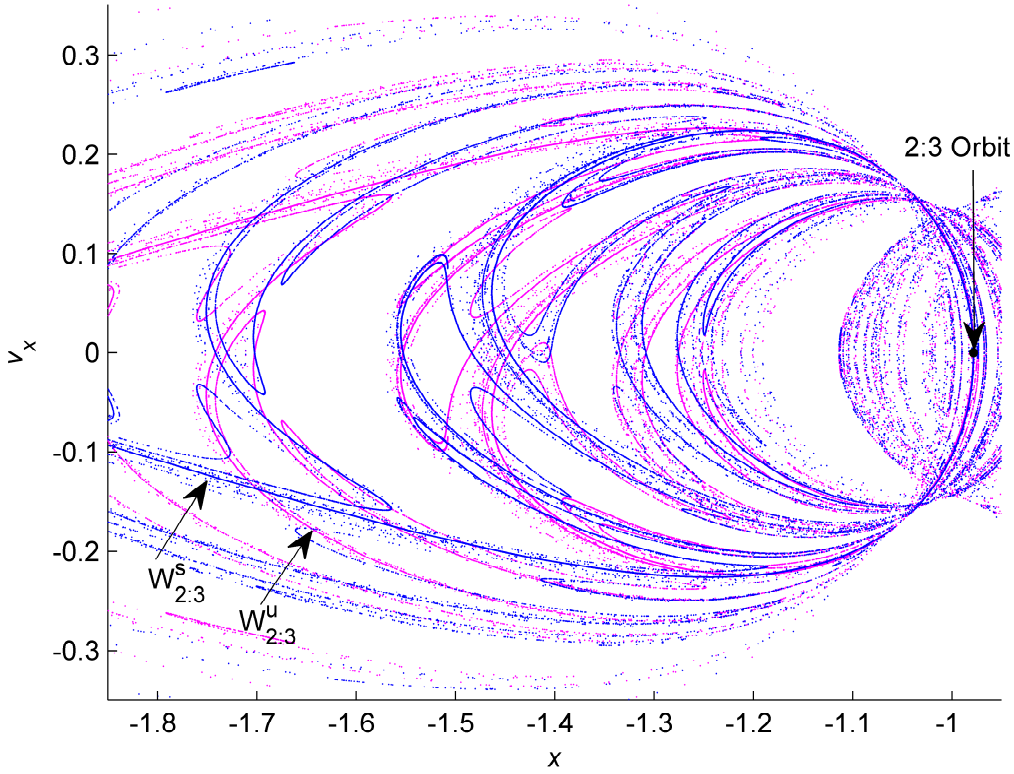

Fig. 4.3. Surface of Section Reflecting the Invariant Manifolds of the Double-loop Planar 2:3 Resonant Orbit in the Saturn-Titan System

trajectory was designed without the use of manifolds [51]. For example, various techniques are examined by Anderson and Lo in considering low-thrust trajectory design for Jovian moon missions, as well as the Europa Orbiter (EO) spacecraft.

In their investigations, Lo and Anderson (et al.) first use Poincaré sections to search for unstable resonant orbits in support of the Europa Orbiter mission concept [2] [3] [4]. The invariant manifolds from these unstable resonant orbits are then computed and indicate the transitions of the Europa Orbiter trajectory between resonances; eventually the spacecraft is captured into an orbit around Europa. The trajectory clearly exploits invariant manifolds associated with quasi-periodic orbits [3]. Extending the work of Lo and Anderson, this investigation focuses on the use of Poincaré sections to search for unstable resonant orbits and to aid in visualization of

their invariant manifold structure to search for potential resonance transitions. As a baseline, this study begins with a detailed investigation of the invariant manifolds associated with the two unstable resonant orbits involved in the EO trajectory, that is, a 3:4 and a 5:6 resonant orbit, respectively. The unstable resonant orbits are computed in the CR3BP using the technique described in Section 3.1.3. Two-body approximations are used as the initial guess and a corrections algorithm yields the periodic resonant orbits, subsequently plotted in Fig. 4.4(a) and Fig. 4.4(b). The corresponding initial conditions, Jacobi constant, unstable eigenvalue, and orbital period for both resonant orbits are listed in Table 4.2.

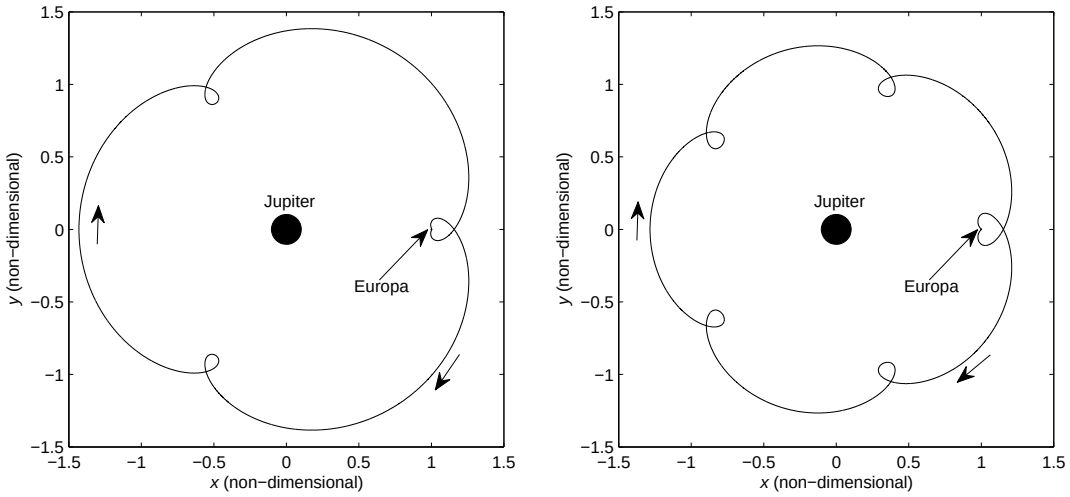

(a) 3:4 Resonant Orbit

(b) 5:6 Resonant Orbit

Fig. 4.4. Unstable Resonant Orbits in the Jupiter-Europa System

Once the unstable resonant orbits are identified and computed, their invariant manifolds are calculated and displayed in a surface of section using the techniques described in Section 4.2. The plots in Figs. 4.5-4.6 demonstrate the relationship between these resonant orbits, their manifolds, and the EO flyby trajectory as discovered by Anderson [5]. Figure 4.5 represents the invariant manifolds computed in conjunction with the 3:4 resonant orbit. The stable manifolds are plotted in green, and the unstable manifolds appear in red. The fixed points corresponding to the 3:4 and 5:6

Table 4.2
Initial Conditions, Jacobi Constant (JC), Unstable Eigenvalue (λ_{uns}), and Orbital Period for the 3:4 and 5:6 Unstable Resonant Orbits in the Jupiter-Europa System

p:q	x (km)	$\dot{y}$ (km/sec)	JC	λ_{uns}	Period (days)
3:4	-959,949.50	9.2438487	2.9916395	1,036.1161	14.513326
5:6	-861,829.36	6.3698436	2.9916395	4,445.3874	21.9149861

resonant orbits are represented as blue and orange dots, respectively. The black dot corresponds to the EO flyby trajectory. Similarly, the invariant manifolds corresponding to the 5:6 unstable resonant orbit are apparent in the section plotted in Fig. 4.6. To distinguish the 5:6 manifolds from the manifolds of the 3:4 resonant orbit, the stable and unstable manifolds originating with the 5:6 orbit are plotted in blue and orange, respectively. Recall that these sections are computed for the value of Jacobi constant associated with the flyby trajectory, that is, $C = C_{flyby} = 2.991639568304150$. The resemblance in the manifold structures associated with both orbits is immediately obvious. The manifolds from one orbit closely follow the manifolds of the other, so closely that it is difficult to distinguish between them. The energy level at which these sections are computed is determined by first computing the EO flyby trajectory and then calculating its energy level. From the section, it appears likely that a special relationship exists between these two resonant orbits at this particular energy level [5]. The close alignment of the invariant manifolds verifies this conjecture. The actual flyby trajectory possesses nearly the same state in phase space as some of the trajectories on the invariant manifolds. Thus, the flyby trajectory is indeed shadowing the invariant manifolds as it transitions between the resonances [5] [2] [3] [4].

With the purpose of gaining more insight into the problem, the plots in Fig. 4.5 and Fig. 4.6 are reproduced. The invariant manifolds associated with the 3:4 and 5:6 resonant trajectories are computed using a variety of offset values ranging from 0.1 to 10 km. The invariant manifolds originating with both orbits are computed from

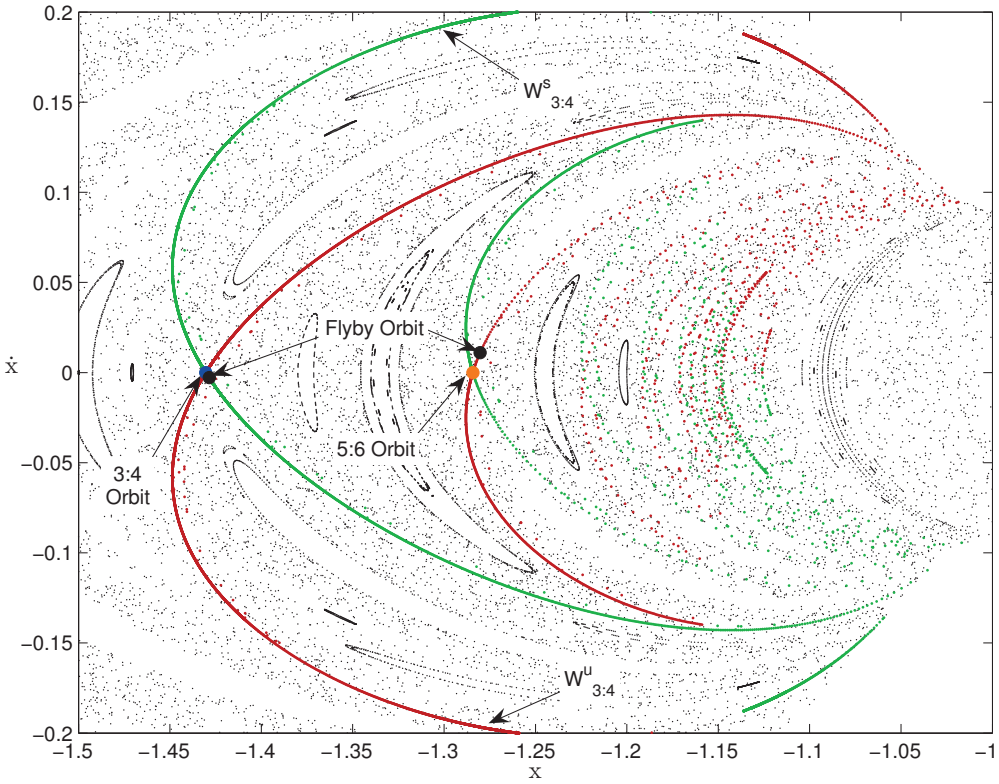

Fig. 4.5. Poincaré Section Illustrating the Relationship between the Invariant Manifolds of the 3:4 Resonant Orbit and the Flyby Trajectory (with Permission, Anderson [5])

a total of 40 fixed points evenly spaced in time along each orbit. The trajectories along the stable manifold are propagated backwards in time for 20 non-dimensional time units, equivalent to 11.3065 days. Similarly, the trajectories along the unstable manifold are integrated forward in time for the same period of time. For a view of the invariant manifolds as a whole and their relationship to other dynamical structures, it is necessary to plot them against a background that includes these structures. The set of initial conditions used to generate this surface of section is selected to be in the vicinity of the resonant orbits, that is, $-1.5 \leq x_0 \leq -1$ and $-0.25 \leq \dot{x}_0 \leq 0.25$. A planar problem, the bounds are defined with $y = 0$ and $z_0 = \dot{z}_0 = 0$; the corresponding value of $\dot{y}_0$ is calculated from the value of Jacobi constant using the

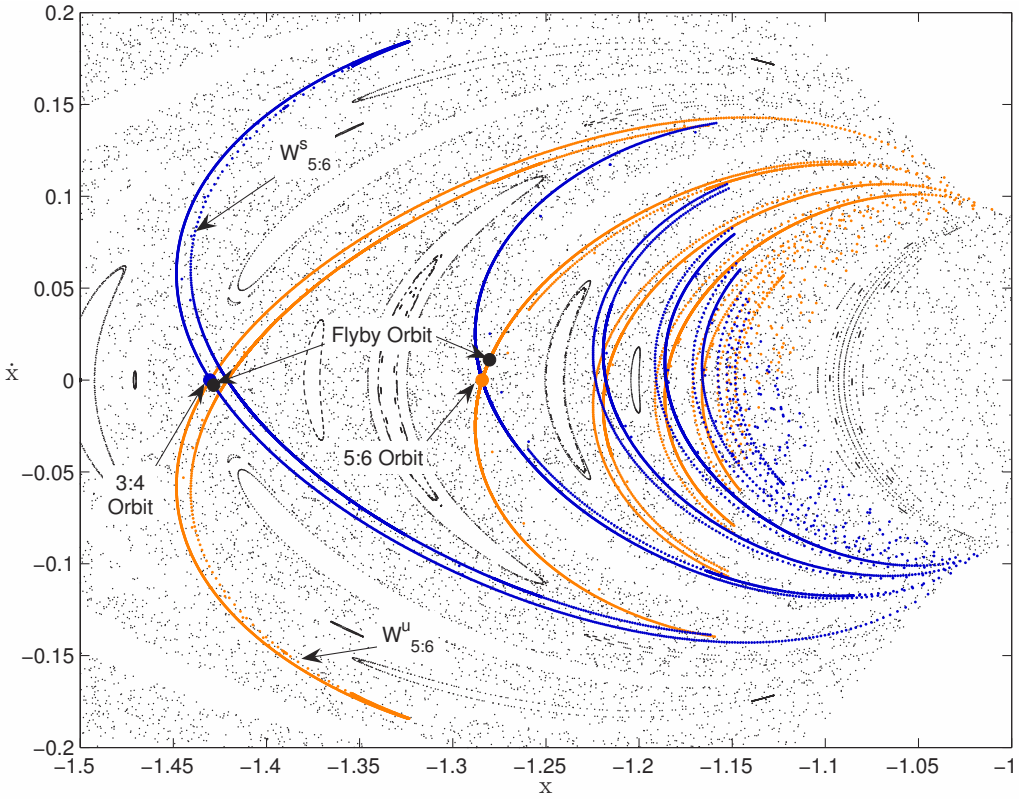

Fig. 4.6. Poincaré Section Illustrating the Relationship between the Invariant Manifolds of the 5:6 Resonant Orbit and the Flyby Trajectory (with Permission, Anderson [5])

relationship in Eq. (3.21). In propagating the initial conditions, long integration times are necessary to produce sufficient crossings to yield a dense and well-defined map. For this particular example, an integration time of approximately 38 years is employed to generate the background section in Fig. 4.7. The invariant manifolds associated with the 3:4 resonant trajectory appear in the figure plotted against a background map that inlcudes regions of both periodic and quasi-periodic motion. The stable manifolds are plotted in green, and the unstable manifolds appear in red. Similarly, the invariant manifolds originating from the 5:6 resonant trajectory are plotted in Fig. 4.8. The magenta curves represent the stable manifolds, and the unstable manifolds are orange in color.

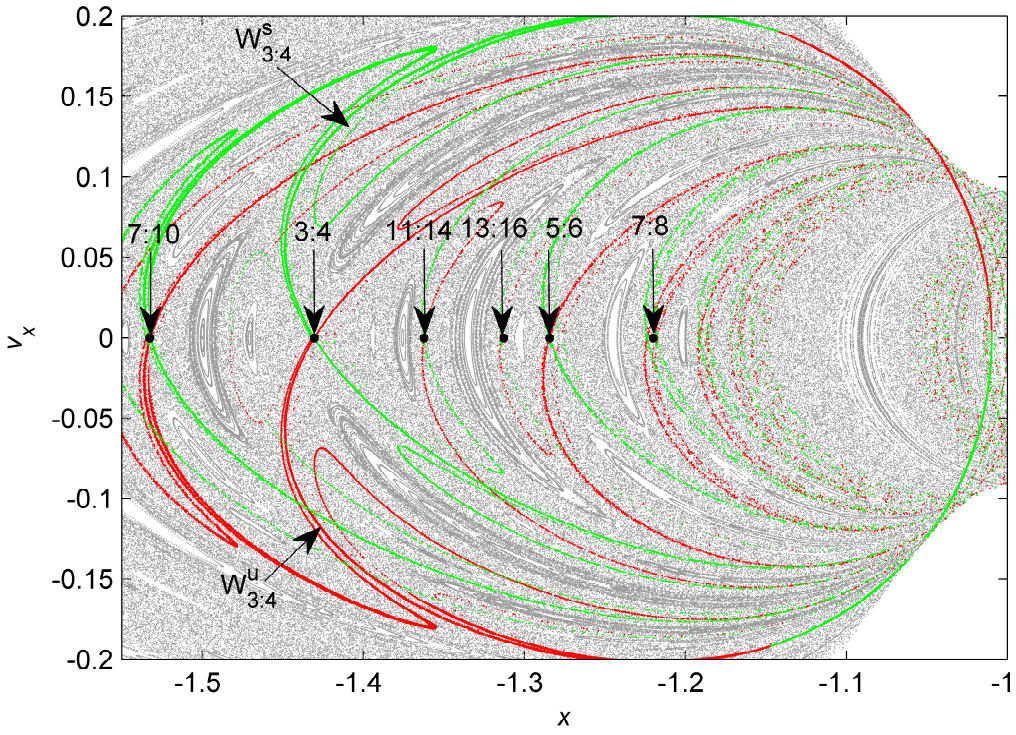

Fig. 4.7. Poincaré Section Illustrating the Relationship between the Invariant Manifolds of the 3:4 Resonant Orbit and Other Resonant Trajectories

From the plots in Fig. 4.7 and Fig. 4.8, it is clear that the invariant manifolds corresponding to the 3:4 and 5:6 resonant orbits are closely related, but it is also apparent that these manifolds travel to different regions in the map. Different areas of the map are potentially associated with other unstable resonant orbits, possibly leading to additional resonance transitions. Thus, it is necessary, at the given energy level, to further examine the relationship between the 3:4 and 5:6 resonances and other structures that are not necessarily related to the EO trajectory. Hence, some of the crossings of the invariant manifolds associated with the 3:4 resonant orbit are investigated using the methodology described in Section 4.1.1. Recall that this approach is employed to estimate the period of the potential resonant orbit from its intersection in the Poincaré map using two-body approximations. The estimated

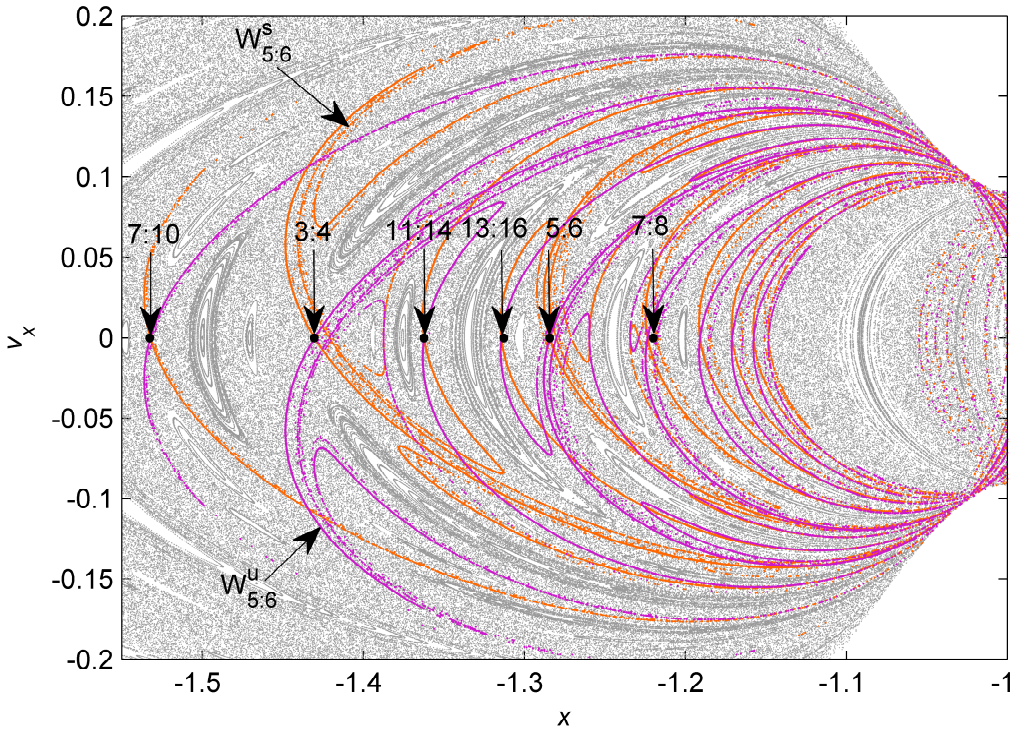

Fig. 4.8. Poincaré Section Illustrating the Relationship between the Invariant Manifolds of the 5:6 Resonant Orbit and Other Resonant Trajectories - Jupiter-Europa System

period and state from the map are then used as the initial guess in the corrections algorithm to compute the corresponding unstable resonant orbit in the CR3BP. As a result, 7:10, 11:14, 13:16, and 7:8 unstable resonant orbits are determined that expose manifold structures similar to those relating the 3:4 and 5:6 resonances. The intersection of these multiple unstable resonant orbits are labeled in Fig. 4.7, and the actual trajectories are plotted in Figs. 4.9(a)-4.9(d). For completeness, the corresponding initial states, unstable eigenvalues, and periods associated with these resonant trajectories are listed in Table 4.3. Note that the value of Jacobi constant reflecting the energy remains constant at $C = 2.991639568304150$.

Once the unstable resonant orbits are identified on the surface of section, it is necessary to compute their invariant manifolds to confirm that a transition is possible

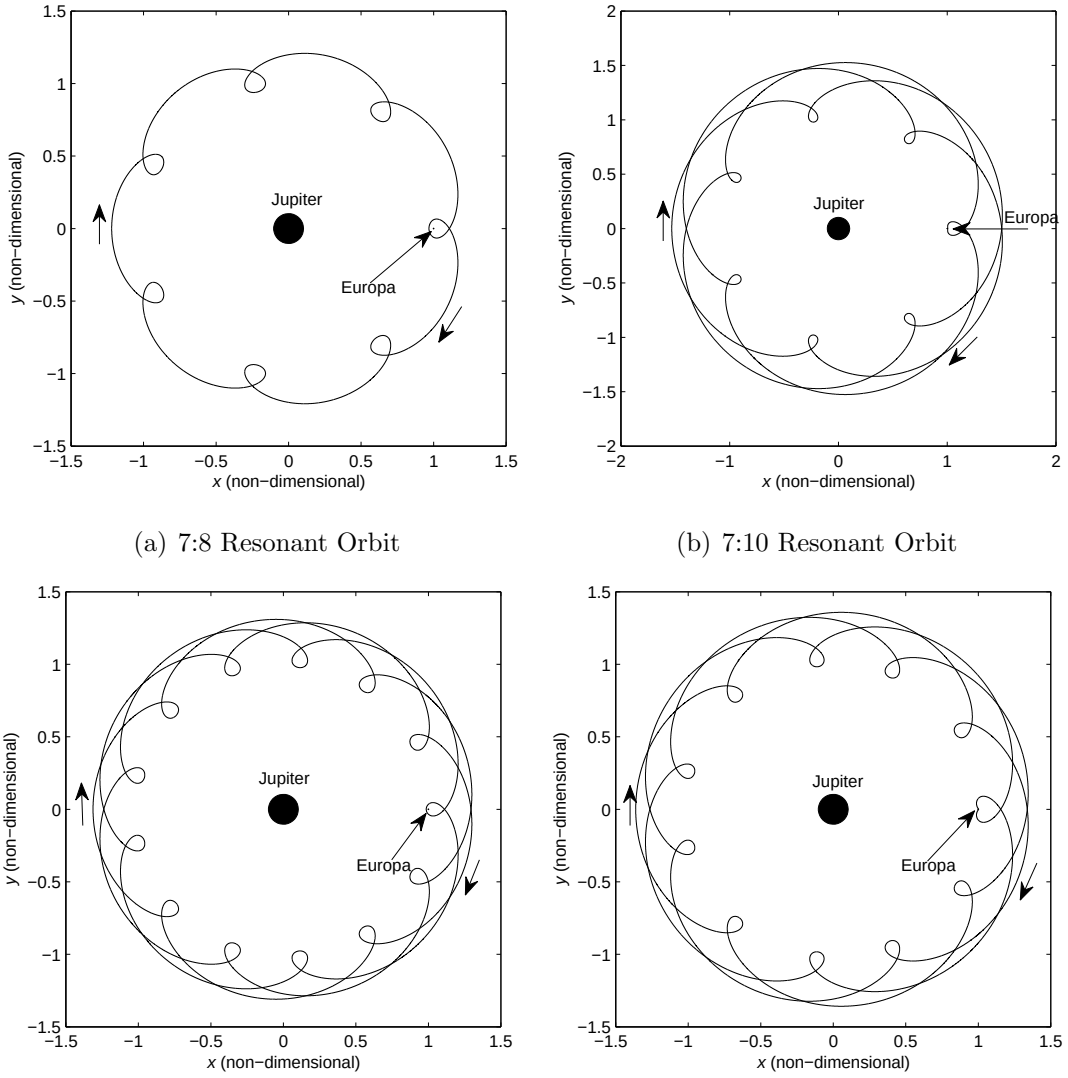

(a) 7:8 Resonant Orbit

(b) 7:10 Resonant Orbit

(c) 13:16 Resonant Orbit

(d) 11:14 Resonant Orbit

Fig. 4.9. Unstable Resonant Orbits in the Jupiter-Europa System

between these trajectories and the 3:4 and 5:6 resonant orbits. If such a relationship exists, then returns on the map corresponding to the invariant manifolds associated with each resonant orbit should approach the fixed point associated with each other resonance and intersect the corresponding manifold trajectories. That is, on the surface of section, the invariant manifolds of the 7:8 resonant orbit should approach each of the fixed points on the map linked to the 7:10, 13:16, and 11:14 resonant orbits

Table 4.3
Initial Conditions, Unstable Eigenvalue (λ_{uns}), and Orbital Period for the 7:10, 11:14, 13:16, and 7:8 Unstable Resonant Orbits in the Jupiter-Europa System (JC = 2.9916395, $l^* = 671101.96$ km)

p:q	x (km)	$\dot{y}$ (km/sec)	λ_{uns}	Period (days)
7:10	-1,028,550.00	11.181175	846.71229	35.692453
11:14	-91,420.045	7.9194395	5,215.8380	50.151184
13:16	-880,933.11	6.9392345	-110.22278	56.641668
7:8	-818,675.00	5.0670019	-28.149951	28.265081

to demonstrate that a transition exists between these resonances via their invariant manifolds. Likewise, the invariant manifolds of the 7:10, 13:16, and 11:14 resonant orbits should display a similar behavior. Thus, the stable and unstable manifolds corresponding to each of these orbits are computed and plotted in Figs. 4.10(a)-4.10(d). The intersections with each of the resonant orbits are labeled in the Poincaré map as well. The integration times that are required to compute the invariant manifolds varies from orbit to orbit. Of course, the manifolds for orbits that are more unstable depart or approach the orbit faster than the manifolds associated with orbits possessing a smaller stability index. In other words, the manifolds corresponding to the 11:14 resonant orbit, with $\lambda_u = 5,215.8380$, approach the other resonant orbits much faster than the manifolds associated with the 7:8 resonant trajectory, with $\lambda_s = -28.149951$. As expected, the similarities between the manifold structures are clear. At this particular energy, there exists a special relationship between more than two resonant orbits. The manifold trajectories corresponding to each resonant orbit approach each of the other resonant orbits identified in the section, as illustrated in Figs. 4.10(a)-4.10(b).

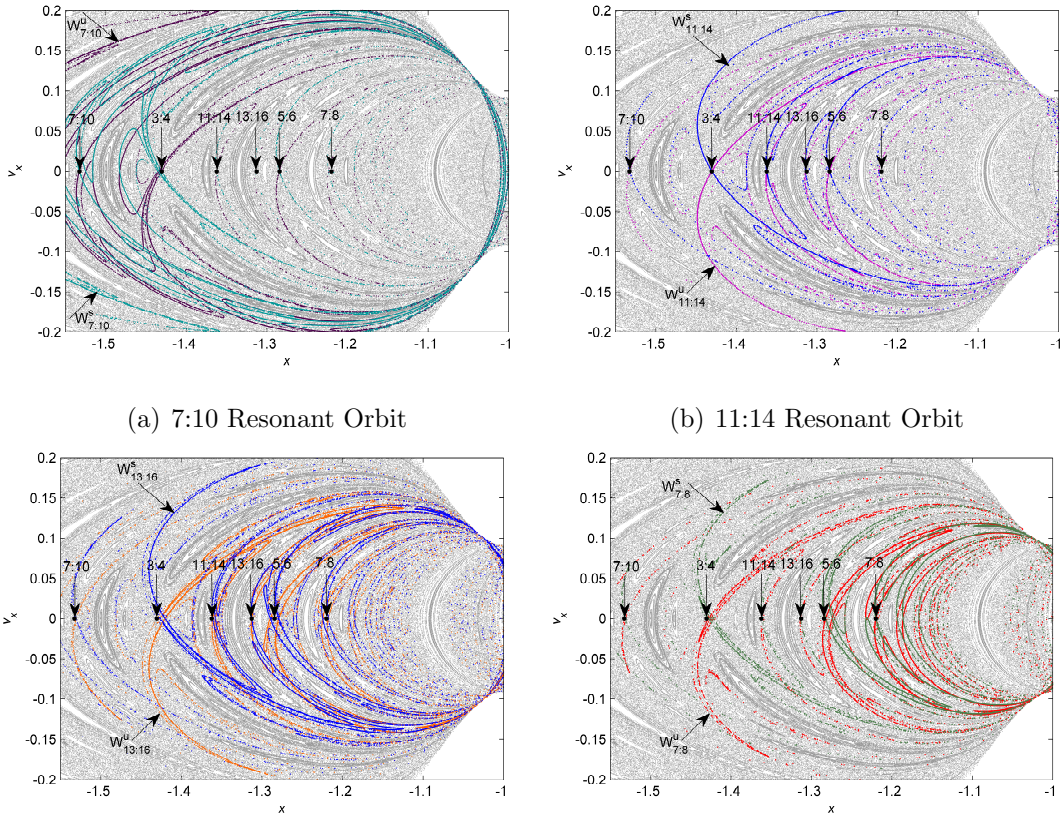

(a) 7:10 Resonant Orbit

(b) 11:14 Resonant Orbit

(c) 13:16 Resonant Orbit

(d) 7:8 Resonant Orbit

Fig. 4.10. Poincaré Section Illustrating the Relationship between the Invariant Manifolds of the 7:10, 11:14, 13:16, and 7:8 Resonant Orbit and Other Resonant Trajectories - Jupiter-Europa System

4.3.1 Homoclinic Connections in the Jupiter-Europa System

An intersection in the Poincaré map is an intersection in phase space. That is, an intersection of the stable and unstable manifolds on the Poincaré section - generated for a particular Jacobi constant - is a point that approaches the resonant orbit when integrated into the future as well as into the past [5]. Such trajectory is frequently termed a 'homoclinic' connection. Consider the invariant manifolds associated with the 3:4 unstable resonant orbit in Fig. 4.7. A homoclinic connection associated with the 5:6 resonant orbit can be determined from the intersection of

the stable and unstable manifolds corresponding to the 3:4 resonance near the fixed point on the Poincaré map corresponding to the 5:6 resonant orbit, as illustrated in Fig. 4.11. Hence, the path of the resulting trajectory is associated with both resonant orbits, that is, the 5:6 and the 3:4. To illustrate this relationship, the initial state of this homoclinic connection is integrated forward and backward in time for a half period and plotted in Fig. 4.12. For completeness, the initial conditions and orbital period for this homoclinic connection are summarized in Table 4.4. The integrated paths with the initial state near the return on the map of the 5:6 resonant orbit follow the invariant manifolds of the 3:4 resonant orbit, and thus, asymptotically arrive and depart the 3:4 resonant orbit after a half period. Since the manifolds corresponding to the 3:4 resonant orbit intersect very near the 5:6 resonant orbit, the homoclinic trajectory tends to follow both resonant paths. That is, for $0 \leq \tau \leq \frac{1}{4}P$, the homoclinic trajectory follows the 5:6 resonant trajectory, and for $\frac{1}{4}P \leq \tau \leq \frac{1}{2}P$, it switches to shadow the 3:4 resonant orbit. For $\frac{1}{2}P \leq \tau \leq \frac{3}{4}P$, it continues on the 3:4 resonant path, and finally, for $\frac{3}{4}P \leq \tau \leq P$, it returns to follow the 5:6 resonant trajectory, closing the cycle at the same point where it started.

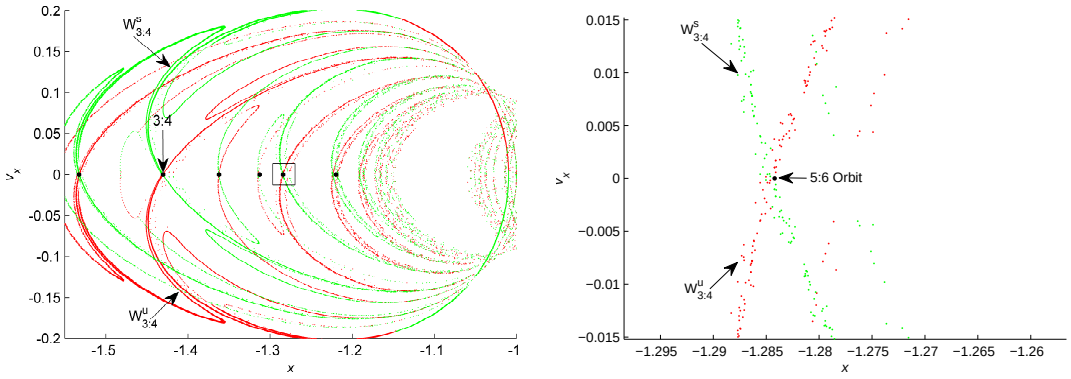

(a) Invariant Manifolds of the 3:4 Resonance

(b) Boxed Region

Fig. 4.11. Poincaré Section Illustrating the Relationship between the Invariant Manifolds of the 3:4 Resonant Orbit, the Homoclinic Connection and the 5:6 Unstable Resonant Orbit - Jupiter-Europa System

Similarly, another homoclinic connection is also identified at the intersection of the stable and unstable manifolds corresponding to the 7:10 resonant orbit, near the return of the 7:8 resonance in the Poincaré map (Fig. 4.10(a)). The behavior of this homoclinic connection is similar to that of the 3:4 homoclinic connection; such that it cycles between the two resonances. That is, for $0 \leq \tau \leq \frac{1}{4}P$, the homoclinic trajectory follows the 7:8 resonant path. At $\tau = \frac{1}{4}P$, it switches to the 7:10 resonant orbit until $\tau = \frac{3}{4}P$. Finally, for $\frac{3}{4}P \leq \tau \leq P$, it returns to the 7:8 resonant trajectory, arriving at the initial state after one full period. Recall that the initial state is computed from the intersection of the stable and unstable manifolds associated with the 7:10 resonant orbit near the return to the map of the 7:8 resonant path. To illustrate the relationship between the homoclinic connection and the 7:8 and 7:10 resonant orbits, the initial state computed from the Poincaré map is integrated forward and backward in time for a half period, and the results are plotted in Fig. 4.13. The corresponding initial conditions and orbital period for this homoclinic trajectory are listed in Table 4.4. Likewise, this trajectory with initial state near the 7:8 resonant follows the invariant manifolds of the 7:10 resonant orbit, and thus, approaches the 7:10 resonant trajectory asymptotically. The presence of these homoclinic trajectories certainly suggests the possibility of a chaotic dynamical environment [5], as small changes in initial conditions may lead to very different trajectories.

Table 4.4
Initial Conditions and Orbital Period for the 3:4 and 7:10 Homoclinic Connections - Jupiter-Europa System (JC = 2.9916395, $l^* =$ 671101.96 km)

Resonances	x (km)	$\dot{y}$ (km/sec)	Period (days)
5:6-3:4	-861,880.90	6.3713058	36.415757
7:10-7:8	-102,8550.00	11.181175	64.805980

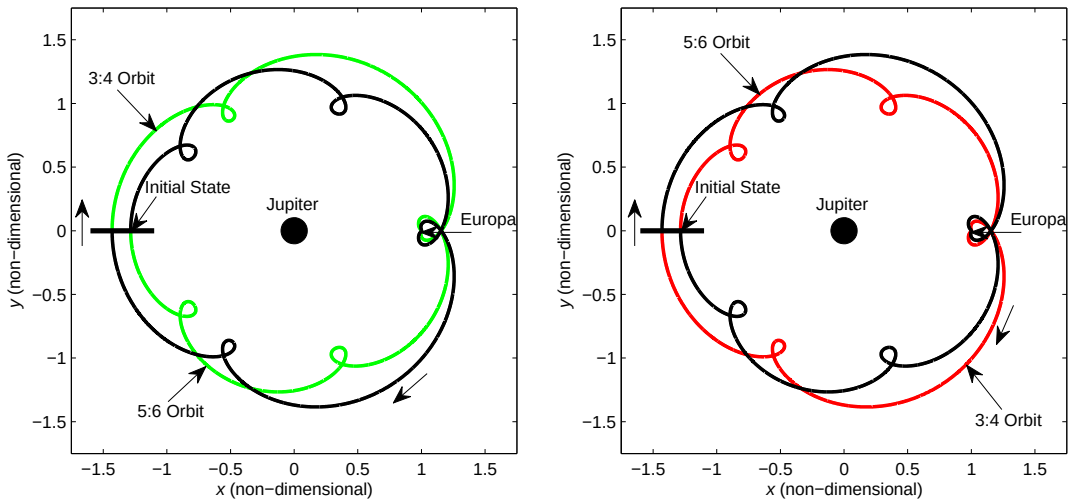

(a) Backward Integration (b) Forward Integration

Fig. 4.12. Homoclinic Trajectory in the Vicinity of a 5:6 Resonant Orbit - Jupiter-Europa System

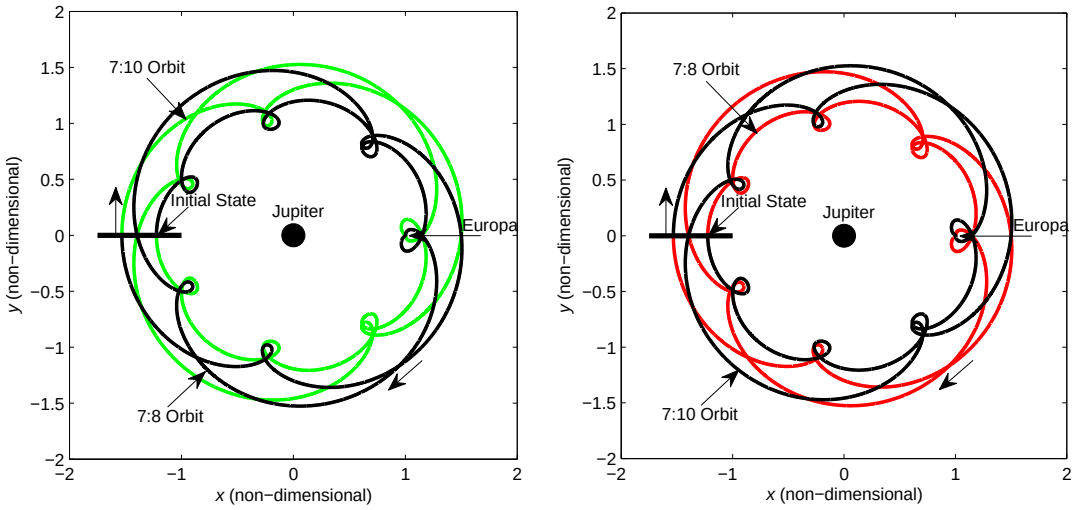

(a) Backward Integration (b) Forward Integration

Fig. 4.13. Homoclinic Trajectory in the Vicinity of a 7:8 Resonant Orbit - Jupiter-Europa System

4.4 Resonant Orbits in the Saturn-Titan System

Given the Europa Orbiter flyby trajectory, it is expected that some special relationship exists between the unstable 3:4 and 5:6 resonant orbits in the Jupiter-Europa system [5]; the flyby trajectory apparetly exploits invariant manifolds to transition between resonances. This relationship between the invariant manifolds is demonstrated in Section 4.3, but this type of relationship apparently also exists between other resonances at the same energy level, that is, the Jacobi constant value that corresponds to the EO trajectory. This type of relationship may not be unique to this particular system and energy level; it is likely to appear in other systems defined in terms of different μ and C values.

Consider the 2:3 double-loop resonant orbit plotted in Fig. 4.1. This particular resonant orbit is associated with a Jacobi constant value of $C = 2.97877552449866$ and a mass fraction $\mu = 2.365805221385698 \times 10^{-4}$, that is, the Saturn-Titan system. Recall that the initial state and the unstable eigenvalue corresponding to this trajectory are listed in Table 4.1. A series of unstable resonant orbits are computed in the Saturn-Titan system, but the double-loop 2:3 resonant trajectory is selected because it possesses the maximum absolute eigenvalue. The same methodology that is employed to compute the invariant manifolds associated with the resonant orbits in the Jupiter-Europa system is used again to investigate the manifold structure associated with this resonant trajectory in the Saturn-Titan system. A variety of offset values, ranging from 0.1 to 10 km, and relatively short integration times ($\tau = 80$ non-dimensional time units, equivalent to 203 days) are used to populate the curves representing the stable and unstable manifolds in the Poincaré section. The results, previously illustrated in Fig. 4.3, are now plotted in Fig. 4.14 against a background that also includes some of the other dynamical structures at this particular energy level. The unstable manifolds are represented in magenta, and the stable manifolds are plotted in blue. Some of the stable and unstable manifold intersections are investigated, and by employing the strategy described in Section 4.1.1 in conjunction with

a Jacobi constant targeter, a series of unstable resonant orbits are identified at this particular energy level. The intersections on the map corresponding to the resulting unstable resonant orbits are plotted as dots and labeled in Fig. 4.14. The actual trajectories corresponding to the 7:10, 5:8, and 3:4 resonances appear in Fig. 4.15(a), Fig. 4.15(b), and Fig. 4.15(c). One interesting feature that emerges in these unstable resonant orbits is the formation of a double loop in the vicinity of Titan, as seen in the 2:3 double-loop resonant orbit (Fig. 4.15(d)).

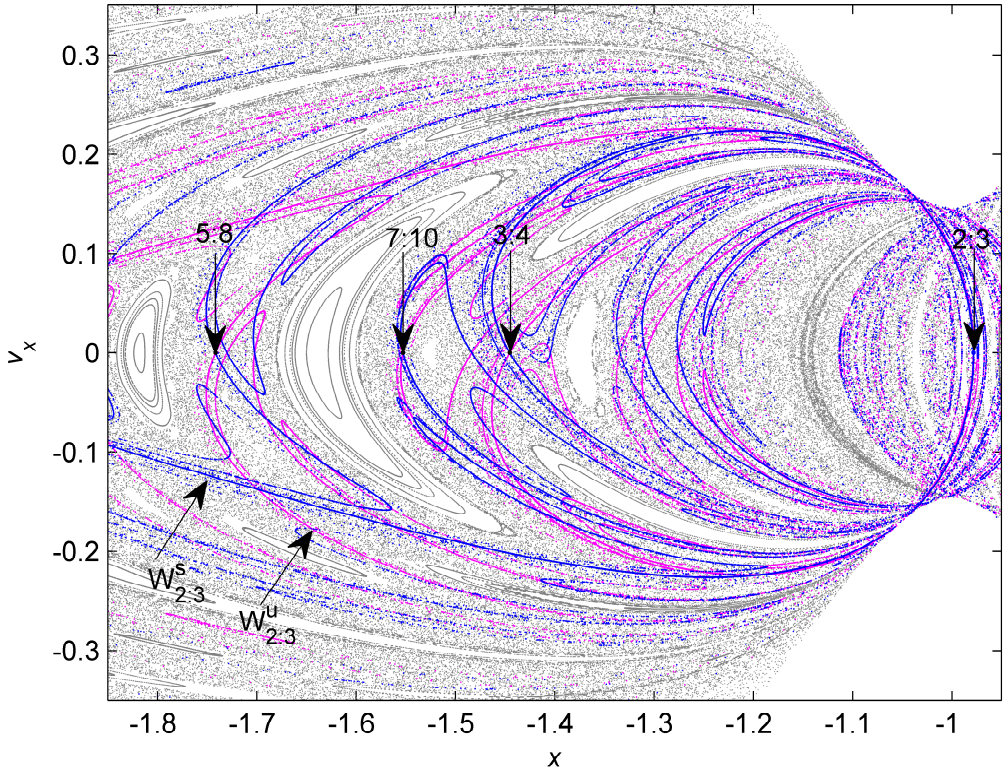

Fig. 4.14. Poincaré Section Illustrating the Relationship between the Invariant Manifolds of the 2:3 Resonant Orbit and Other Resonant Trajectories - Saturn-Titan System

To explore the possibility that a relationship exists between these four unstable resonant orbits at the given energy level, it is necessary to examine the manifold structure associated with each resonant orbit. If an intersection of the stable with the unstable manifolds occurs very near the fixed point on the map that is linked to

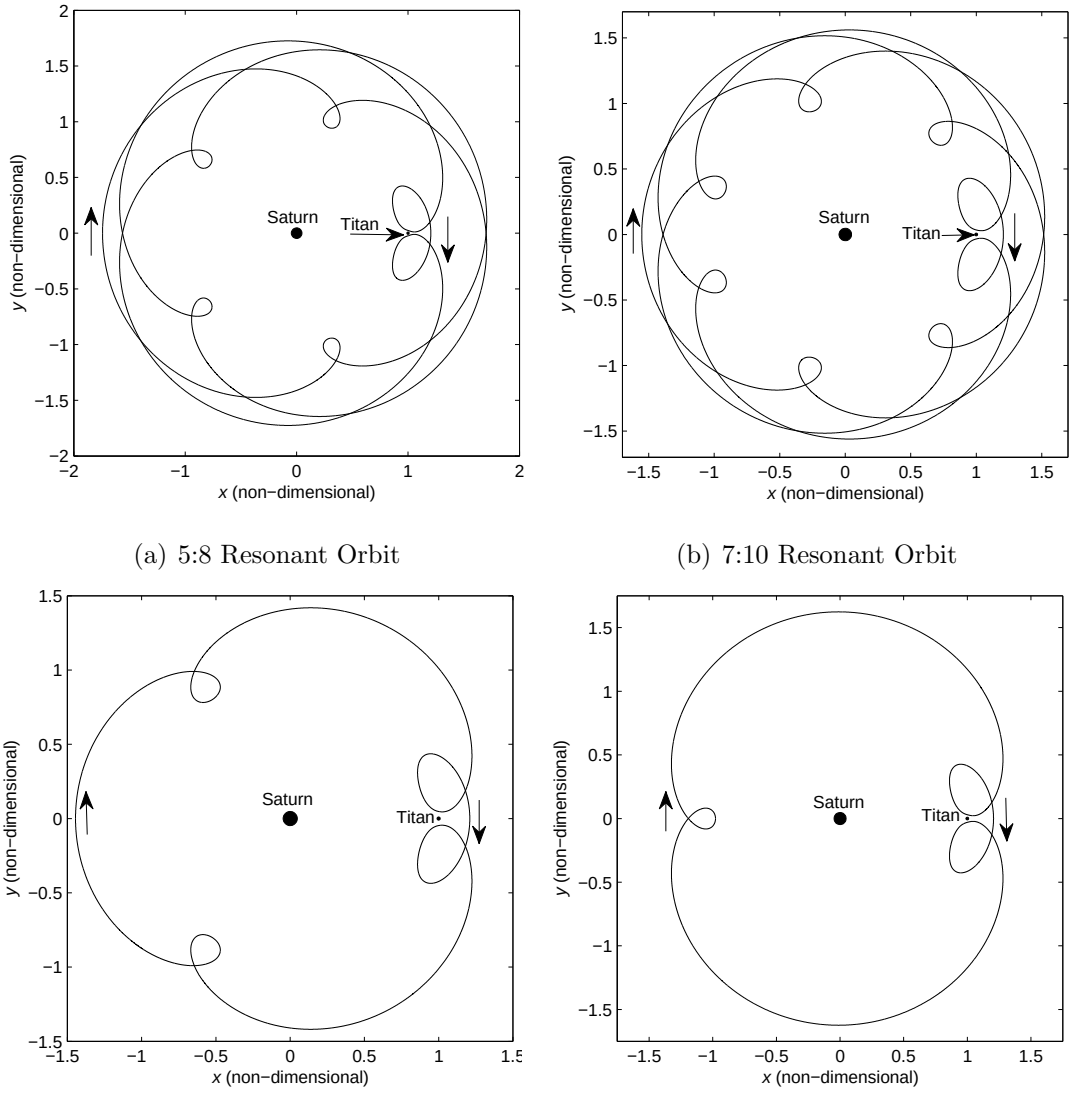

(a) 5:8 Resonant Orbit

(b) 7:10 Resonant Orbit

(c) 3:4 Resonant Orbit

(d) 2:3 Resonant Orbit

Fig. 4.15. Unstable Resonant Orbits in the Saturn-Titan System

each unstable resonant orbit, then a specific relationship is likely. From the manifold structure of the double-loop 2:3 resonant orbit, a resonance transition is possible between the 2:3 resonance and the 7:10, 5:8, and 3:4 resonances. By computing the invariant manifolds that depart and arrive at these orbits using the numerical methods previously described, this relationship is verified by the similarities in the manifold

Table 4.5
Initial Conditions, Unstable Eigenvalue (λ_{uns}), and Orbital Period for the 7:10, 5:8, and 3:4, Unstable Resonant Orbits in the Saturn-Titan System (JC = 2.9787755, $l^* = 1221830.0$ km)

p:q	x (km)	$\dot{y}$ (km/sec)	λ_{uns}	Period (days)
5:8	-2,128,083.3	6.1123408	56,668.767	147.17650
7:10	-1,897,105.5	4.7290504	18,630.954	178.25534
3:4	-1,765,806.0	3.9159718	3,641.3163	81.894437
2:3	-119,5287.8	-0.843470	12,884.441	66.986191

structure. For comparison purposes, the invariant manifolds of the 7:10, 5:8, and 3:4 resonant orbits are displayed in a Poincaré section in Fig. 4.16, Fig. 4.17, and Fig. 4.18, respectively. The similarity in the manifold structure is immediately obvious. The manifolds associated with one orbit closely follow the manifolds corresponding to the other orbits. The stable and unstable manifolds for each resonant orbit intersect at a location on the map corresponding to the fixed point associated with the other resonances, that is, $[x = x_{p:q}, \dot{x} = 0]$. This confirms that resonant transition is also available at this particular energy level through the invariant manifolds associated with the various unstable resonant orbits.

4.4.1 Homoclinic Connections in the Saturn-Titan system

As discovered in the Jupiter-Europa, homoclinic connections also exist in the Saturn-Titan system for a specified energy level. Consider the 5:7 resonant orbit computed in the vicinity an intersection of the invariant manifolds emanating from the double-loop 2:3 unstable resonant orbit illustrated in Fig. 4.20(a). The return on the map corresponding to the fixed point representing the 5:7 resonant orbit is plotted in Fig. 4.19(a) along with the stable and unstable manifolds of the 2:3 resonance. A close-up view of the boxed region is highlighted in Fig. 4.19(b). The state associated

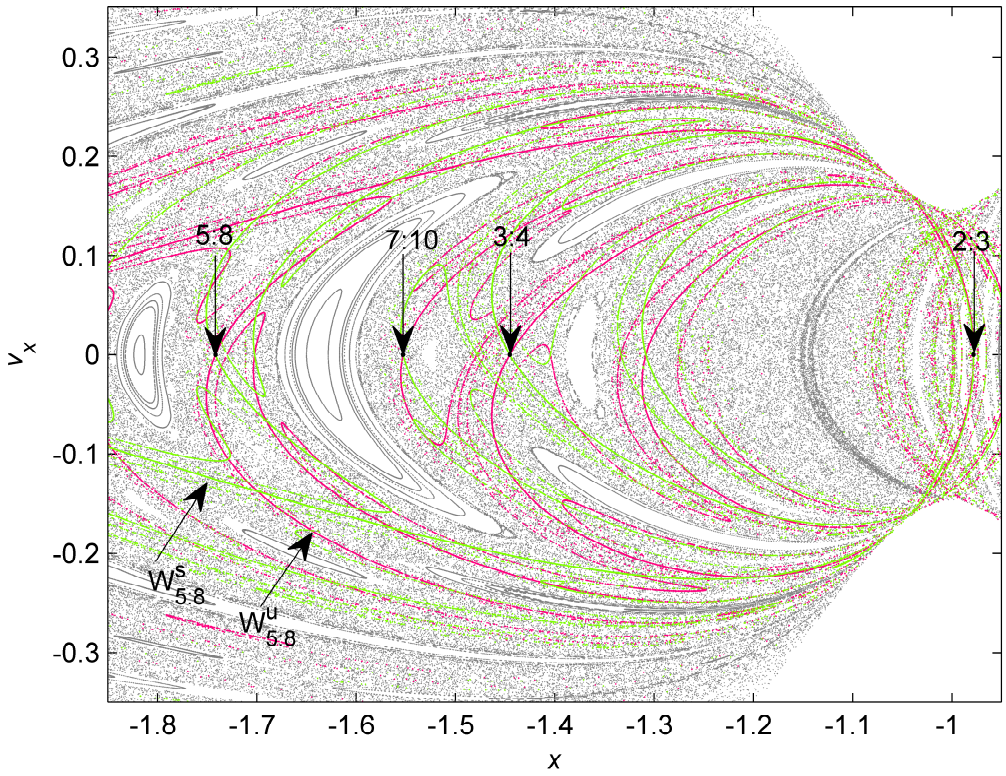

Fig. 4.16. Poincaré Section Illustrating the Relationship between the Invariant Manifolds of the 5:8 Resonant Orbit and Other Resonant Trajectories - Saturn-Titan System

with the intersection of the manifolds near the 5:7 resonance is labeled in Fig. 4.19(b) as 'homoclinic trajectory'. This state corresponds to a homoclinic connection that originates very near the 5:7 resonance, shadows the 5:7 resonant path for the first quarter period, approaches the 2:3 resonance for half a period, and eventually returns to the 5:7 resonant path for the remaining quarter of the period. Hence, its path is closely related to both resonant orbits. To illustrate the resemblance between the homoclinic trajectory and the 5:7 and 2:3 resonances, all three orbits are plotted in Fig. 4.20. The initial state corresponding to this homoclinic connection, computed from the Poincaré map in Fig. 4.19(b), is integrated forward and backward in time for $\tau = \frac{1}{2}P$. The resulting trajectories are displayed in Fig. 4.21 to illustrate how each trajectory follows the unstable and stable manifolds to asymptotically approach

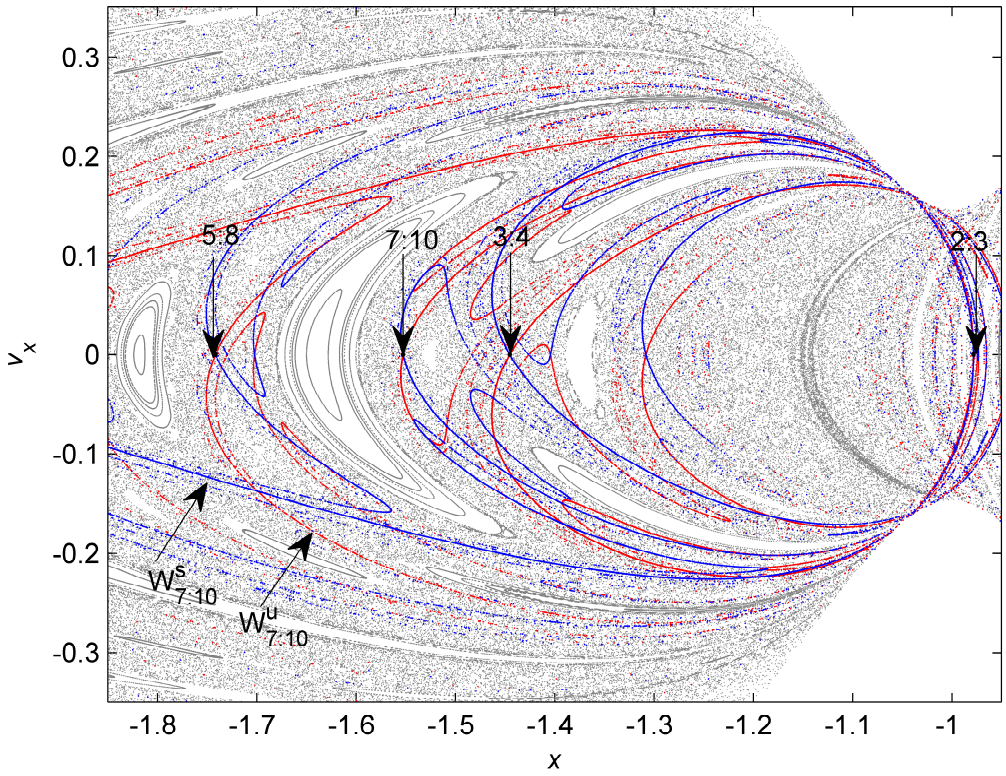

Fig. 4.17. Poincaré Section Illustrating the Relationship between the Invariant Manifolds of the 7:10 Resonant Orbit and Other Resonant Trajectories - Saturn-Titan System

the 2:3 resonance. For completeness, the initial conditions and orbital period for this homoclinic connection are given in Table 4.6.

Table 4.6
Initial Conditions and Orbital Period for the Homoclinic Trajectory - Saturn-Titan System (JC = = 2.9787755, l^* = 1221830.0 km)

x (km)	$\dot{y}$ (km/sec)	Period (days)
-1,812,655.7	4.2084642	178.89424

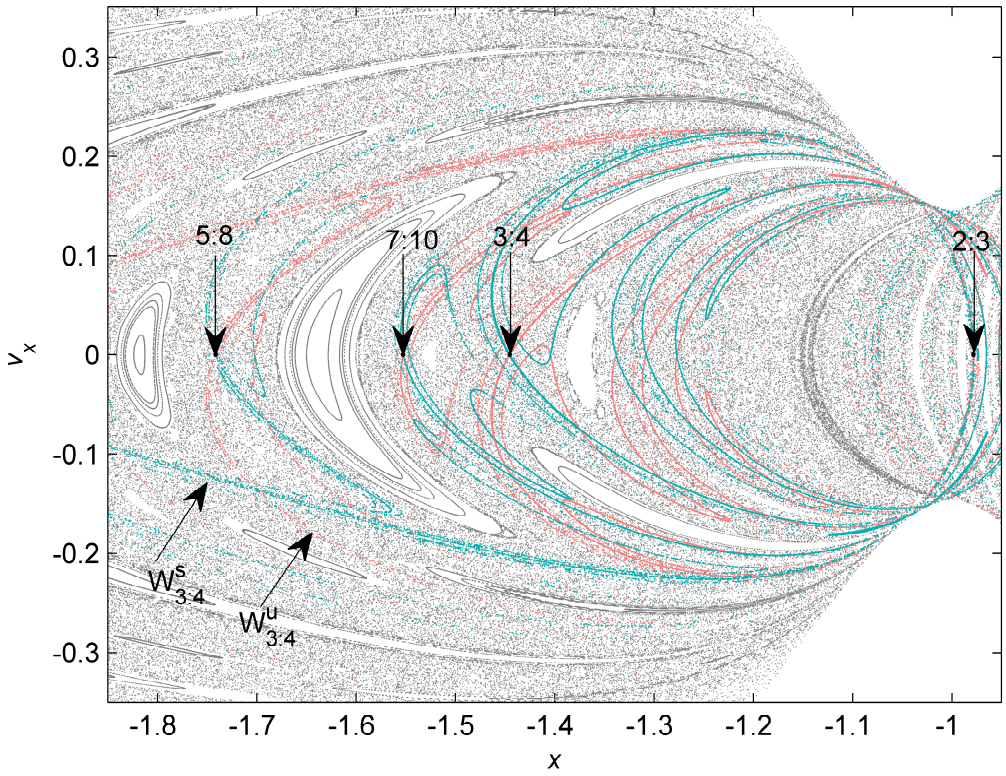

Fig. 4.18. Poincaré Section Illustrating the Relationship between the Invariant Manifolds of the 3:4 Resonant Orbit and Other Resonant Trajectories - Saturn-Titan System

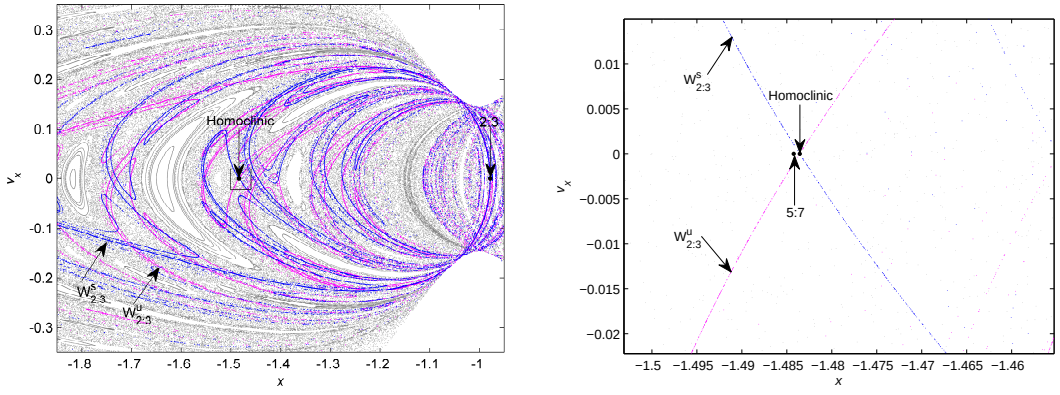

(a) Invariant Manifolds of the 2:3 Resonance

(b) Boxed Region

Fig. 4.19. Poincaré Section Illustrating the Relationship between the Invariant Manifolds of the 2:3 Resonant Orbit, the Homoclinic Connection and the 5:7 Unstable Resonant Orbit - Saturn-Titan System

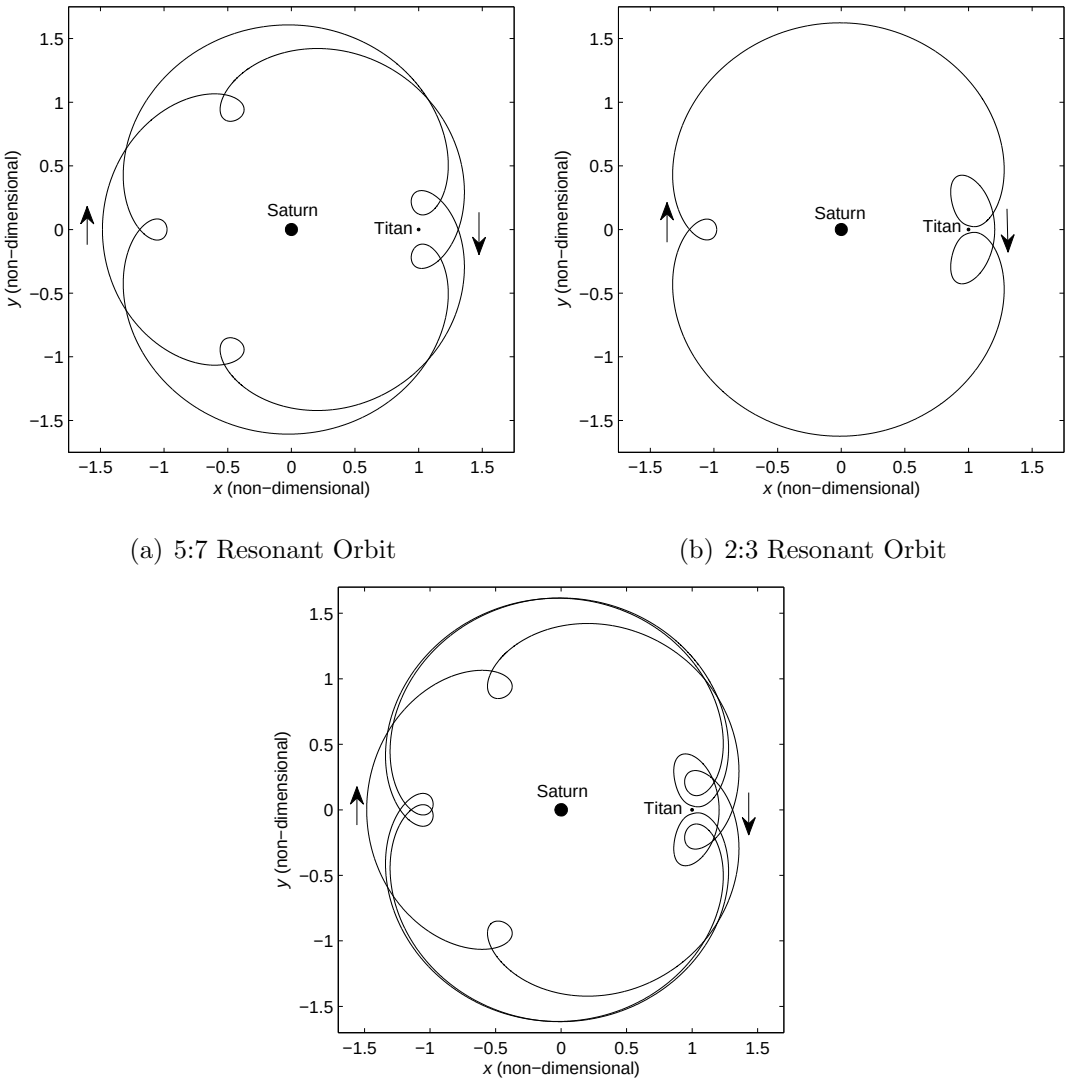

(a) 5:7 Resonant Orbit

(b) 2:3 Resonant Orbit

(c) Homoclinic Trajectory

Fig. 4.20. Unstable Resonant Orbits and Homoclinic Connection in the Saturn-Titan System

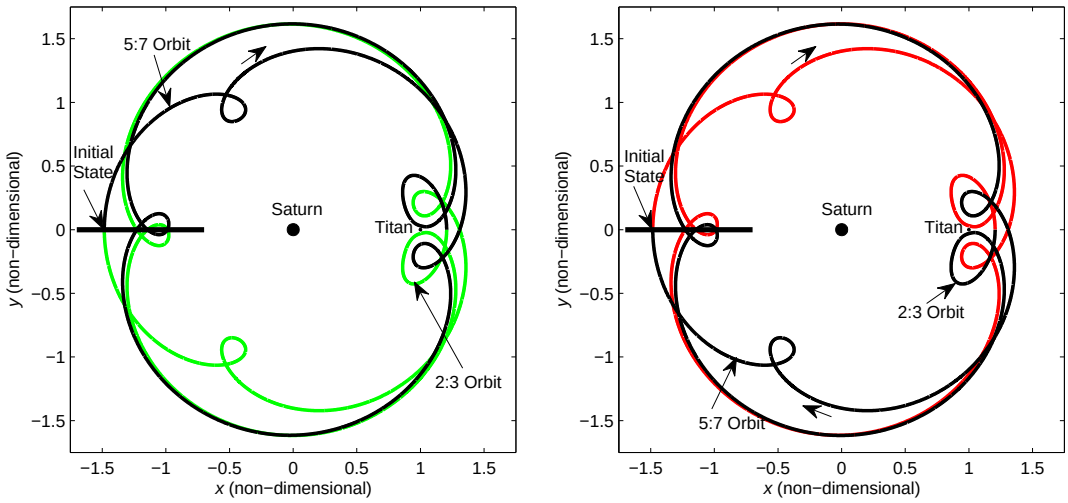

(a) Backward Integration

(b) Forward Integration

Fig. 4.21. Homoclinic Trajectory in the Vicinity of a 5:7 Resonant Orbit - Saturn-Titan System

5. SUMMARY AND RECOMMENDATIONS

5.1 Summary

Poincaré sections are effective in locating and computating unstable resonant orbits and displaying their manifold structures. Results from the analysis for the design of a planar Europa Orbiter flyby trajectory are successfully reproduced in this investigation. The associated surface of section demonstrates that, for the specified energy level, a relationship exists between the invariant manifolds of the two resonant orbits involved in the flyby trajectory. Also notable is the extension of the relationship between these two orbits to three more unstable resonant orbits at the same energy level. In addition, two homoclinic trajectories are computed for the 3:4 and 7:8 resonant orbits. The two homoclinic trajectories intersect at a point that is very near the respective unstable resonant orbits in the Poincaré map. The intersection suggests that a heteroclinic connection may exist between the 3:4 and 5:6 resonances, as well as between the 7:8 and 7:10 resonances for certain energy levels.

The observation that a relationship exists between the manifolds associated with the resonant orbits is explored. The relationship is not an isolated case. Various unstable resonant orbits and their invariant manifolds are computed for a different energy level in the Saturn-Titan system, and, as expected, similar results emerge. At this particular energy level, such a relationship between the invariant manifolds is extended to include four unstable resonant orbits, allowing for potential resonance transfers. This type of relationship may not be unique to a specific system or energy level.

Planar families of unstable resonant orbits in different systems are computed and families of three-dimensional resonant orbits are observed to bifurcate from most of these planar families of resonant orbits. The same type of resonant family is computed

in, at least, two different systems. In fact, a particular family of three-dimensional 2:3 resonant orbits is also located for values of the mass fraction corresponding to the Earth-Moon, Saturn-Enceladus, Saturn-Titan, and Jupiter-Europa systems.

5.2 Conclusions

Two significant observations are notable as a result of this numerical investigation:

(i) Poincaré sections are a powerful tool in the search for unstable resonant orbits at different energy levels and the display of their invariant manifolds. The fact that the invariant manifolds associated with these trajectories are closely related, suggests that these resonances offer good candidates for resonance transition at given energy levels. The Europa Orbiter flyby trajectory supplies evidence for the utility of resonance transitions. The EO trajectory closely follows the invariant manifolds associated with the 3:4 resonant orbit and, then, apparently transitions between the 3:4 and 5:6 resonances [5].

(ii) The existence of multiple families of three-dimensional orbits in various systems suggests that these families may exist for a wider range of mass ratio values, and such families are likely to be related to each other.

5.3 Recommendations for Future Work

Exploration and exploitation of Poincaré sections for application to trajectory design in astrodynamics has emerged only recently, but offers great insight. Further development of the methodology to create a practical design tool can yield many benefits. To reach that goal, some recommendations that build directly from this work include:

(i) Further investigation of the relationship between the invariant manifolds corresponding to unstable resonant orbits for different values of mass ratio and at different energy levels is warranted.

(ii) The three-dimensional resonant families offer significant advantages for design if the families are more completely mapped. The relationship between two-dimensional and three-dimensional families can be clarified. The stability of these families can be assessed and the manifolds explored. New techniques may be required to utilize the manifolds because of their complexity.

(iii) The most significant task is likely to be transfer design tool. Identification of the unstable resonant orbits, recognition of the resonance transitions, computation of suitable trajectory arcs, and blending of the arcs into a variable trajectory that yields a complete design is the goal. Note that the ultimate trajectory design may be natural or include maneuvers.

New strategies and computational tools are ultimately required to accomplish these objectives.

LIST OF REFERENCES

LIST OF REFERENCES

[1] J. R. Johannesen and L. A. D'Amario, "Europa Orbiter Mission Trajectory Design," in *AAS/AIAA Astrodynamics Specialist Conference*, (Girdwood, Alaska), August 16-19 1999. Paper AAS 99-360.

[2] M. W. Lo, R. L. Anderson, G. Whiffen, and L. Romans, "The Role of Invariant Manifolds in Low Thrust Trajectory Design (Part I)," in *AAS/AIAA Spaceflight Dynamics Conference*, (Maui, Hawaii), February 2004. Paper AAS 04-288.

[3] R. L. Anderson and M. W. Lo, "The Role of Invariant Manifolds in Low Thrust Trajectory Design (Part II)," in *AAS/AIAA Spaceflight Dynamics Conference*, (Providence, Rhode Island), August 2004. Paper AAS 06-190.

[4] M. W. Lo, R. L. Anderson, T. Lam, and G. Whiffen, "The Role of Invariant Manifolds in Low Thrust Trajectory Design (Part III)," in *AAS/AIAA Spaceflight Dynamics Conference*, (Tampa, Florida), January 2006. Paper AAS 06-190.

[5] R. L. Anderson, "Low Thrust Trajectory Design for Resonant Flybys and Captures Using Invariant Manifolds." Ph.D. Dissertation, School of Aeronautics and Astronautics, University of Colorado, Boulder, Colorado, 2005.

[6] V. Szebehely and H. Mark, *Adventures in Celestial Mechanics*. New York, New York: John Wiley and Sons, Inc., second ed., 1998.

[7] J. Barrow-Green, *Poincaré and the Three Body Problem*. Volume 11 of History of Mathematics, Providence, Rhode Island: American Mathematical Society, 1997.

[8] V. Szebehely, *Theory of Orbits: The Restricted Problem of Three Bodies*. New York, New York: Academic Press, Inc., 1967.

[9] H. Poincaré, *Les Méthodes Nouvelles de la Mécanique Celeste*, vol. II. Paris: Gauthier-Villars, 1893.

[10] H. Poincaré, *Science and Hypothesis*. London: Walters Scott Publishing, 1905.

[11] I. Peterson, *Newton's Clock: Chaos in the Solar System*. New York: W. H. Freeman and Company, 1993.

[12] G. D. Birkhoff, *Dynamical Systems*, vol. 9 of *American Mathematical Society Colloquium Publications*. Providence, Rhode Island: American Mathematical Society, 1927.

[13] T. S. Brown, "Multi-Body Mission Design in the Saturnian System With Emphasis on Enceladus Accesibilty." M.S. Thesis, School of Aeronautics and Astronautics, Purdue University, West Lafayette, Indiana, 2008.

[14] K. C. Howell, "Families of Orbits in the Vicinity of the Collinear Libration Points," *Journal of the Astronautical Sciences*, vol. 49, pp. 107–125, January-March 2001.

[15] R. W. Farquhar and A. A. Kamel, "Quasi-periodic Orbits About the Translunar Libration Point," *Celestial Mechanics*, vol. 7, pp. 458–473, 1973.

[16] K. C. Howell, "Three-dimensional, Periodic, 'Halo' Orbits," *Celestial Mechanics*, vol. 32, pp. 53–71, January 1984.

[17] R. W. Farquhar, "The Flight of ISEE-3/ICE: Origins, Mission History, and a Legacy," *Journal of the Astronautical Sciences*, vol. 49, pp. 23–73, January-March 2001.

[18] V. Domingo, B. Fleck, and A. I. Poland, "The SOHO Mission: An Overview," *Solar Physics*, vol. 162, pp. 1–37, 1995.

[19] P. Sharer and T. Harrington, "Trajectory Optimization for the ACE Halo Orbit Mission," in *AAS/AIAA Astrodynamics Specialist Conference*, (San Diego, California), 29-31 July 1996. Paper AAS 93-3601.

[20] C. L. Bennett, M. Bay, M. Halpern, G. Hinshaw, C. Jackson, N. Jarosik, A. Kogut, M. Limon, S. S. Meyer, L. Page, D. N. Spergel, G. S. Tucker, D. T. Wilkinson, E. Wollack, and E. L. Wright, "The Microwave Anisotropy Probe Mission," *Astrophysical Journal*, vol. 583, pp. 1–23, January 2003.

[21] C. Conley, "Low Energy Transit Orbits in the Restricted Three-Body Problem," *SIAM Journal of Applied Mathematics*, vol. 16, pp. 732–746, 1968.

[22] G. Gómez, J. Llibre, R. Martínez, and C. Simó, *Dynamics and Misison Design Near Libration Points Vol. I Fundamentals: The Case of Collinear Libration Points, Volume 2 of World Scientific Monograph Series in Mathematics*. New Jersey: World Scientific, 2001.

[23] K. C. Howell, B. T. Barden, and M. W. Lo, "Application of Dynamical Systems Theory to Trajectory Design for a Libration Point Mission," *The Journal of Astronautical Sciences*, vol. 45(2), pp. 161–178, April-June 1997.

[24] K. C. Howell, B. T. Barden, and R. S. Wilson, "Trajectory Design Using a Dynamical Systems Approach with Application to GENESIS," in *AAS/AIAA Astrodynamics Specialist Conference*, August 4-7 1997. Paper AAS 97-709.

[25] M. Lo and S. Ross, "Low Energy Interplanetary Transfers Using Invariant Manifolds of L1, L2, and Halo Orbits," in *AAS/AIAA Space Flight Mechanics Meeting*, (Monterey, California), February 9-11 1998.

[26] M. W. Lo, "The Interplanetary Superhighway and the Origins Program," in *IEEE Space 2002 Conference*, (Big Sky, Montana), March 2002.

[27] M. A. Minovitch, "A Method for Determining Interplanetary Free-Fall Reconnaissance Trajectories." Technical Memorandum 312-130, Jet Propulsion Laboratory, August 1961.

[28] M. A. Minovitch, "The Determination and Characteristics of Ballistic Interplanetary Trajectories under the Influence of Multiple Planetary Attractions." Technical Report 32-464, Jet Propulsion Laboratory, October 1963.

[29] E. Belbruno and B. Marsden, "Resonance Hopping in Comets," *Astronomical Journal*, vol. 113(4), pp. 1433–1444, 1997.

[30] W. S. Koon, M. W. Lo, J. E. Marsden, and S. D. Ross, "Heteroclinic Connections between Periodic Orbits and Resonance Transitions in Celestial Mechanics," *Chaos*, vol. 10(2), pp. 427–469, 2000.

[31] W. S. Koon, M. W. Lo, J. E. Marsden, and S. D. Ross, "Resonance and Capture of Jupiter Comets," *Celestial Mechanics and Dynamical Astronomy*, vol. 81(1-2), pp. 27–38, 2001.

[32] K. C. Howell, B. Marchand, and M. W. Lo, "Temporary Satellite Capture of Short-Period Jupiter Family Comets from the Perspective of Dynamical Systems," *The Journal of the Astronautical Sciences*, vol. 49(4), pp. 539–557, October-December 2001.

[33] L. R. Irrgang, "Investigation of Transfer Trajectories To and From the Equilateral Libration Points L_4 and L_5 in the Earth-Moon System." M.S. Thesis, School of Aeronautics and Astronautics, Purdue University, West Lafayette, Indiana, 2008.

[34] V. A. Yakubovich and V. M. Starzhinskii, *Differential Equations with Periodic Coefficients*. New York: John Wiley and Sons, 1975.

[35] B. T. Barden, "Using Stable Manifolds to Generate Transfers in the Circular Restricted Problem of Three Bodies." M.S. Thesis, School of Aeronautics and Astronautics, Purdue University, West Lafayette, Indiana, 1994.

[36] R. W. Farquhar, "The Control and Use of Libration-Point Satellites." Ph.D. Dissertation, Stanford University, Stanford, California, 1968.

[37] B. Marchand, "Temporary Satellite Capture of Short-Period Jupiter Family Comets from the Perspective of Dynamical Systems." M.S. Thesis, School of Aeronautics and Astronautics, Purdue University, West Lafayette, Indiana, 2000.

[38] C. D. Murray and S. F. Dermott, *Solar System Dynamics*. Cambridge, United Kingdom: Cambridge University Press, Cambridge, 1999.

[39] T. S. Parker and L. O. Chua, *Numerical Algorithms for Chaotic Systems*. New York: Springer-Verlag, 1989.

[40] J. Guckenheimer and P. Holmes, *Nonlinear Oscillations, Dynamical Systems, and Bifurcations of Vector Fields*. New York: Springer-Verlag, 1983.

[41] L. Perko, *Differential Equations and Dynamical Systems*. New York: Springer-Verlag, 1991.

[42] K. C. Howell, M. Beckman, C. Patterson, and D. Folta, "Representation of Invariant Manifolds for Applications in Three-Body Systems," *The Journal of the Astronautical Sciences*, vol. 54(1), January-March 2006.

[43] D. J. Grebow, "Generating Periodic Orbits in the Circular Restricted Three-Body Problem with Applications to Lunar South Pole Coverage." M.S. Thesis, School of Aeronautics and Astronautics, Purdue University, West Lafayette, Indiana, 2006.

[44] M. Hénon, "Numerical Exploration of the Restricted Three-Body Problem," *International Astronomical Union. Simposium no. 25*, p. 157, 1966. Academic Press, London.

[45] V. V. Markellos and A. E. Roy, "Hill Stability of Satellite Orbits," *Celestial Mechanics*, vol. 23, pp. 269–275, March 1981.

[46] A. Van Helden, "Naming the Satellites of Jupiter and Saturn," *The Newsletter of the Historical Astronomy Division of the American Astronomical Society*, August 1994.

[47] Jet Propulsion Laboratory, "Cassini Equinox Mission." http://saturn.jpl.nasa.gov/.

[48] Jet Propulsion Laboratory, "Voyager: The Interstellar Mission." http://voyager.jpl.nasa.gov/.

[49] R. Greenberg, *Europa: The Ocean Moon, Search for an Alien Biosphere*. Springer-Praxis Books in Geophysical Sciences, 2005.

[50] Jet Propulsion Laboratory, "JPL Solar System Dynamics." http://ssd.jpl.nasa.gov/, 1994.

[51] A. F. Heaton, N. J. Strange, J. M. Longuski, and E. P. Bonfiglio, "Automated Design of the Europa Orbiter Tour," *Journal of Spacecraft and Rockets*, vol. 39, no. 1, January-February 2002.